Surface Enhanced Raman Spectroscopy-Based Sensor for Portable, Multiplexed
Detection of Toxic Metals in Urine

By

Andrew Luis Cook, M.A.

Dissertation

Submitted to the Faculty of the

Graduate School of Vanderbilt University

in partial fulfillment of the requirements

for the degree of

DOCTOR OF PHILOSOPHY

in

Biomedical Engineering

September 30th, 2021

Nashville, TN

Approved:

Todd Giorgio, Ph.D., Chair

Richard Mu, Ph.D.

Joshua Caldwell, Ph.D.

Anita Mahadevan-Jansen, Ph.D.

Kerri Cavanaugh, M.D.

To my wife, Kaitlin, without whose support I would never have finished.

TABLE OF CONTENTS

LIST OF TABLES

LIST OF FIGURES

LIST OF ABBREVIATIONS

AB18C6	4'-Aminobenzo-18-Crown 6
3D	Three-Dimensional
Ag	Silver
Ag/ZnO	Silver Nanoparticle-Decorated Zinc Oxide
Au	Gold
B18C6	Benzo-18-Crown-6
CE	Capillary Electrophoresis
CV	Crystal Violet
DI	Deionized
DMSO	Dimethylsulfoxide
DOD	United States Department of Defense
DPSS	Diode-Pumped, Solid State
DU	Depleted Uranium
e-beam	Electron Beam
EF	Enhancement Factor
FWHM	Full Width-Half Maximum
HPLC	High-Performance Liquid Chromatography
ICP-MS	Inductively-Coupled Plasma Mass Spectrometry
IED	Improvised Explosive Device
LSPR	Localized Surface Plasmon Resonance
PDMS	Poly(Dimethysiloxane)
PEO	Poly(Ethylene Oxide)
PL	Photoluminescence
PVA	Polyvinyl Alcohol
RSD	Relative Standard Deviation
SEM	Scanning Electron Microscopy
SERS	Surface-Enhanced Raman Scattering
TEF Registry	Toxic Embedded Fragments Registry
TEFSC	Toxic Embedded Fragments Surveillance Center
UV-vis	Ultraviolet-Visible
UV-vis-NIR	Ultraviolet-Visible-Near Infrared
VA	United States Department of Veterans Affairs
ZnO	Zinc Oxide

CHAPTER I

INTRODUCTION

BACKGROUND AND SIGNIFICANCE

Need for Toxic Metals Biomonitoring

Personnel in modern conflicts, such as those in Iran and Afghanistan, are exposed to toxic metals from sources such as burn pits[1] and injuries resultant from explosive devices.[2] Indeed, most injuries and fatalities that have occurred in United States combat operations since 2001 are the results of explosions from improvised explosive devices (IEDs).[3,4] Not only are wounded military personnel surviving in much greater numbers than ever before (**Figure I.1**[4]), but such exposures can also have significant adverse long-term health effects for those exposed.[5]

It was once thought that metal fragments imbedded in the body were inert.[5] For this reason, accepted practice was to leave embedded fragments undisturbed unless they presented acute health concerns. It was commonly believed that the trauma associated with surgical removal of those fragments outweighed the presumed negligible long-term health effects of leaving those fragments embedded. Very little was done to actually examine the long-term health effects of such metals.[6] The advent of depleted uranium (DU) in munitions[7] during the Gulf War and increasing evidence demonstrating mobilization of embedded fragments have raised concerns about long-term adverse health effects from embedded fragments.[8–10] Health toxicity from embedded fragments, however, is not limited to DU. There is a range of military-relevant metals, particularly soluble metals, that can cause systemic adverse health effects.[11] The health
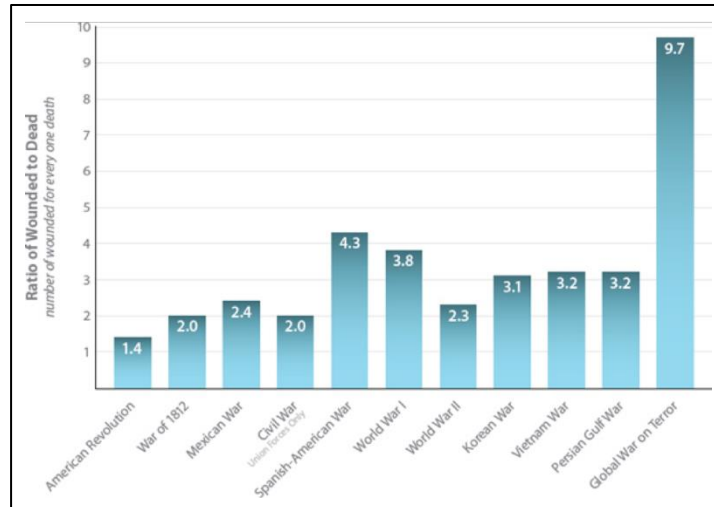
Figure I.1: Ratio of wounded to dead in major U.S. conflicts, illustrating the rising need for toxic metals biomonitoring[4]

concerns associated with embedded toxic metals led the United States Department of Veteran Affairs (VA) to establish the Toxic Embedded Fragments Surveillance Center (TEFSC) at the Baltimore VA Medical Center in 2008 to address the dearth of information regarding fragment composition and adverse health effects.[12] The TEFSC, in turn, established the Toxic Embedded Fragments (TEF) Registry to conduct long-term medical surveillance of affected veterans.[12] TEF biomonitoring is performed via centralized urinalysis at the TEFSC in Baltimore, as many of the metals in question are excreted in urine.[13]

A second significant source for metals toxicity is burn pit exposure. Burn pits are a common method of waste disposal in deployed settings.[14] In such situations, waste includes a wide variety of materials, including flammables, plastics, ammunition, and bulk metals.[15–17] Adverse health effects have been associated with burn pit exposure[18–21] and relevant metals have been found in lung tissue after inhalation.[22] However, other reports conflict with this association,[23–25] and the relationship between burn pit exposure and these health effects is not well understood.[26,27] Indeed, one report explicitly concluded that there is insufficient data to concretely associate adverse health effects with burn pit exposure.[28] This inadequacy is resultant,

2

Table I.1: Metals Included in the TEFSC Biomonitoring Panel[12, 30]

Aluminum (Al)	Copper (Cu)	Nickel (Ni)
Arsenic (As)	Iron (Fe)	Tungsten (W)
Cadmium (Cd)	Lead (Pb)	Uranium (U)
Chromium (Cr)	Manganese (Mn)	Zinc (Zn)
Cobalt (Co)	Molybdenum (Mo)	

in large part, from a lack of post-deployment medical surveillance.[28] Thus, toxic metals biomonitoring for personnel exposed to burn pits can potentially help elucidate the relationship between burn pit exposure, toxic metal inhalation, and associated adverse health outcomes.

Need for Portable Analyte Sensing

Currently, biomonitoring of military members known or suspected of having embedded toxic metal fragments takes the form of urinalysis, with urine samples sent to the Toxic Embedded Fragment Surveillance Center (TEFSC, Baltimore, MD).[12] Analysis is carried out using inductively-coupled plasma mass spectrometry (ICP-MS),[9,29] and the list of metals in the biomonitoring panel includes uranium, cobalt, aluminum, and lead among 14 toxic or potentially toxic metals (**Table I.1**[12,30]). All of these metals have either been found in fragments that have been surgically removed from service members or have well-known toxicological effects.[31] Unfortunately, while an estimated 42,000 veterans possess embedded fragments,[32] only about 19,000 are registered in the TEF registry.[33] This deficit is due in large part because the evaluation process for inclusion into the TEF registry is predicated on the individual's knowledge or suspicion of retained fragments.[30] Thus, biomonitoring of toxic embedded fragments begins long after peak exposure and depends on incomplete knowledge concerning exposure and retention toxic fragments from IEDs, making inclusion into the EFR noncomprehensive. Importantly, this

program does not include veterans who may have retained metals less-readily detected by contemporary imaging evaluation, such as metal particles embedded in the lung after inhalational exposure from burn pits.[12] Beginning biomonitoring long after exposure to IEDs or burn pits also contributes to the lack of concrete correlation between retained toxic metals and adverse health outcomes.[34] For these reasons, portable detection of toxic metals, which can be performed near the time of exposure and can include all exposed rather than a subset, is vital to the development of more comprehensive biomonitoring as well as a better understanding of the adverse health outcomes associated with exposure to toxic metals through IEDs or burn pits.

The TEF registry as it's currently implemented, utilizing centralized ICP-MS urinalysis, is unsuitable for portable toxic metals urinalysis. While ICP-MS is sensitive and precise, it is a large, research-grade instrument that requires significant power and highly trained technicians for operation[35,36] making it unsuitable for use near the locations where military blast injuries occur. For this reason, such monitoring is initiated long after the acute exposure at the time of the blast injury. There is still much uncertainty concerning long-term health effects of embedded metal fragments[6,30,34] and of particulate metal from burn pit exposure,[28,34] yet ICP-MS precludes sample analysis at or near the time of exposure. No commercial instrument combines sensitivity and selectivity for metals associated with military-related exposures with the portable, rugged, self-powered characteristics necessary for use at the site of blast or inhalational injuries. Furthermore, there is a lack of information concerning the scope and extent of both burn pit exposure[17,34,37] and embedded fragments.[4,12] Thus, a device that enables portable toxic metals detection can enable the collection of information concerning composition and acute exposure levels, which may significantly strengthen correlations of health outcomes with toxic metal exposure from embedded fragments or burn pit inhalation.

Toxic Metal Ion Detection Strategies

There are multiple methods available to detect toxic metal ions in an aqueous or organic environment. Some of these are instrumental approaches, such as mass spectrometry, while others are molecular approaches, such as fluorescence and colorimetry, which still require sophisticated dedicated instrumentation. ICP-MS is the method currently used for monitoring embedded fragments in military personnel.[29] ICP-MS is an analysis method that relies on ionizing a sample into an inductively coupled plasma that is characterized by mass spectrometry. The ions are identified based on their mass-to-charge ratios. ICP-MS is very sensitive, being able to detect ng/L concentration,[38] and offers multiplexed detection of toxic metals. However, ICP-MS requires significant sample preparation, often involving dissolution of particulate matter, preconcentration of trace analytes,[39] and sample aerosolization,[40] In addition, highly trained personnel and sophisticated instrumentation is required, making ICP-MS unsuitable for portable toxic metals sensing, as discussed above. Similarly, other instrumental approaches used for metal ion detection, such as inductively coupled plasma optical emission spectrometry (ICP-OES), atomic absorption spectrometry (AAS), and gas chromatography suffer from the same disadvantages.[41] Some studies have combined chromophores with techniques such as high-performance liquid chromatography (HPLC) and capillary electrophoresis (CE) as alternative detection approaches to toxic metals detection. Detection limits in the ng/L range have been achieved with HPLC and μg/L for CE.[41] Both techniques reduce sample preparation difficulty in that they test liquid samples. However, HPLC requires complex instrumentation and CE can require preconcentration steps and suffers from false positives.

Electrochemical techniques are another prevalent class of methodologies for detecting toxic metal ions in urine. The basic setup consists of an electrolytic cell with an ionic conductor and an electronic conductor. In the case of toxic metal ions, an aqueous solution of the toxic

5

metal ions in question acts as the electrolytic cell. Electrochemical ion detection relies on changes induced by the presence of toxic metal ions to electrical parameters such as current, voltage, impedance, and charge. The most sensitive electrochemical techniques have limits of detection on the order of ng/L,[42,43] though detection limits on the order of µg/L are more common.[44–46] Although high sensitivity has been achieved for certain electrochemical techniques, miniaturization remains an issue, making portability problematic. Additionally, most electrochemical techniques suffer from poor reproducibility and stability. These drawbacks coupled with an inability to selectively detect toxic metals in complex samples[47] limit the usefulness of electrochemical techniques for toxic metals detection in the field. There are other optical, electrochemical, or even biological sensing techniques for metal ions, but much work still needs to be done to overcome challenges in sensitivity, selectivity, robustness, field deployability, and cost-effectiveness, among others.[48]

Surface Enhanced Raman Spectroscopy for Trace Analyte Sensing

Raman spectroscopy has attracted much attention in recent years as technique to identify analytes because it is non-destructive to the sample, label-free,[49] and not subject to photobleaching,[50] relying on exciting vibrational modes in molecular bonds. Raman scattering, first discovered in the 1920s,[51] occurs when light illuminates a sample. Most photons are elastically scattered via Rayleigh scattering, but a small portion of incident photons (on the order of one in a million) are inelastically Raman scattered. In Raman scattering, the energy of the photon changes, either losing energy to induce molecular vibrations or (rarely) gaining energy from already vibrating bonds (Stokes and anti-Stokes scattering, respectively; see **Figure**

I.2(a)[52]). The change in photonic energy is dependent on the structure of the molecule in question, and is constant, irrespective of incoming light frequency,[53]

Because Raman scattering is so rare relative to Rayleigh scattering, Raman spectroscopy suffers from low sensitivity, hampering the detection and identification of trace analytes. The effect of Raman's low optical cross-section can be greatly mitigated through surface-enhanced Raman scattering (SERS). First observed in 1974,[54] SERS is the result of two distinct mechanisms. The first is electromagnetic in nature. Light incident on the surface of a conductor causes the excitation of the electron gas within the conductor, called a "plasmon" (**Figure I.2(b)**[55]) When excitation is confined near the surface of the conductor, it is called a "surface plasmon." Importantly, the excitation of surface plasmons requires surface roughness or curvature, as in the case of metal nanoparticles. In the case of nanoparticles, surface plasmons have a "natural frequency," which is dependent on the size and shape of the nanoparticle, the dielectric environment of the nanoparticle, and the metal composition and crystal defect density of the nanoparticle. As the frequency of incident light approaches the plasmon's natural
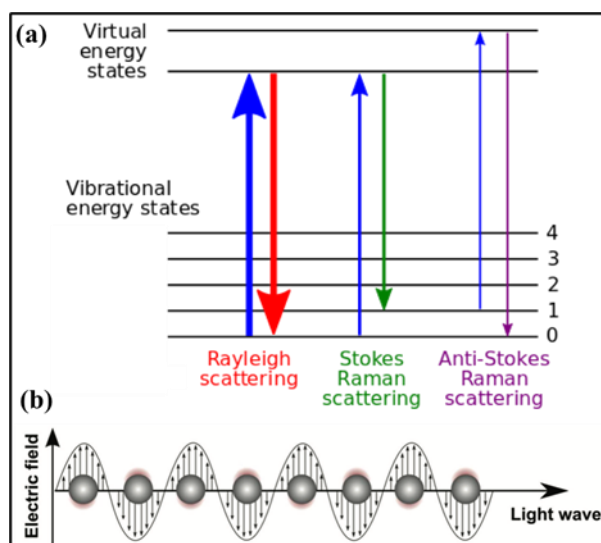
Figure I.2: (a) A Jablonski diagram of Rayleigh, Stokes Raman, and anti-Stokes Raman scattering;[52] (b) An illustration of plasmons caused by incident light.[55]

frequency, a resonance condition occurs, which vastly increases the field local to the nanoparticle. In the case of Raman spectroscopy, this means that not only incident light is enhanced, but also scattered light, causing even greater enhancement to the Raman spectra of analytes local to the nanoparticle.[56] Theoretical estimates show that enhancement factors can be as large as 10^{12}, which can enable single-molecule detection.[57]

While the electromagnetic mechanism is well understood and explains the majority of surface enhancements, the second mechanism is not so clear. There has long been observed, in some cases, an additional one to three orders of magnitude enhancement to the Raman spectra of certain chemisorbed analytes that cannot be explained by the electromagnetic theory.[56–58] This additional enhancement is difficult to isolate from electromagnetic enhancement, but is believed to be chemical in nature, and three different mechanisms have been proposed to contribute to this additional enhancement. The first is chemical interaction between the nanoparticle and the analyte in the ground state. It is suggested that for analytes not covalently bound to the nanoparticle surface, the presence of the metal can induce a slight change in the electronic distribution of the analyte.[55] The second is commonly referred to as the charge-transfer model, in which charge transfer can occur between the molecule and the metal.[55] Charge transfer can occur when the Fermi level of the metal allows charge transfer excitations from the highest occupied molecular orbital to the lowest unoccupied molecular orbital in the analyte.[56–58] The third mechanism is resonance Raman enhancement in chemically bound analytes.[55] While chemical enhancements are not as large as electromagnetic enhancements, they may still be significant.

Surface-Enhanced Raman Sensing of Toxic Metals

SERS-based techniques for sensing toxic metal ions can be divided into three major types based on changes to the SERS reporter signal: SERS signal decrease (or turn-off), SERS signal increase (or turn-on), and SERS signal modification (**Figure I.3**). Common mechanisms for turn-off SERS sensing include reporter detachment[59–62] and nanoparticle de-aggregation (or aggregation prevention)[63,64] in the presence of the metal ion, either from direct interaction between the reporter and the ion or SERS surface, or from ion interaction with a DNAzyme.[61] While these techniques are often very sensitive, they are difficult to multiplex. Furthermore, these techniques have been developed for few metal ions, further complicating the development of a multiplexed toxic metal SERS sensor. Common mechanisms for turn-on SERS sensing of toxic metals include reporter attachment (or juxtaposition),[65,66] and controlled nanoparticle aggregation[67,68] in the presence of the metal ion. By far the most common method of accomplishing both mechanisms is aptamer or DNAzyme functionalization of the SERS substrate. DNAzymes, in particular, have been developed for the selective coordination of a variety of metal ions,[69] and biomolecule-based techniques re often very sensitive. However,
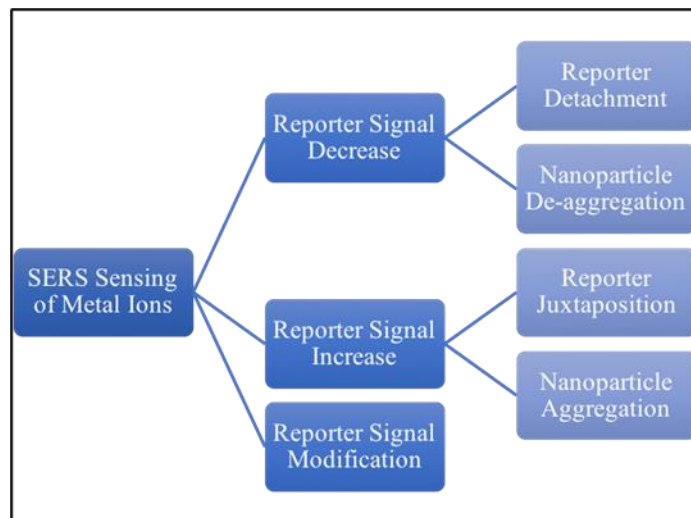
Figure I.3: Breakdown of techniques used for SERS detection of toxic metal ions

9

biomolecules are susceptible to denaturation in suboptimal storage conditions,[70] making them unsuitable for the development of a portable toxic metals sensing platform. Turn-on mechanisms that are not based on aptamers are limited in variety of metal ions able to be sensed, limiting their usefulness for multiplexed toxic metal ion sensing.

Reporter modification techniques for SERS sensing of toxic metal ions rely on changing the SERS signal of the reporter molecule upon coordination with metal ions, rather than change in SERS intensity.[71–74] These techniques do not rely on colloidal SERS substrates, as aggregation and de-aggregation strategies do, nor do they require biomolecules, as aptamer and DNAzyme-based strategies do. Because these techniques rely on signal modification, multiplexation is easier than for turn-on and turn-off strategies. It has been shown that reporter SERS signals will change differently depending on the metal ion being coordinated.[35,71] This reduces the need for highly specific binding, facilitating multiplexed metal ion sensing on the same SERS substrate. These advantages make SERS reporter signal modification the optimal strategy for portable, multiplexed detection of toxic metals.

Zinc Oxide Nanowire-Based Surface Enhanced Raman Spectroscopy

A number of SERS-active substrates have been designed for use with fluid samples, which can be broadly categorized as "in-solution" or "stationary." In-solution SERS nanoprobes have attracted much recent attention for analyte detection, especially for continuous-flow strategies, due to several advantages. These include freedom to manipulate flow, ease of integration with microfluidics, and highly sensitive sensing.[55] However, colloidal nanoprobes suffer from a lack of stability[75] and spectral reproducibility,[76,77] as well as contamination.[78–80] In contrast, stationary SERS-active substrates are much more stable than colloids and result in more

reproducible spectra, due to a lack of uncontrolled dynamic colloid motion.[78] On the other hand, stationary substrates are less sensitive than colloidal nanoprobes since stationary substrates don't mix with sample fluids.[55] Integration of stationary substrates also increases the complexity of microfluidic channel fabrication by requiring extra fabrication steps. For portable SERS sensing applications, the approach must possess sufficient stability and ruggedness to survive in suboptimal conditions, but must also be sensitive enough for trace detection with portable equipment.

A bed of nanowires offers a potential approach for the design of a toxic metal ion sensor in this application for portable SERS. Nanowires possess the stability of stationary substrates, but also an increased surface area, which simultaneously allows for more plasmonic "hotspots" and increased analyte adsorption.[75] Zinc oxide (ZnO) nanowires, in particular, are advantageous for SERS sensing for a number of reasons, the first of which are a large direct bandgap of ~3.3 eV[81] and a high exciton binding energy of 60 meV.[82] This leads to high electronic stability at room temperature and transparency to visible and NIR light,[83] reducing absorption of Raman-scattered photons. ZnO nanowires can also increase surface enhancement through charge transfer, either with analytes directly adsorbed to the nanowire surface or with noble metal nanoparticles decorating the nanowires' surfaces.[81,84] This charge transfer mechanism can synergize with Mie resonances, otherwise known as whispering gallery optical cavity modes. ZnO has a highly faceted Wurtzite crystal structure, and ZnO nanowires can be grown with atomically smooth surfaces.[85] This combined with a refractive index of ~2.0 in the visible region[86] means that Mie resonances can set up for visible light, in which light travels scatters off the nanowire faces inside the nanowire, remaining local to the surface. This Mie scattering

combined with charge transfer and high electron mobility[87] can result in 10^5 enhancement on top of the electromagnetic mechanism discussed above.[88]

The metal chosen for SERS applications plays a large part in the range of wavelengths for which enhancements can occur. While there is a multitude of metals that can be used for SERS, such as gold, platinum, copper, and palladium, silver (Ag) is among the most common metals used for SERS sensing in the visible region.[55] Surface plasmon resonances (SPRs) from Ag nanoparticles generally have wavelengths of 400-500 nm, although nanoparticles with sharp edges or corners can push SPRs towards 800 nm, as shown in **Figure I.4**.[89] Ag nanoparticle strongly enhance Raman spectra by virtue of strong plasmon resonance. By decorating ZnO nanowires with Au or Ag nanoparticles, the advantage of a three-dimensional nanowire structure can be realized.

Chelating Toxic Metals with Crown Ethers

To detect toxic metal ions by SERS reporter signal modification, chelating ligands are required to bind the ions local to the sensing surfaces. These ligands serve the dual purpose of bringing metal ions close to sensing surfaces and reporting the presence of metal ions through changes to the ligands' Raman spectra, since metal ions alone have little to no Raman signal. Specifically, crown ethers are an attractive option for this purpose. Crown ethers are cyclic compounds consisting of a number of ether groups. The most common crown ethers consist of repeating ethyleneoxy units. Variations of these include benzo- or dibenzo-crown ethers which have one or two benzine rings appended to the crown, aza-crown ethers which have nitrogen atoms substituted for oxygen atoms, and thia-crown ethers which have sulfur atoms substituted for oxygen atoms.
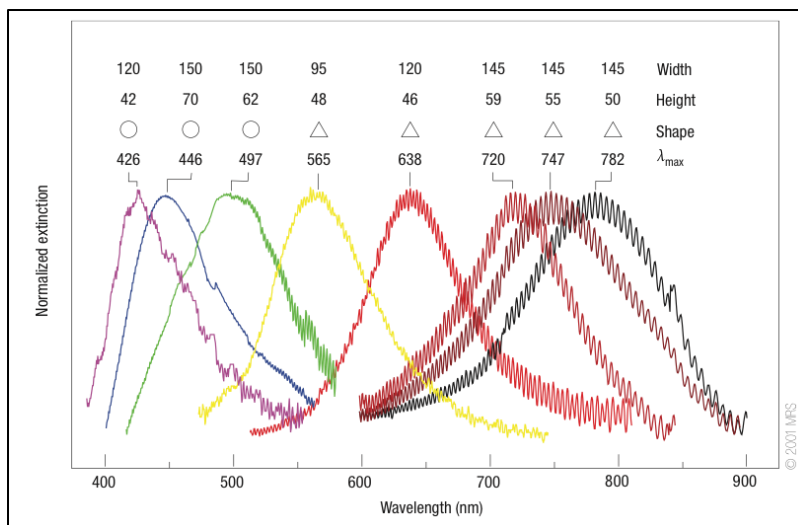
Figure I.4: Effects of size and shape on the wavelength of plasmonic resonance for silver nanoparticles[89]

Crown ethers are best-known for selective coordination of alkali metal cations,[90] but have been studied for coordination with multiple toxic or potentially toxic metals. In particular, 4'-aminobenzo-18-Crown-6 (AB18C6, shown in **Figure I.5**), which has a crown radius of 2.2 – 3.2 Å has been reported to bind Pb^{2+}, which has a radius of 2.4 Å.[91,92] However, crown ethers are known to chelate multiple different cations based on size fit and coordination chemistry.[90] There is evidence that crown ethers with different structures will chelate metal ions differently.[91,93] In addition, solvent affects metal chelation by crown ethers.[94]

Spectral Processing and Analysis

Before Raman spectra can be used in any sort of quantitative analysis, they must be pre-processed, which includes noise removal, background subtraction, and normalization. Noise removal is required to reveal or clarify spectral features due to the small optical cross-section of Raman scattering. Shot noise, which is random in nature and high frequency,[95] can be removed or reduced by a variety of methodologies. Perhaps the simplest is smoothing by a moving
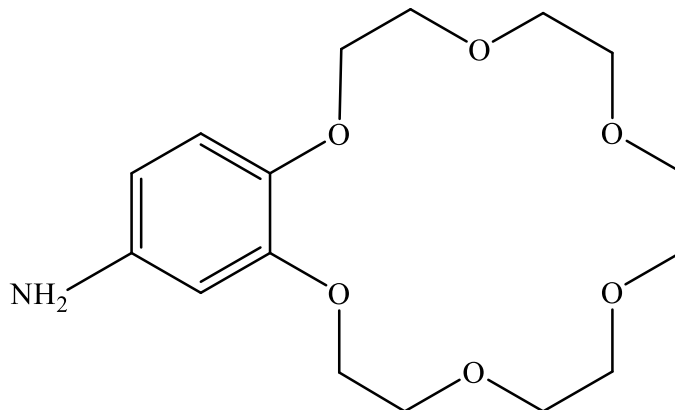
Figure I.5: Chemical structure of 4'-aminobenzo-18-crown-6

average, which relies on the randomness and high frequency of noise. The moving average

technique averages each point on a spectrum with a specified number of adjacent points.[96] With

this technique, spectral points at the ends of the spectrum are lost due to an inability to average

them. Additionally, increasing the number of points to be averaged also increases spectral

distortion in the smoothed spectrum. Smoothing by the Savitzky-Golay polynomial technique[97]

can alleviate spectral distortion, as each point in the spectrum is fit to a polynomial function

derived from adjacent points. The order of the polynomial is dependent on the number of

adjacent points used, with an nth-order polynomial requires $2n+1$ points. Low-order polynomials

significantly reduce noise, with an increased risk of spectral distortion. High-order polynomials

reduce signal distortion at the cost of reduced noise removal. If the signal-to-noise ratio is

extremely small, noise can be removed by discrete frequency analysis accomplished by applying

the fast Fourier transform to the spectrum. By this technique, high-frequency spectral

components can be separated from mid- and low-frequency components. However, difficulty lies

in choosing the frequencies to remove, as Raman bands can have similar frequencies to noise.

Cosmic rays are another common source of noise, causing significant but random spikes during

measurement.[98] These, being random, are extremely unlikely to occur at the same wavenumber

over multiple measurements, can be easily removed by repeat measurements.[99]

A major component of Raman spectra, particularly of organic materials (including crown ethers), is broad background signal due to fluorescence that can alter acquired Raman spectra. Although several methods exist to remove background from spectra, perhaps the most common is polynomial curve fitting.[99] This technique fits the purpose well, as fluorescence background is broadband with few features. Polynomial fitting also lends itself well to Raman analysis because it largely preserves Raman band shape and intensity, if performed correctly. However, a major drawback of this technique has been the need for extensive manual and subjective processing to exclude Raman bands from the curve-fitting process. This drawback has been significantly alleviated by the development of an automated polynomial function developed by Lieber and Mahadevan-Jansen,[100] This function iteratively examines spectral data points, conserving those that are lower in intensity than the corresponding point on the fitted polynomial curve. This process effectively retains Raman bands while eliminating broadband fluorescence, even for spectra with weak Raman bands respective to fluorescence.[101]

SPECIFIC AIMS

As of 2017, improvised explosive devices (IEDs) have accounted for 75% of all traumatic injuries to U.S. soldiers in recent conflicts in Iraq and Afghanistan.[29] As a result, an estimated 42,000 veterans possess embedded fragments.[30,32] In response to this growing need, the United States Department of Veterans Affairs (VA) established the Toxic Embedded Fragment Surveillance Center (TEFSC, Baltimore, MD) in 2008 with the overall mission to 1) identify veterans who may have embedded metal fragments, and 2) conduct long-term medical surveillance of this population.[12] The evaluation process for inclusion into the Embedded Fragments Registry (EFR) is predicated on the individual's knowledge or suspicion of retained

fragments.[31] Thus, biomonitoring of toxic embedded fragments begins long after peak exposure and depends on incomplete knowledge concerning exposure and retention toxic fragments from IEDs, making inclusion into the EFR noncomprehensive. As a result, there are currently only around 19,000 Veterans enrolled in the EFR.[33] The development of a portable toxic metals sensor would allow military personnel to be screened for toxic metal ions associated with embedded fragments near the time of exposure, enabling more comprehensive biomonitoring of veterans exposed to toxic metals, as well as potential early intervention.

The overall goal of this work is to develop an inexpensive, disposable sensor that can reproducibly characterize the presence of analytes such as toxic metals in biological and environmental samples using portable equipment. This work will develop a microfluidic device integrated with an inherently three-dimensional surface-enhanced Raman scattering (SERS) substrate using a novel fabrication procedure. In preparation to functionalize this SERS-active substrate with the chelating ligand 4'-aminobenzo-18-crown-6, this work will identify which toxic metals are selectively chelated by this crown ether in solution (**Figure I.6**).

Specific Aim 1: Optimize silver nanoparticle formation for surface enhanced Raman spectroscopy with 532-nm laser.

To maximize the sensitivity of the sensor, Ag nanoparticles' shape and dimensions must be modified to align their plasmon peak with the fingerprint region of the analyte. To accomplish this, the effects of Ag nanoparticles' deposition and anneal parameters on their plasmon peak will be examined. Ag film thicknesses of ranging from $1 - 9$ nm will be deposited on a ZnO layer via electron beam deposition at rates of 0.1 and 0.3 Å/s. These films will be examined via SEM imaging to examine their shape and distribution. UV-Vis spectrophotometry will be
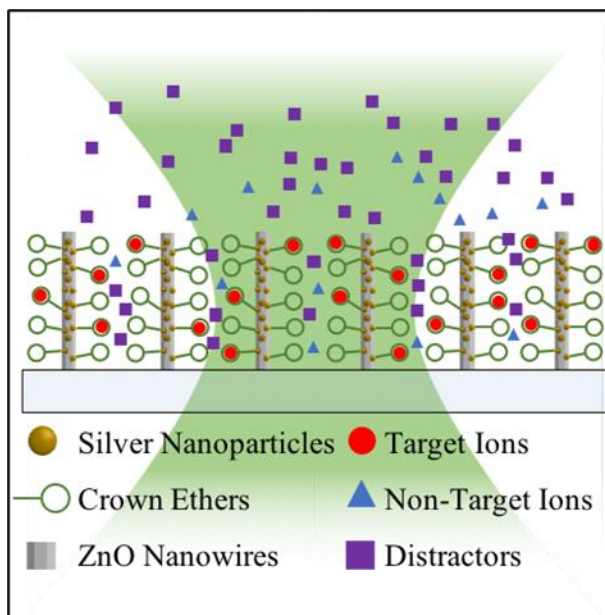
Figure I.6: Illustration of the proposed advanced sensor. ZnO nanowires decorated with silver nanoparticles amplify the changes in Raman spectra resulting from metal binding to crown ethers functionalized to the silver

performed to ascertain their plasmon peak properties and Raman spectra will be acquired using a 532-nm laser from crystal violet (CV) deposited on the substrates to determine which thicknesses afford the most spectral enhancement. These substrates will be annealed at temperatures ranging from $50 - 400$ °C for times ranging from $15 - 150$ min, with UV-Vis being performed as above to discover how their plasmon properties change due to annealing. Likewise, Raman spectroscopy will be performed on annealed substrates to determine how annealing changes affects the nanoparticles' surface enhancement at each thickness. An optimal nanoparticle fabrication and anneal parameters will be determined from these results, maximizing device sensitivity.

Specific Aim 2: Design and Fabricate Microfluidic Channel with Integrated Silver-Decorated Zinc Oxide Nanowires for Surface Enhanced Raman Spectroscopy.

Surface-enhanced Raman scattering (SERS) detection of selected analytes will be characterized within a microfluidic channel. The SERS-active substrate will consist of high quality, single-crystal zinc oxide (ZnO) nanowires and silver (Ag) nanoparticles decorating the nanowire sides. A microfluidic channel master will be fabricated and will be used to embed the channel in poly(dimethylsiloxane) (PDMS). A ZnO seed layer will be patterned inside the microfluidic channel and ZnO nanowires will be grown from this seed layer. ZnO nanowires will be characterized for crystallinity, defects, and dimensionality. Ag nanoparticles will be deposited on the nanowires and characterized for plasmonic resonance. Subsequently, the PDMS will be irreversibly bonded to glass and a solutions of crystal violet and melamine, a Raman-reporter and contaminant of dairy products respectively, will be injected into the channel. Label-free SERS sensing of crystal violet at various concentrations will demonstrate efficacy of the SERS-active substrate within a microfluidic channel.

Specific Aim 3: Explore Chelation of Toxic Metals by 4'-Aminobenzo-18-Crown-6

Once device utility for SERS sensing has been demonstrated, the chelation of toxic metals will be explored in multiple solutions. The metal ions which crown ether 4'-aminobenzo-18-crown-6 (AB18C6) binds in both 1:1 dimethylsulfoxide (DMSO):DI water and 1:3 DMSO:DI water will be determined using UV-Vis spectrophotometry. Metals will be selected for further study based on how well they are chelated by AB18C6. Fluorescence spectroscopy will be performed on AB18C6 chelating selected metals, and concentration-dependent studies will be performed with both UV-Vis spectrophotometry to explore the possibility of using fluorescence

and UV-Vis to inform SERS quantification of toxic metals, or as possible dual sensing strategies in conjunction with SERS.

CHAPTER II

OPTIMIZATION OF SILVER NANOPARTICLE FORMATION FOR SURFACE-
ENHANCED RAMAN SPECTROSCOPY WITH A 532-NM LASER

Reprinted with permission from:

ABSTRACT

Surface enhanced Raman spectroscopy enables robust, rapid analysis on highly dilute

samples. To be useful, the technique needs sensing substrates that will enhance intrinsically

weak Raman signals of trace analytes. In particular, three-dimensional substrates such as zinc

oxide nanowires decorated with electron-beam deposited silver nanoparticles are easily

fabricated and serve the dual need of structural stability and detection sensitivity. However, little

has been done to optimize e-beam deposited silver nanoparticles for maximal surface

enhancement in the unique dielectric environment of the zinc oxide substrate. Herein, fabrication

and anneal parameters of electron beam-deposited silver nanoparticles were examined for the

purpose of maximizing surface enhancement. Specifically, this work explored the effect of

changing film thickness, deposition rate, anneal temperature, and anneal time on the surface

plasmon resonance of Ag nanoparticles. In this study, multiple sets of fabrication and annealing

parameters were discovered that optimized surface plasmon resonance for maximal enhancement

to Raman signals acquired with a 532-nm laser. This work represents the first characterization of

the fabrication and annealing parameters for electron beam-deposited silver nanoparticles on zinc

oxide.

INTRODUCTION

There is an unmet multidisciplinary need for bioanalytical techniques that can perform analyses on small volumes of highly diluted specimens with minimum sample preparation. Applications such as the detection of toxic metals,[93,103–105] other pollutants or contaminants,[106–109] circulating tumor cells,[110] bacteria,[111] or viruses[112] benefit from fast and reliable molecular sensing. State-of-the-art tools used for these purposes such as high-performance liquid chromatography, mass spectrometry, and enzyme-linked immunosorbent assays commonly involve expensive reagents, large sample volumes, skilled technicians and frequently have low throughput rates. In addition, such tools are often plagued by limited differentiation among chemically or biologically similar analytes.[113–115] Raman spectroscopy is an attractive technique that addresses some of the limitations of other approaches because it provides a unique spectroscopic "fingerprint" of the biomolecular and biochemical composition of specimens, potentially offering effective detection of analytes in minutes or seconds.[116–118] Raman also exhibits portability and facile function, as demonstrated by its use in forensic fields such as explosives identification.[119] However, Raman scattering has a small optical cross-section, with only one in $10^6 – 10^8$ photons being Raman scattered, limiting its usefulness for trace analyte sensing. Surface-enhanced Raman spectroscopy (SERS), however, can significantly enhance intrinsically weak Raman signals, enabling reliable, efficient, and non-destructive detection of highly dilute analytes.

It is well-known that there are two mechanisms principally responsible for the enhancement effects in SERS: an electromagnetic mechanism resulting from localized surface plasmon resonance (LSPR) and a chemical mechanism resulting from charge transfer between analyte and metallic nanostructure.[56,120,121] To take full advantage of the dominant electromagnetic mechanism of surface enhancement, it is necessary that the nanoparticles be

21

spatially dense, to make use of "hotspots" in the gaps between nanoparticles.[57,122] For these

reasons, much attention has been devoted to the use of metallic nanoparticles for incorporating

SERS into various sensing system solutions. However, the expansive parameter space

controlling SERS performance requires further investigation to effectively design sensors that

provide optimal surface enhancement of intrinsically weak Raman signals.

Silver (Ag) is among the most commonly used metals for SERS-based sensing, due to

strong Ag plasmon resonance in the visible region[123,124] and facile synthesis.[125] Many Ag

nanostructures have been explored for SERS-based sensing, which fall into two basic categories:

(1) colloidal nanostructures and (2) nanostructures on solid surfaces.[126] Colloidal nanostructures

offer high sensitivity due to the ability to easily generate a large sensing surface area. However,

due to random suspension of particles in free solution, colloidal nanostructures lack stability, and

thus can affect measurement reproducibity. Conversely, nanostructures fabricated onto solid

surfaces can possess great structural stability, resulting in greater measurement reliability.

However, this stability comes at the cost of reduced sensitivity compared to colloidal paradigms

due to lower surface area. This cost can be mitigated by fabricating inherently three-dimensional

(3D) sensing substrates, as described in our previous work.[127] There are several methods of

fabricating metallic nanoparticles onto a solid substrate that generally fall into two categories:

chemical fabrication and physical deposition. Physical deposition techniques such as electron

beam (e-beam) deposition facilitate formation of densely arranged Ag nanoparticles, enabling

use of "hot-spots" between nanoparticles.[128] However, these techniques do not easily lend

themselves to control of nanoparticle properties that affect LSPR. In the case of chemical

fabrication, techniques such as hydrothermal growth are used to fabricate nanoparticles directly

on the sensing surface.[129] While these techniques are more easily implemented and easier to

control than physical deposition, they usually result in lower surface coverage by nanoparticles, reducing the impact of inter-particle hotspots. Therefore, by exploring the fabrication parameters that affect nanoparticle formation in physical deposition paradigms, greater control over nanoparticle formation can be implemented.

Recent research has illuminated multiple strategies for realizing 3D templates for SERS-active substrates, including anodized aluminum oxide,[130] porous silicon,[131] electrospun polymers,[132] silicon nanowires,[133] and zinc oxide (ZnO) nanowires,[129] among others. ZnO, in particular, is an attractive material for fabricating 3D SERS substrates. ZnO is a biocompatible[134] wide direct-bandgap semiconductor with a band-edge emission of 3.3 eV and a high exciton binding energy of 60 meV, making it electronically stable at room temperature.[135,136] The semiconducting nature of ZnO also enables charge transfer between the ZnO and Ag,[137] increasing surface enhancement over strategies that rely solely on the electromagnetic mechanism. Crystalline ZnO is also transparent to visible light,[83] which reduces absorptive loss of light when acquiring spectra through the substrate as we did in our previous work.[127] Additionally, ZnO possesses a large refractive index of approximately 2.0 in the visible region, which aids in the confinement of light.[86,138] Combining these characteristics with the atomically smooth and highly faceted hexagonal single-crystal structure of the nanowires allows for wave-guiding of light, which can reduce signal loss due to light scattered away from the detector.[85]

Previously, we prepared ZnO nanowires decorated with Ag nanoparticles for sensing soluble analytes. This sensing paradigm yielded an estimated six orders of magnitude surface enhancement of the Raman signal for crystal violet (CV, CCDC # 137090), melamine, and adenine.[127] Performance of this sensor was likely reduced because the Ag nanoparticles, with a plasmon peak at ~460 nm, were not optimal for SERS with the 532-nm laser used. We also did

not explore the sensor performance as a function of Ag deposition parameters that are likely to influence SERS amplification mechanisms. Through this study, Ag-decorated ZnO nanowires demonstrated potential for effective sensing of trace analytes, which can be realized by examining the effect of fabrication and anneal parameters on surface plasmon resonance.

Parameters that can be manipulated during e-beam deposition of Ag and significantly impact the Raman enhancement include film thickness and deposition rate. Film thickness, in general, changes the shape and surface coverage of metallic nanostructures which changes LSPR characteristics of the film. By consequence, these changes modulate the magnitude of surface enhancement. Other research groups have explored how Ag nanoparticle plasmon resonance changes with film thickness in e-beam deposited[139] and sputtered[140] systems, but in neither of these works were nanoparticles deposited on a ZnO layer, which can significantly impact plasmon resonance as part of the dielectric environment of the nanoparticles. Also, while the effects of Ag film thickness on LSPR has been explored in some way, little attention has been devoted to the effects of Ag film deposition rate on plasmon resonance, even though deposition rate has a known effect on the structural properties of metallic films.[141] Furthermore, thermal annealing following deposition changes the nanoparticle size and shape through Ostwald ripening.[142] Since nanoparticle geometry and dimension are important drivers of plasmon resonance, thermal annealing offers an additional strategy for optimization of SERS sensing. Thermal annealing occurs as a result of two independent parameters: anneal temperature and anneal time.

In this work, four independently selectable parameters that influence Ag nanoparticle formation and presentation on ZnO were quantitatively controlled. These parameters, namely film thickness, deposition rate, anneal temperature, and anneal time were examined to assess

24

their impact in modulating surface plasmon resonance. The functional consequences of these fabrication parameters were comparatively assessed using surface-enhanced Raman spectra that were acquired from crystal violet deposited onto each substrate. We aim to discover fundamental fabrication principles and sensor characteristics that will advance the design of maximally sensitive SERS devices based upon e-beam deposited Ag nanoparticles on a ZnO substrate.

EXPERIMENTAL

Substrate Preparation

Glass slides (Fisherbrand® Plain Microscope Slides) were cut into 80 1-cm^2 substrates with a diamond saw and cleaned by sonication sequentially for 10 minutes each in 1% aqueous Alconox® solution, deionized (DI) water, acetone, methanol, and again in DI water. Onto these substrates, a 100 nm ZnO layer was deposited via e-beam deposition at a rate of approximately 0.1 Å/s to ensure even deposition of Zn and O. As demonstrated by **Figure A.1**. Masks were cut from aluminum foil large enough to completely cover the substrates, with a square cutout ~0.2 cm to a side, allowing an Ag film to be deposited on only a small portion of each substrate. After each film was deposited, the masks were shifted so that the cutouts exposed a new portion of each substrate, and a new film was deposited. This process was repeated nine times, for nine different Ag film thicknesses fit on each substrate, as illustrated by **Figure A.1**. Ag thin films were deposited over a range of 1 nm to 9 nm film thicknesses, in 1 nm increments, hereafter referred to as T1 – T9. The 80 substrates were divided into two groups of 40 substrates, as shown in **Figure II.1**. These two groups, hereafter referred to as Group A and Group B, were deposited with Ag thin films at rates of 0.1 and 0.3 Å/s, respectively. All Ag films in Group A were
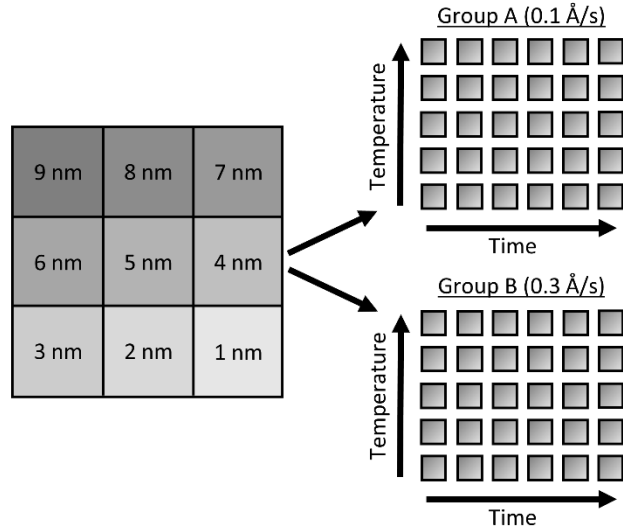
Figure II.1: Schematic of substrates used for parameter exploration. Substrates deposited with 9 different Ag film thicknesses and separated into two rate groups (A and B). In each group, substrates are annealed over a range of times (15 – 150 min) and temperatures (50 – 400 °C)

deposited at rates of 0.1 ± 0.002 Å/s and all Ag films in Group B were deposited at rates of 0.3 ± 0.018 Å/s. It is well known that when material from a point source is deposited onto substrates affixed to a flat plate, deposition rates fall off with axial distance from the source. This results in varying film thickness as a function of axial distance, defined by **Equation (II.1)**:

$$t_d = \left[1 + \left(\frac{d}{R_0}\right)^2\right]^{-3/2} \tag{II.1}$$

In this equation, t_d represents the film thickness at distance d from the axis defined by the point source and R_0 represents the distance from the source to the plane of deposition. R_0 was measured to be 27 cm and the axial distance d of substrates farthest from the source was measured to be ~4.5 cm. Thus, the largest variation in film thickness was ~4% of the target thickness. All e-beam depositions were performed at pressures below 6.7 mPa.

Following the deposition of silver, the substrates were annealed at various temperatures: 50, 100, 200, 300 and 400 °C. At each temperature, different substrates were annealed at times: 15, 30, 60, 90, 120, and 150 minutes, providing a substrate from each deposition rate group (2

26

groups) with every anneal temperature (5) and time (6), producing 2 x 5 x 6 = 60 uniquely fabricated and annealed substrates and 1 unannealed control, each presenting T1 through T9 film thicknesses for a total of 549 different substrates.

Optical Characterization Techniques

Scanning electron microscopy (SEM) images, before annealing, were acquired of each Ag film thickness from a random substrate to get a visual perspective on the changing Ag nanostructure morphology as a result of changing film thickness. These images were acquired using a Zeiss Merlin scanning electron microscope (Jena, Germany) in a plan configuration with a 10 kV electron beam at a magnification of 400,000× and a working distance of 2.8 mm. The average size of nanostructures was determined using Fiji image analysis of acquired SEM images.[143,144] The images were first converted to black-and-white via the Make Binary function and noise was removed via the Despeckle function, in which each pixel is given the median value of its 3×3 neighborhood. The area of the nanostructures was acquired via the Analyze Particles function and area values that didn't correspond to single nanostructures were removed.

Extinction spectra were acquired of each film thickness, on each substrate before and after annealing, using a Hitachi U-4100 spectrophotometer integrating sphere to determine peak surface plasmon resonance wavelength. Extinction spectra were obtained at a rate of 3 nm/s over a range of 350 – 850 nm, with each substrate oriented facing away from oncoming light.

Raman spectra were acquired using a Thermo Scientific DXR Raman microscope (Waltham, MA, USA). A 532 nm diode-pumped, solid state (DPSS) laser was used with a 10x objective (Olympus, MPlan N Achromat, 0.25 NA) at a power of 10 mW as measured at the objective turret. Focal plane was adjusted before each acquisition to maximize spectral intensity.

All substrates were placed in contact with a 25 μM aqueous solution of crystal violet (CV) overnight. The substrates were then removed from the CV solution and air-dried. Five Raman spectra were acquired from each substrate (T1-T9), along with five spectra of a portion on each substrate without Ag, hereafter referred to as T0. Each Raman spectrum was the accumulation of four background-subtracted spectra acquired over a range of 200-1800 cm-1, each taken with a 5 s exposure time. All Raman spectra were acquired with a 50 μm pinhole aperture and a 900 grooves/mm grating.

Spectral Processing

UV-Vis spectra of the Ag films deposited on ZnO layers exhibit extinction from both Ag and ZnO. While ZnO is largely transparent in the visible region, light extinction due to the ZnO band edge occurs below approximately 380 nm. In order to accurately obtain Ag plasmon peak information, absorptive contributions from ZnO were approximated and subtracted as illustrated in **Figure A.2**. This method was chosen to minimize variation in ZnO signal induced by the fabrication and anneal process, as illustrated by **Figure A.3**. To approximate ZnO absorptive contributions, UV-Vis spectra from the T1 portions of each substrate were fitted to a tri-gaussian equation, shown in **Equation (II.2)**. In this fit, the first gaussian approximated the ZnO band-edge contribution, the second approximated the ZnO visible contribution, and the third approximated the Ag plasmon peak. T1 spectra were chosen for this task because of minimal overlap between the Ag plasmon peak and the ZnO band-edge and because the plasmon peak could be accurately approximated by a gaussian curve. Once fits to these spectra were successfully obtained, the third gaussian was subtracted from the fit to arrive at an approximation of the ZnO contribution to the spectra. This ZnO contribution for each substrate was then

subtracted from the UV-Vis spectra for T1-T9 for each substrate. Finally, a cubic smoothing

spline, where **Equation (II.3)**. is minimized, was fit to the resultant plasmon peaks to remove

noise, enabling accurate extraction of plasmon peak extinction, wavelength, and spread.

$$F_g(x) = a_b e^{-\frac{(x-\mu_b)^2}{2\sigma_b^2}} + a_v e^{-\frac{(x-\mu_v)^2}{2\sigma_v^2}} + a_p e^{-\frac{(x-\mu_p)^2}{2\sigma_p^2}} \tag{II.2}$$

$$\lambda \sum_i [y_i - s(x_i)]^2 + (1-\lambda) \int_{x_{min}}^{x_{max}} \left(\frac{d^2 s(x)}{dx^2} \right)^2 dx \tag{II.3}$$

In **Equation (II.2)**, F_g is the gaussian fit, a is an arbitrary fit parameter, and μ & σ

represent the peak and root-mean-square width of the gaussian, respectively. Subscripts b, v, and

p denote the gaussian fitting of the ZnO band-edge, ZnO visible, and Ag plasmon contributions

to the spectrum, respectively. In **Equation (II.3)** λ represents the smoothing parameter, y is the

set of observed extinctions at each wavelength, x is the set of wavelengths at which extinction is

measured, s is the smoothed function output of the equation, and x_{min} & x_{max} are the minimum

and maximum wavelengths of the spectrum, respectively. For this work, a smoothing parameter

$\lambda = 0.003$ was used. A smoothing spline was used to approximate the plasmon rather than a

gaussian because, while the plasmon peaks of thinner films could be accurately approximated by

a gaussian fit, the plasmon peaks of thicker films could not due to increasing asymmetry in the

peak. Spread was measured at the full width-half maximum (FWHM) of each plasmon peak

where possible. For several spectra, particularly of thicker Ag, the FWHM was sufficiently broad

to extend beyond the measured wavelength range and could not be determined. All processing of

UV-Vis spectra was performed in MATLAB.[145] Energy dispersive x-ray spectroscopy had been

previously performed on similarly prepared SERS-active substrates, confirming the presence of

ZnO and Ag.[127]

Table II.1: The benzene and non-benzene vibrational modes of the CV peaks selected for analysis, with the CV molecular structure for reference

Raman Band (cm^{-1})	Non-Benzene Vibrational Modes	Benzene Modes	
420	δ(C-C$_{center}$-C)/δ(C-N-C)$_l$	16a	
915	δ(C-C$_{center}$-C)	12,17a	
1592		8a	
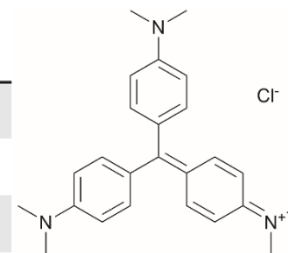
Raman spectra were subtracted of their fluorescent background, estimated using 5th-degree polynomial fit. These spectra were then smoothed using a Savitzky-Golay filter. Each of the five spectra acquired from each film thickness (T0-T9) on each substrate were averaged to find a representative spectrum. Three CV Raman peaks at 420, 915, and 1592 cm^{-1}, tabulated in **Table II.1** with their associated vibrational modes and the CV molecular structure, were selected to provide specific, characteristic features for the estimation of enhancement factors (EFs). These peaks were selected to interrogate EFs from each end of the measured spectra and one feature near the middle of the spectra. The intensities of these peaks in the spectra for T1-T9 on each substrate were divided by the intensities of the same peaks in the spectrum of T0 on the same substrate to arrive at EFs for each peak.

Statistical Analysis

All error bars represent standard deviation unless otherwise stated. Two-way analysis of variance followed by Tukey's and Sidak's multiple comparison tests was performed for data presented here as indicated, and statistical significance was defined as $p < 0.05$. Statistical analyses were performed using Prism 7.04 (GraphPad Software).

RESULTS & DISCUSSION

The surface plasmon peak of a distribution of Ag nanoparticles possesses three characteristics that affect the level of enhancement: peak intensity, peak wavelength, and peak breadth. Because surface plasmons enhance both incident light from the laser and Raman-scattered light, surface enhancement is most effective when high plasmon extinction occurs at both the laser line and across the range of wavelengths at which light is scattered. Thus, the surface plasmon peak should be located near the laser line to maximize enhancement to incident light, and the peak should be sufficiently broad to provide significant enhancement to Raman-scattered light across the wavelength range of interest. In addition, plasmon intensity correlates with enhancement factor, with higher plasmon intensities generally producing greater enhancement for non-colloidal sensing substrates.[146] Surface plasmon peak intensity, wavelength, and breadth are all influenced by nanoparticle size, size distribution, crystal composition, proximity, and shape. These nanoparticle properties are modulated by deposition thickness and deposition rate, and by anneal temperature and time, post-deposition. In this study, we explore the combinatorial effect of these fabrication parameters on the surface plasmon peak characteristics of Ag nanoparticle arrays and correlate these effects to changes in enhancement of intrinsic Raman spectral intensity of CV. By doing so, we aim to facilitate the development of optimized sensing substrates for maximally surface-enhanced Raman spectroscopy.

Effect of Film Thickness on Surface Enhanced Raman Spectroscopy

Increasing Ag film thickness was anticipated to intensify, broaden, and red-shift the plasmon extinction peak due to increasing Ag surface coverage, increasing particle diameter, and decreasing interparticle distance. However, the quantitative relationships that describe these

31
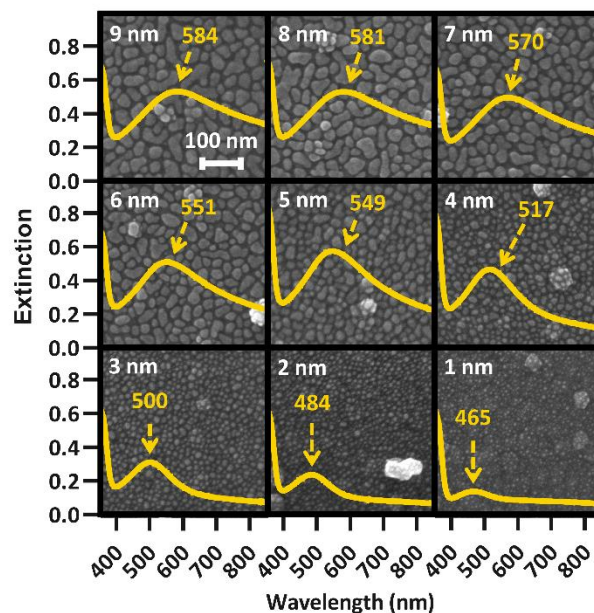
Figure II.2: SEM images of all film thicknesses (identified in white) for a random substrate, with associated extinction spectra displaying peak plasmon wavelength overlaid. The plasmon peak wavelength is identified in yellow for each extinction spectrum.

effects as a function of film thickness have not been previously described. Furthermore, while increasing intensity is correlated with increasing surface enhancement, for solid substrates, maximizing enhancement requires proximity of the peak wavelength with the incident laser. In addition, broadening the plasmon peak is only effective insofar as it maximizes plasmon extinction across the wavelengths of interest. Therefore, we examined the relationships between Ag film thickness and maximized surface enhancement through changes to nanostructure morphology and plasmon peak extinction characteristics. SEM images were acquired from Group A before annealing to explore the relationship between film thickness and nanostructure morphology. These images, shown in **Figure II.2**, reveal that Ag was deposited as small islands that grow with increasing film thicknesses from 1 nm (T1) to approximately 5 nm (T5) and become more film-like for depositions of 6 nm (T6) and greater. This change is likely due to surface coverage approaching 100% as a result of increasing Ag mass per area. Extinction

spectra are superimposed on each SEM image in **Figure II.2**, confirming intensified and red-shifted extinction with increasing film thickness. The symmetrical plasmon peaks observed among the lowest Ag depositions (T1 – T4) are consistent with individual, spherical Ag nanoparticles. The transition toward nanostructured thin films (T5 – T9) was accompanied by increasingly exotic nanostructure shapes, associated with increasing asymmetry in the plasmon peaks.

The UV-Vis spectra for all 9 film thicknesses on each of 40 substrates in Group A were processed as described in the Experimental Section above to find peak extinction intensity, wavelength, and breadth in each case. Plasmon extinction intensity increased with Ag film thickness, as shown in **Figure II.3(a)**. Intensity increases approximately linearly for T1 – T5, but begins to approach an asymptotic maximum for T6 – T9. The reduction in differential extinction for high film thicknesses is confirmed by the lack of statistically significant differences between T7 & T8 and T8 & T9 as compared to T1 – T6 in which each thickness group was significantly different from every other thickness group. This change in behavior between thin and thick films correlates with proximity-induced hotspots. When adjacent nanoparticles are within a few nanometers of each other plasmonic coupling results in a hotspot between them, greatly increasing plasmon extinction.[122] For T1 – T5, plasmonic coupling between nanoparticles drove the growth in plasmon extinction intensity as interparticle distances decreased, exhibited by**Figure II.2**. Beginning at T6 however, interparticle gaps ceased to decrease as Ag was deposited. At that point, plasmon extinction intensity began to plateau, which is consistent with Ag accumulation becoming the primary driver for increasing plasmon extinction.
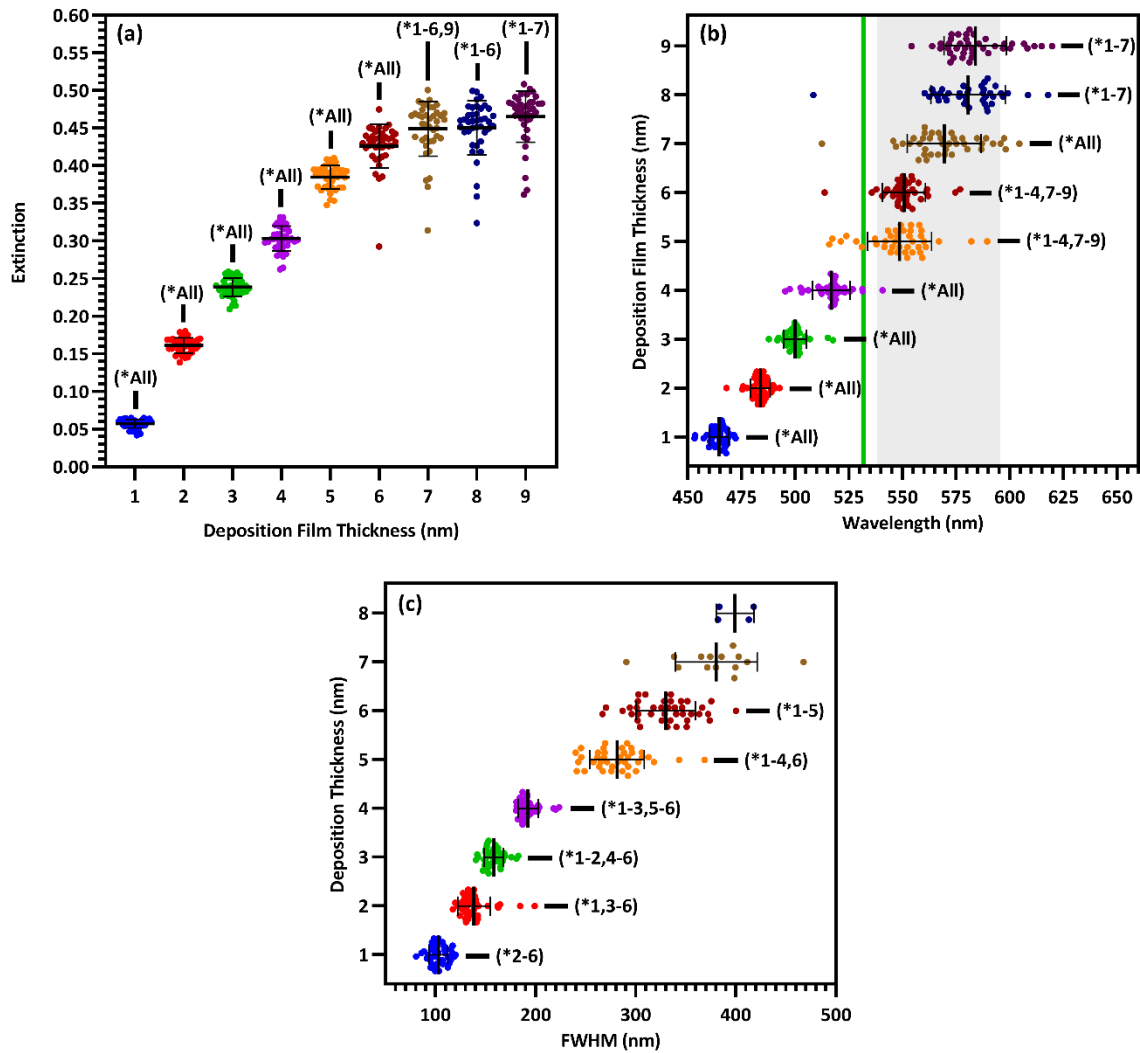
Figure II.3: Scatterplots of plasmon peak (a) intensity (n = 40), (b) wavelength (n = 40), and (c) FWHM (T1 – T4: n = 40, T5 – T6: n = 39, T7: n = 14, T8: n = 4) for each film thickness of substrates in Group A. Green line and shaded region in (b) represent the laser line and fingerprint region, respectively. All data shown with mean and standard deviation of each group, *p <0.05 two-way ANOVA. Statistical significance of the FWHM of 7- and 8-nm films as compared to other films not shown due to an insufficient number of data points to use a parametric test.

Plasmon peak wavelength red-shifted with increasing Ag film thickness, shown in **Figure II.3(b),** from well below the laser line at an average of ~464 nm for 1-nm films, to well past the laser line at an average of ~584 nm for 9-nm films. This redshift was likely due primarily to increasing nanostructure size, which correlated with increasing film thickness (**Figure II.2**).

Nanostructures increased in size from an average of ~30 nm^2 for 1-nm films to an average of ~970 nm^2 for 9-nm films, as shown in **Figure A.4**. Unlike intensity, maximizing surface enhancements requires proximity of the plasmon extinction peak and the laser wavelength, illustrated by the green line in **Figure II.3(b)**. The wavelength of peak plasmon extinction also influences surface enhancement, as the efficiency of optical coupling is enhanced when the laser line is near the plasmon peak. The closest alignment between peak extinction and the laser line was at 517 nm for T4 and 548 nm for T5. Additionally, variability in peak wavelength generally increased as films thickened, with standard deviation growing from 4.2 nm for 1-nm films to as much as 17.3 nm for 8-nm films. We speculate that this behavior is associated with the increasingly exotic nanostructure shapes associated with increasing film thickness.

Maximal surface enhancement requires LSPR with both incident laser light and wave-shifted scattered light. While enhancement is improved when the plasmon extinction peak is close to the laser wavelength, the peak should also be sufficiently broad to enhance wave-shifted scattered light across the fingerprint region which, for organic molecules, usually consists of some portion of the region between 200 and 2000 cm^{-1}. When a 532-nm laser is used to acquire Raman spectra, this fingerprint region translates to 537.7 – 595.3 nm, illustrated by the shaded region in **Figure II.3(b)**.[147–150] Thus, the sensing approach aims for a plasmon wavelength range that usefully overlaps with the entire spectral region of interest. To estimate breadth of the plasmon peak, the FWHM was determined where possible. FWHM of the plasmon peaks correlate with film thickness and range from ~104 nm for 1-nm films to more than 400 nm for 8-nm films, as shown in **Figure II.3(c)**. While this phenomenon provides a greater wavelength range with the potential for useful sensing at the largest deposition thicknesses, it complicated our ability to accurately characterize the FWHM. For substrates with T5 and T6 film thickness, a
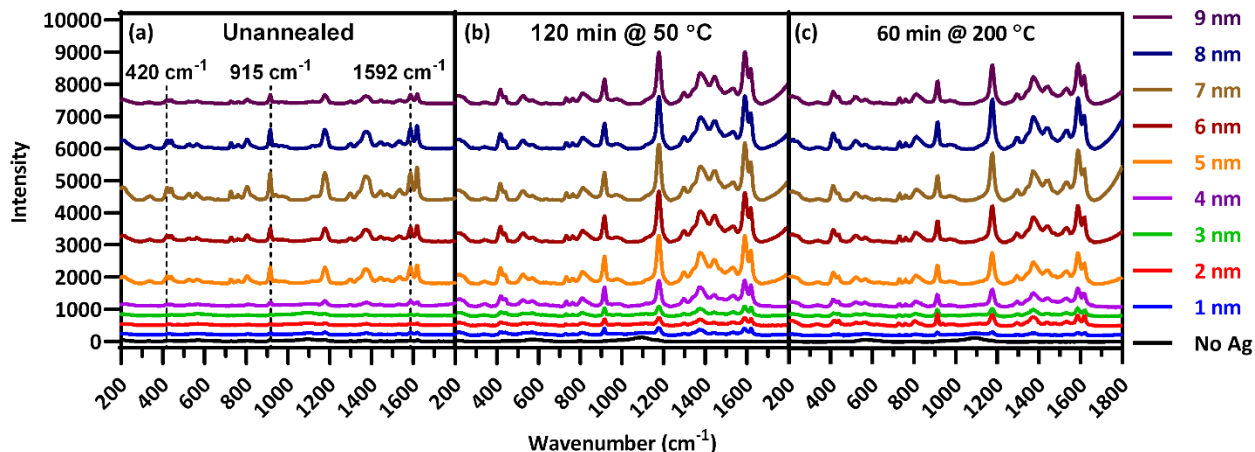
Figure II.4: Raman spectra of CV deposited on each film thickness for substrates (a) unannealed, (b) annealed at 50 °C for 60 min, and (c) annealed at 200 °C for 60 min.

FWHM could be calculated for 39/40 spectrums. For T7, a FWHM could only be calculated for 14/40 spectra. For T8, a FWHM could only be calculated for 4/40 spectra, and for T9, no FWHM's could be calculated. This phenomenon correlated with the increasing asymmetry of the plasmon peaks as films transitioned from individual nanoparticles to nanostructured films, shown in **Figure II.2**. This increasing asymmetry was beneficial for maximizing surface enhancement due to greater plasmon resonance across the fingerprint region.

Analyses of individual plasmon characteristics indicated that the film thickness required to produce maximal surface enhancement would optimize the balance among plasmon extinction intensity, peak proximity to the laser line, and extinction intensity across the fingerprint region. Because these plasmon extinction characteristics interact in non-obvious ways to influence the overall Raman spectra enhancement, SERS spectra of CV adsorbed onto the Ag films were acquired and shown in **Figure II.4(a)** to characterize the role of film thickness on surface enhancement. CV possesses multiple strong Raman peaks, tabulated in **Table A.1** with their associated vibrational modes, across a large portion of the fingerprint region,[151] Very little enhancement was observed for T1 – T4, with the T4 film resulting in less than 5-fold

enhancement across the fingerprint region as compared to the T0 spectrum. This inconsequential enhancement likely resulted from a combination of low plasmon intensity (**Figure II.3(a)**), inefficient coupling between the plasmon peak and the laser line (**Figure II.3(b)**), and insufficient peak breadth to enhance wave-shifted light across the fingerprint region. However, enhancement notably increased starting at T5, with up to 15.8-fold enhancement as compared to the T0 spectrum at 1592 cm^{-1}. Maximal enhancement was found to occur for the T7 film, with up to 25.7-fold enhancement across the fingerprint region at 1592 cm^{-1}, before decreasing with T8 and T9 films. The diminished enhancement for the thickest Ag films is correlated with an increasing departure from the laser line due to red-shifting peak plasmon extinction (**Figure II.3(b)**) accompanied by decreasing rate of plasmon extinction intensification (**Figure II.3(a)**). These results are non-obvious when assessing plasmon peak characteristics individually, illustrating the value in analyzing relationships between these characteristics in light of how they influence surface enhancement. These results demonstrate that film thicknesses of 5 nm or greater provide the best surface enhancement, peaking with 7 nm film thickness. Thus, continued analysis focused on thicker films of 5 nm and above.

Effect of Annealing on Surface-Enhanced Raman Spectroscopy

Following the analysis of deposition thickness, substrates were annealed to explore the effect of annealing temperature and time on plasmon extinction characteristics, toward additionally maximizing surface enhancement. From Group A, 31 substrates from Group A were chosen for this analysis, with the remaining 9 held in reserve should they be needed. Of the 31 substrates, one was set aside as an unannealed control and the remaining 30 were annealed at five temperatures in the range of 50 – 400 °C for six anneal times in the range of 15 – 150 min.
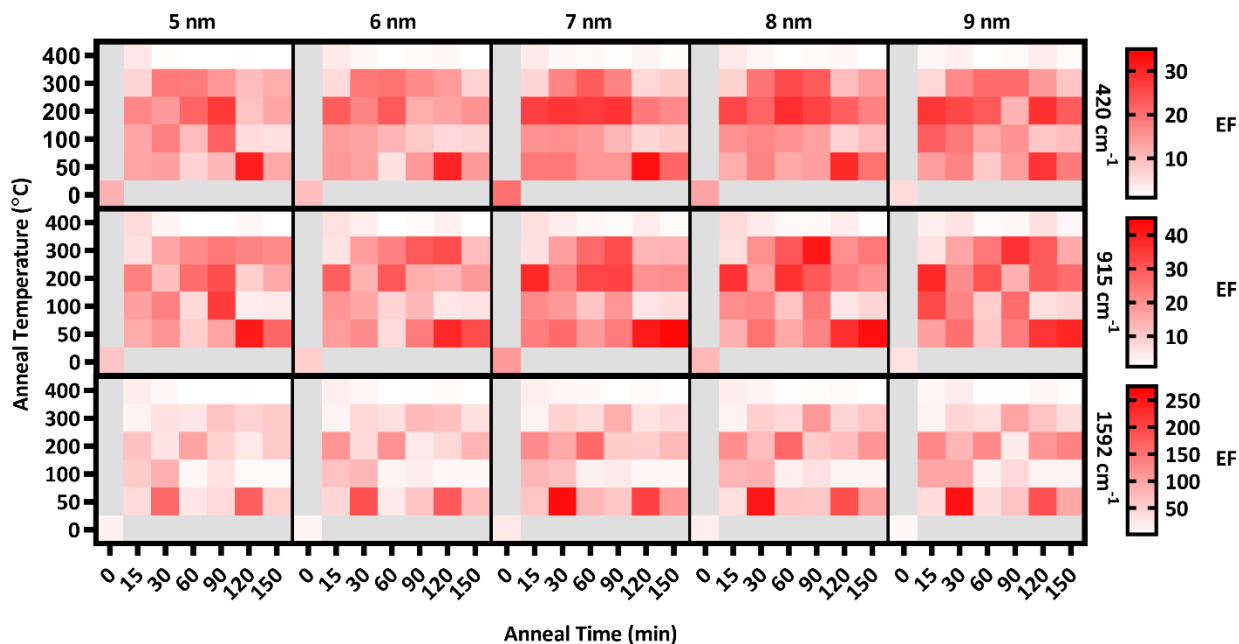
Figure II.5: Heat map of the enhancement factors of T5 – T9 for 420, 915, & 1592 cm^{-1} peaks across all anneal temperatures & times along with the unannealed control.

Raman spectra were acquired of CV adsorbed onto Ag films after annealing, examples of which are presented in **Figure II.4(b,c)**. As with the pre-anneal spectra in **Figure II.4(a)**, film thicknesses of 5 – 9 nm provided the best surface enhancement for both annealed substrates presented in **Figure II.4(b,c)**, peaking at 7 nm. However, the difference in surface enhancement between 7 nm and 5 or 9 nm films is much less pronounced for the annealed substrates than the unannealed substrate. Thus, annealing can be used to obtain near-maximum surface enhancement over a range of film thicknesses. Such flexibility in deposition thickness may be especially useful for three-dimensional sensing substrates such as ZnO nanowires. In such cases, thicker films may over-fill interwire gaps, reducing effective surface area. Because maximal surface enhancement results in part from enhancement of Raman-scattered light across the fingerprint region, three CV peaks at 420, 915, and 1592 cm^{-1} as identified in **Figure II.4(a)** were chosen to quantitatively assess enhancement at multiple points that span the fingerprint region. The enhancement of these peaks was calculated for T5 – T9 at each anneal temperature and time.

38

These enhancements appear as a heat map in **Figure II.5**, where red shading indicates increased enhancement. Annealing produced substantial impact to surface enhancement, but in ways that are nonlinear with respect to time and temperature. Annealing conditions generated changes to surface enhancements ranging from less than 3% to almost 3000% of the unannealed surface enhancement. Clearly, the selection of annealing parameters measurably impacts the performance of these sensors. **Figure II.5** reveals that annealing at 400 °C for even a short time drastically reduced surface enhancement across the board, indicating an upper temperature limit for this sensing paradigm well below 400 °C. Further examination of **Figure II.5** reveals that in general, the anneal time required to maximize surface enhancement decreased as anneal temperature increased. At 50 °C, maximizing enhancement required 120 min while at 100 °C, enhancement dropped off significantly after annealing 90 min. At 200 °C, enhancement was strongest when annealed from 15 – 60 min. Two of these anneal temperatures, 50 °C and 200 °C, produced particularly strong results toward maximizing surface enhancement, motivating closer examination.

Enhancement factors for the five film thicknesses were averaged for each anneal time at each temperature and plotted in **Figure II.6**. The relative strength of enhancement between the two anneal temperatures varies across the three CV peaks, indicating the necessity of investigating enhancement across the entire fingerprint region. For instance, annealing at 30 °C resulted in opposing enhancement trends for the two anneal temperatures. Relative enhancement decreased farther away from the laser wavelength when annealed at 200 °C while it increased away from the laser wavelength when annealed at 50 °C. Among this variability, two anneal times produced consistently strong surface enhancement at these temperatures: 60 min at 200 °C and 120 min at 50 °C.
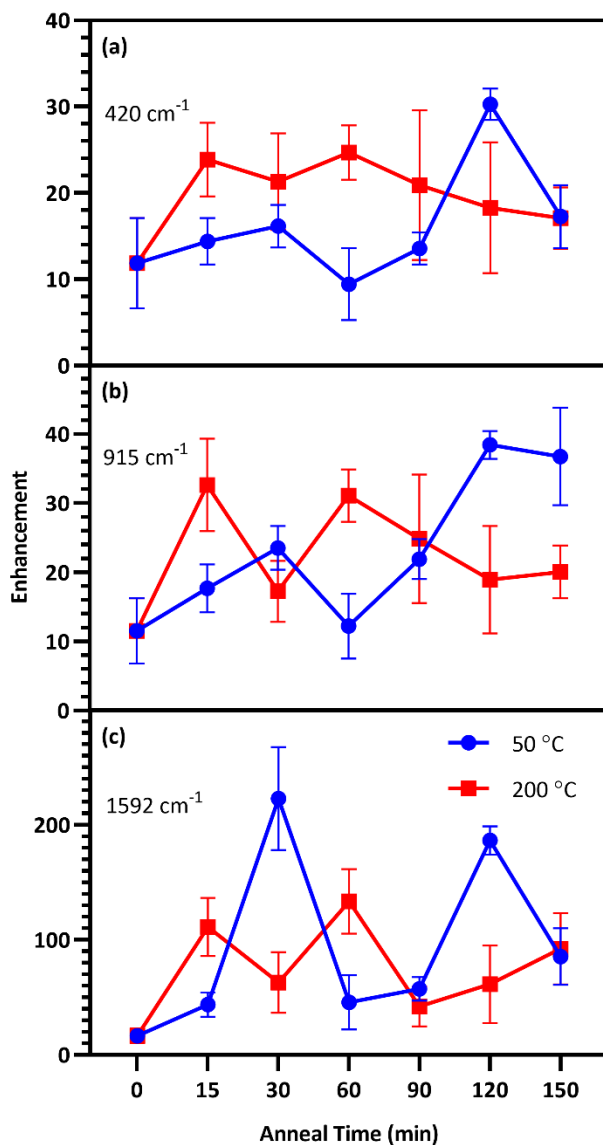
Figure II.6: SERS EFs of substrates annealed at 50 °C (blue) and 200 °C (red) for up to 150 min, along with the unannealed control for the (a) 420 cm^{-1}, (b) 915 cm^{-1}, and (c) 1592 cm^{-1} peaks. Each point in the figure exhibits the mean and standard deviation of the EFs for T5 – T9.

This study seeks to not only describe the deposition and annealing parameters that result in maximal surface enhancement, but also relate these results to changes in plasmon extinction characteristics effected by those fabrication parameters. To this end, changes to plasmon extinction characteristics for all five effective film thicknesses (T5 – T9) due to annealing at 50 and 200 °C were plotted in **Figure II.7**. Annealing at 200 °C caused the plasmon intensity of all
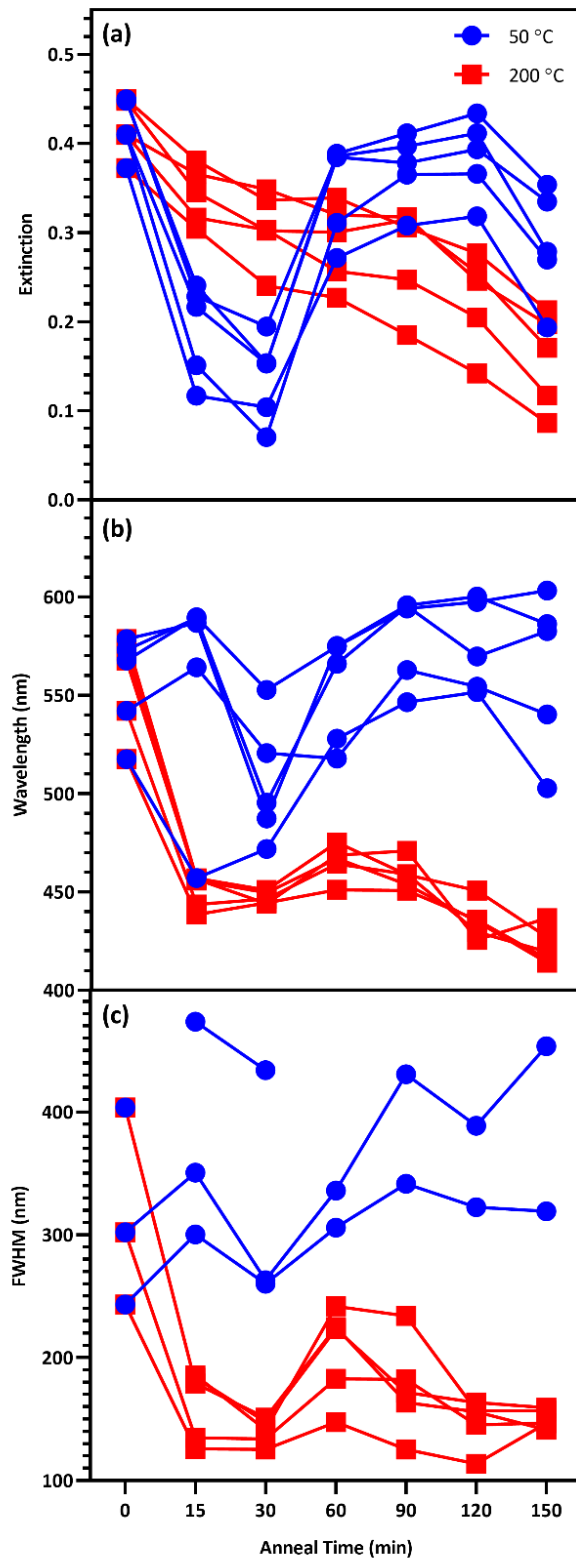
Figure II.7: Change to the plasmon peak (a)intensity, (b)wavelength, and (c)FWHM due to anneal time at 50 °C (blue) and 200 °C (red) for T5 – T9.

five film thicknesses to decrease steadily with increasing anneal time. In addition, annealing for

15 min or more at 200 °C blue-shifted the plasmon peaks. Annealing for 60 min slightly red-

shifted the peaks, which blue-shifted again at higher anneal times (> 90 min). This blue-shifting

behavior is consistent with increasing nanostructure uniformity due to Ostwald ripening,

reducing the exotic nature of nanostructure shapes. FWHMs followed a similar behavior as peak

wavelengths, with a short anneal time narrowing the plasmon peaks. These plasmon peaks

widened slightly when annealed for 60 min before narrowing again beyond 90 min. These

observations agree with the results in **Figure II.6**, indicating that annealing at 200 °C generated

the best combination of plasmon intensity, peak wavelength, and peak width at 60 min of anneal

time.

Annealing at 50 °C for less than 60 min reduced peak intensity that rebounded for anneal

times of 60 – 120 min. Peak wavelength blue-shifted slightly following annealing for less than

60 min at 50 °C before subsequent red-shifting for annealing times of 60 – 120 min. FWHMs for

5- and 6-nm films were increased with increasing anneal time. These results agree with the

results in **Figure II.6** that indicate an optimum anneal time of 120 min at 50 °C. We anticipate

that deposition and dewetting kinetics differ between the ZnO films used in this work and ZnO

nanowires often utilized in 3D SERS substrates. However, this work expedites future

nanoparticle optimization by narrowing the window of parameters values to explore in future

works involving ZnO nanowires.

Effect of Deposition Rate on Surface Enhanced Raman Spectroscopy

Deposition rate had a significant impact on plasmon peak wavelengths, with films

deposited at 0.3 Å/s exhibiting significantly red-shifted peaks compared to a deposition rate of

0.1 Å/s for each film thickness examined, excepting 7 nm, as shown in **Figure A.5(b)**. We hypothesize that this behavior can be explained by rate-induced differences in the crystal structure of Ag nanoparticles, as deposition rate has been shown to effect such crystal properties as grain size, dislocation density, and twin boundary density in metallic nanostructures.[141] These results suggest that the plasmon characteristics of e-beam deposited Ag films are sensitive to deposition rates, as small changes can have a significant impact on important physical characteristics of the nanoparticles. These results also clearly indicate the trade-off between degraded sensor performance and the reduced deposition time achieved at elevated deposition rate.

While there was no significant difference in terms of enhancement in the unannealed controls between Groups A (0.1 Å/s) and B (0.3 Å/s), **Figure A.6** demonstrates that annealing the substrates in Group A generally produced more surface enhancement than Group B, across all film thicknesses, and anneal temperatures/times. This suggests that rate-induced differences in the crystal structure of Ag nanoparticles impacts annealing-induced effects on surface enhancement. This observation further emphasizes the important impact of deposition rate on the physical characteristics of Ag nanoparticles and the resulting surface enhancement of the structure.

Several combinations of fabrication and anneal parameters maximize surface enhancement by optimizing plasmon extinction. This study substantially improves the potential for fabricating high-performance sensors through elimination of fabrication parameters that yield low-enhancement materials. Importantly, these results demonstrate that maximal surface enhancement can be achieved by multiple different fabrication strategies. For instance, 2D sensing surfaces where film thickness does not impact device function have the best

enhancement with a 7 nm thick surface deposited at 0.1 Å/s and annealed at 200 °C for 60 min. However, for 3D sensing surfaces such as the ZnO nanowire-based structure described in our previous work,[127] a thicker sensing surface could reduce device functionality by over-filling the spaces between nanowires, thereby reducing effective surface area. In such cases, a film approximately 5 nm thick, deposited at 0.1 Å/s and annealed at 200 °C for an hour is predicted to provide near-maximal surface enhancement without sacrificing sensing surface area. Another consideration is the substrate on which such nanostructures are fabricated. Many sensing strategies utilize substrates with high melting points such as glass or fused silica. In such cases, annealing at 200 °C is not problematic. However, increasing attention has been devoted in recent years toward fabricating SERS-active structures on flexible substrates made of materials like polyvinyl alcohol (PVA),[152,153] poly(dimethylsiloxane) (PDMS),[154] or polyvinylidene fluoride (PVDF).[155] In such cases substrates, even temperatures as low as 100 °C can have an undesirable effect on the substrate itself, such as increasing brittleness. For such device designs, excellent surface enhancement can be achieved by annealing substrates at 50 °C for 120 min.

CONCLUSIONS

This study provides guidance for the fabrication of sensors with maximal SERS enhancement excited with a 532-nm laser through e-beam deposited Ag nanoparticles on ZnO. 7-nm Ag films possess the optimal combination of plasmon peak intensity, wavelength, and breadth for maximal surface enhancement with a 532-nm laser. When 7-nm films are untenable, films as thin as 5 nm still provide near-maximal surface enhancement. We demonstrated that annealing at temperatures up to 200 °C for one to two hours further improved surface enhancement, but annealing at 200 °C for one hour or 50 °C for two hours resulted in the greatest

increase to surface enhancement. Lastly, we discovered that Ag deposition rate significantly influences surface plasmon extinction peak characteristics. Increasing deposition rate from 0.1 to 0.3 Å/s resulted in decreased surface enhancement at all anneal times and temperatures, making 0.1 Å/s the clearly preferable deposition rate. The results presented in this study fill a vital need for guidance in determining fabrication and annealing parameters for maximal SERS with e-beam deposited Ag nanoparticles with a 532-nm laser. We presume that similar fabrication relationships control the performance of other SERS substrates based on metal nanoparticles. This is the first report to begin to explore the impact of fabrication choices on the performance of a specific SERS sensor, but lays the groundwork for the assessment of similar phenomena in other Raman sensing approaches.

CHAPTER III

FABRICATION OF SILVER-DECORATED ZINC OXIDE NANOWIRE SENSOR IN
MICROCHANNELS FOR SURFACE-ENHANCED RAMAN SPECTROSCOPY

ABSTRACT

Surface-enhanced Raman spectroscopy (SERS) performed in microfluidic channels offers multiple benefits to sensitive and reliable detection of dilute analytes while utilizing the advantages of microfluidics, including small samples, high throughput, and portability. Physical deposition of metallic nanoparticles by techniques such as electron beam deposition results in dense populations of nanoparticles and hotspots between nanoparticles for sensitive detection. However, not only do physically deposited SERS-active surfaces necessitate additional steps during device fabrication, but surface fabrication is itself complicated by the constraints imposed by the microfluidic channel. This work demonstrated a robust approach to physical fabrication of a SERS-active substrates inside a poly(dimethylsiloxane) (PDMS) microfluidic channel. Direct growth of zinc oxide nanowires inside the PDMS channel and e-beam deposition of silver to coat the nanowires was performed before bonding PDMS to glass. This process enabled label-free SERS sensing of micromolar crystal violet and melamine with minimal spectral interference from the PDMS-based channel.

INTRODUCTION

Surface-enhanced Raman spectroscopy (SERS) that is integrated with microfluidic technology offers the advantages of reduced sample consumption and reaction time, high detection efficiency, and portability as compared to state-of-the-art detection paradigms.[156] This

46

integration is primarily pursued through either colloidal solutions[79,157] or stationary

substrates.[158–160] Co-injection of SERS-active colloids with samples into microfluidic channels

can provide efficient sensing and heat-dissipation, although this technique often suffers from

aggregation, resulting in reduced reproducibility and poor mixing due to predominantly laminar

flow in microfluidic channels.[161] Stationary substrates offer greater stability and reproducibility,

although they are often less efficient than colloidal strategies because stationary substrates

cannot be dispersed within sample fluids.[55,78]

SERS-active substrates based on nanowires decorated with metal nanoparticles such as

silver (Ag) or gold (Au), can minimize the drawbacks associated with colloidal or stationary

substrate sensing when fabricated within a microfluidic channel. This design offers the stability

and reproducibility similar to stationary substrates, but can also provide the sensing efficiency of

colloidal strategies due to their inherent 3-dimensional architecture.[127,129] Metal-decorated zinc

oxide (ZnO) nanowires are an attractive platform for SERS sensing. ZnO is a biocompatible[134]

wide direct-bandgap semiconductor with a band-edge emission of 3.3 eV[81] and a high exciton

binding energy of 60 meV.[135,136] These properties make ZnO nanowires electronically stable at

room temperature[135] and transparent to visible and NIR light,[83] reducing absorption of Raman

scattered photons. Optical transparency is ideal for Raman spectra acquired through the substrate

as is necessitated by the sensor and detector geometry we anticipate in microfluidic technology.

In addition, ZnO has been demonstrated to increase surface enhancement due to charge transfer

between ZnO and both Ag[137] and analytes directly adsorbed to the nanowires.[84] Additionally,

ZnO possesses high electron mobility[87] and a large refractive index of approximately 2.0 in the

visible region.[86,138] Combining these characteristics with the atomically smooth and highly

faceted hexagonal single-crystal structure of ZnO nanowires can induce Mie scattering

resonances. Mie scattering can reduce signal loss to scattering through waveguiding light.[85] and synergize with charge transfer to enhance Raman scattering up to 10^5, in addition to the electromagnetic mechanism of SERS.[88]

During the fabrication of SERS-active microchannels, stationary substrates such as the Ag-decorated ZnO nanowires are usually fabricated on the glass wall of the channel. This is done to avoid spectroscopic interference by polymers commonly used to fabricate microfluidic channels such as poly(dimethysiloxane) (PDMS) that has its own strong Raman spectrum. ZnO nanowire fabrication on glass lends itself to *in situ* fabrication techniques like hydrothermal growth and electroplating after microchannel fabrication. In particular, metal-decorated ZnO nanowires can be easily fabricated *in situ* hydrothermally,[129,162,163] however hydrothermal fabrication typically results in sparse metal nanoparticle formation.[129] In contrast, electron beam (e-beam) deposition as a physical technique forms denser nanoparticle distributions,[85,127] resulting in higher surface enhancement due to proximity-induced hotspots between nanoparticles.[125] However, one major drawback is that physical deposition of nanoparticles necessitates *ex-situ* SERS substrate fabrication on glass prior to microfluidic channel bonding because closing the channel prevents deposition of material from an external source. Alignment of the SERS sensor on glass with a microchannel in PDMS is complicated by microscale dimensions and the deformability of PDMS. The complexity of accurate placement in PDMS microchannels is amplified for designs that include multiple SERS sensors on a single glass substrate. Additional alignment steps limit flexibility of microchannel design.[161] making it less ideal for the production of large numbers of disposable sensors. Fabricating SERS substrates directly into PDMS microchannels before bonding with glass as illustrated by **Figure III.1**
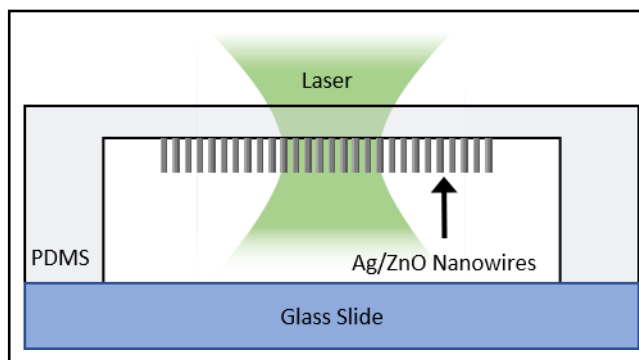
Figure III.1: Illustration of the cross-section of a microchannel integrated with an Ag/ZnO nanoprobe fabricated on the PDMS.

enables the fabrication of complex multisensory, multichannel devices in the absence of rigorous alignment requirements.

In this study, we demonstrated that a ZnO nanowire substrate decorated with e-beam deposited Ag nanoparticles can be simply fabricated within a PDMS microchannel *ex-situ* without requiring an alignment step to complete microchannel fabrication. Furthermore, we demonstrated that trace chemical and biological analytes can be detected through a PDMS microchannel wall by careful optimization of device design and analysis of SERS optical signals.

EXPERIMENTAL

In order to simplify the fabrication of a SERS-integrated microfluidic channel, Ag-decorated ZnO (Ag/ZnO) nanowires were fabricated directly into the channel such that the nanowires would reside on the "roof" of the channel after bonding with glass, as illustrated by Figure 1. In this orientation, Raman spectra would be acquired through the "roof" of the channel. The first step in accomplishing this is to examine the effect of PDMS thickness on spectral intensity, as crosslinked PDMS polymer is known to scatter light.[164] and Mao *et. al.* demonstrated 4× reduced SERS sensitivity when acquiring spectra through a PDMS cap.[165] Next, the applicability of SERS through PDMS must be exemplified through SERS of a relevant

analyte. Melamine was chosen for this purpose due to strong Raman peaks in regions where

PDMS signal is weak. Melamine is an industrial material primarily used in polymer

manufacturing that has also been added to dairy products to produce artificially high readings of

protein content. Because melamine can cause kidney failure and even death, the Codex

Alimentarius set a limit of 1 mg/L (7.93 µM) of melamine in powder infant formula.[118] Lastly,

using information gained from the previous two experiments, a PDMS channel must be designed

and fabricated. The Ag/ZnO nanowire substrate must be constructed within the channel and

SERS of crystal violet injected into the channel must be acquired.

Zinc Oxide Seed in PDMS Channel

SERS-active nanostructures were fabricated directly into the channel, such that they

would reside on the 'roof' of the channel as shown in **Figure III.1**. Substrates and microchannels

were fabricated from PDMS via soft lithography with Sylgard 184® (Dow Corning, Batch

#H047ICL055) which consists of a liquid PDMS base and a curing agent. A microchannel

master was designed in AutoCAD® 2017 as a mold for PDMS microchannels and machined

from aluminum, shown in **Figure B.1**. The base and curing agent were mixed at a 10:1 ratio and

poured over the base. The solution was then placed in a vacuum chamber at ~25 mmHg until all

bubbles were removed. The lid was fitted onto the base before the dish was placed in the oven at

95 °C for two hours to cure the PDMS, after which the dishes were removed and allowed to cool

at room temperature. After cooling, the master was cut away from the surrounding PDMS and

the microchannels were extracted.

PDMS microchannels were cleaned with the ALD-AMD method[127] which consists of

submersion in a 1% Alconox® solution, deionized (DI) water, acetone, methanol, and DI water,

sequentially. At each step, the substrates were sonicated for 10 minutes. After this cleaning process was completed, the substrates were dried using nitrogen gas. For each microchannel, Kapton tape was used to mask the PDMS surface containing the channel so that only the channel was exposed. Microchannels were then mounted in a sputter deposition system (Angstrom Amod Multimode Deposition Chamber) which was pumped down to 5.5×10^{-6} Torr, and ZnO was deposited in the channel over the course of 1 hour and 40 minutes. Stylus profilometry (Bruker Dektak 150) was used to measure the thickness of ZnO across the channel. The maximum ZnO thickness was 150 nm at the center of the channel, and dropped off to 0 nm at the corners of the channel. ZnO was sputtered to ensure ZnO deposition on all sides of the channel, thereby minimizing the impact of PDMS hydrophobicity on hydrothermal nanowire growth. The channels were annealed at 100 °C overnight to improve ZnO seed surface morphology and subsequent nanowire growth.

Zinc Oxide Seed on PDMS Substrates

PDMS substrates were fabricated for two purposes in this work. First, it was necessary to explore the effect of PDMS thickness on the quality of Raman signal, since the crosslinked polymeric nature of cured PDMS scatters light.[164] Results of this exploration informed the design of the PDMS channel used in this work. Second, thin PDMS substrates were fabricated to characterize SERS of melamine through PDMS. These substrates were designed to mimic the thickness of the PDMS channel wall through which spectra of crystal violet were acquired.

To explore the effect of light scattering through PDMS on SERS signal quality, bare ZnO nanowires and Ag nanoparticle-decorated ZnO (Ag/ZnO) nanowires were constructed on thick and thin PDMS substrates, fabricated via soft lithography with Sylgard 184®. Substrate

thickness was controlled by varying the PDMS volume placed into Pyrex® petri dishes (95 mm diameter). 7.0 g of PDMS was poured into one petri dish, and 1.4 g of PDMS was poured into another, targeting 1.0 mm and 0.2 mm PDMS thicknesses for thick and thin substrates respectively. After oven-curing, PDMS squares of approximately 1 cm x 1 cm were cut from the center of each petri dish to form substrates for sensor fabrication. The substrates were cleaned via the ALD-AMD method and the thickness of each substrate was determined via stylus profilometry to be ~1.0 mm for the thick substrates and ~0.17 mm for the thin substrates. The discrepancy between the targeted thickness of 0.2 mm and the resultant thickness of 0.17 mm was caused by capillary action drawing PDMS up along the walls of the petri dish. Subsequent substrates fabricated for SERS of melamine were fabricated with controlled thickness by pouring PDMS between two glass slides with a single layer of 0.15-mm thick carbon tape as a spacer. This resulted in 0.15-mm thick PDMS substrates. Cleaned substrates were mounted in an e-beam deposition chamber (Thermionics, 150-0040). The chamber was pumped down to a vacuum of 5×10^{-6} Torr and a 100 nm ZnO seed layer was deposited at a rate of ~0.1 Å/second. PDMS substrates were mounted in a plan configuration throughout ZnO deposition.

Zinc Oxide Nanowire Growth

The ZnO nanowire growth process is similar to that described in previous work.[127] ZnO nanowires were grown hydrothermally. PDMS channels and substrates were submerged in a 20 mM equimolar solution of zinc acetate dihydrate (Sigma Aldrich, BCBM3068V) and hexamethylenetetramine (Sigma Aldrich, MKBS8102V) in a Teflon reaction chamber. This chamber was placed in a preheated oven at 95 °C for 2.5 hours, after which the chamber was rapidly cooled under running water. The channels and substrates were washed of residual

organics with DI water, then placed in the oven at 105 °C for ~10 minutes to dry. Nanowires were grown only where seed layer was deposited.

Ag Nanoparticle Fabrication

ZnO nanowires on PDMS substrates were decorated with Ag nanoparticles via e-beam deposition (Thermionics, 150-0040) as shown in **Figure B.2**. The nanowire substrates were mounted on a glancing-angle deposition apparatus, which rotates azimuthally at an angle during deposition. This angle was calculated by **Equation (III.1)** to maximize the area of nanowire sides exposed to deposition while minimizing shadowing from adjacent nanowires. L_n and D_n, which are average nanowire length and spacing, were estimated to be 320 and 76 nm, respectively. From these, an angle of θ_{dep}= ~13° was calculated. The deposition chamber was depressurized to ~5.0×10^{-6}, at which point Ag was deposited at a rate of ~0.1 Å/s to a nominal film thickness of 10 nm while the stage was rotated. This resulted in an effective film thickness ~2.2 nm on the sides of the nanowires as calculated by **Equation (III.2)**, where t_{nom} represents the nominal film thickness and θ_{dep} represents the angle of deposition specified above.

$$\theta_{dep} = \text{TAN}^{-1}\left(\frac{D_n}{L_n}\right) \tag{III.1}$$

$$t_{eff} = t_{nom}\sin(\theta_{dep}) \tag{III.2}$$

Ag nanoparticles were deposited in PDMS channels via e-beam deposition (Angstrom Amod Multimode Deposition System) as shown in **Figure B.3**. The nanowire substrates were mounted with a Kapton-tape mask such that only the channel was exposed on a stage at an angle of approximately 24° from the source crucible. The chamber was pumped down to a pressure of ~4.0×10^{-6} Torr. Ag was deposited at a rate of ~0.1Å/s to a nominal film thickness of 15 nm while the stage was rotated. This resulted in an effective film thickness (t_{eff}) of ~6.1 nm on the

sides of the nanowires, and ~13.7 nm on the bottom of the channel. This effective film thickness is within the range of 5 – 9 nm film thickness demonstrated in Chapter II[102] to maximize SERS acquired with a 532-nm laser. The mask was designed to allow Ag deposition only inside the channel. After deposition, the microchannel was heated to 50 °C for 2 hours to anneal the nanoparticles, which was shown in Chapter II to greatly increase surface enhancement.[102]

Microfluidic Chip Fabrication

After fabrication of Ag-decorated ZnO nanowires inside the microchannels, holes were punched at the inlet and outlet with a 2-mm disposable biopsy punch (Premier® Uni-Punch®) and they were placed in a plasma oxidation chamber (Harrick Plasma PDC-001) for 4 minutes to oxidize the PDMS surface. This enabled bonding to a glass slide (Fisherbrand® 12-550-A3). Lastly, Tygon® tubing (ID: 0.020 in.; OD: 0.060 in.) was inserted at the inlet and outlet and PDMS was used to seal the interface between PDMS and tubing

Characterization Techniques

Scanning electron microscopy images of bare and Ag-decorated ZnO nanowires were acquired with a Zeiss Merlin scanning electron microscope (Jena, Germany) in both plan and 45° configurations. These images were used to visually inspect nanowire and nanoparticle morphology. All image analysis was performed using ImageJ.

Photoluminescence (PL) spectra of ZnO nanowires were acquired to assess nanowire crystallinity using a thermoelectrically cooled (-40 °C) CCD camera in a spectroscopy setup (HORIBA Jobin Yvon LabRAM 800HR). ZnO nanowire emissions were excited using a 325-nm He-Cd laser (Kimmon, 1 K series 200 mW, vertically polarized output measured at the laser

head). PL spectra were acquired with a 15×-magnification objective lens (Thorlabs, LMU-15×-NUV, NA = 0.32), and detected in line with the laser normal to the substrate surface. Nanowires were oriented facing incident light. Five locations on each patch of nanowires were chosen, with a precision of 100 μm. At each location, a PL spectrum was acquired over a wavelength range of 340-700 nm. Each spectrum was the accumulation of 4 background-subtracted spectra, each taken with a 200-μm aperture, and a 600 grooves/mm grating. Exposure time was 0.1 seconds and laser power was between 4.0 – 5.0 mW, as measured at the lens. The five spectra for each patch were averaged to produce a representative PL spectrum for each patch of nanowires within the channel.

To characterize the effect PDMS-induced scattering on spectral quality, SERS spectra of crystal violet in solution were acquired through Ag/ZnO and bare ZnO nanowires on 1.0-mm and 0.17-mm substrates to compare SERS and non-SERS spectra. These spectra were acquired using a CCD camera on the same spectroscopy setup as the PL measurements with a 532-nm laser (Ventus, 500 mW, horizontally polarized output measured at the laser head) and a 10x-magnification lens (Olympus, MPlan N Achromat, NA = 0.25). Raman scattering was collected in line with the laser normal to the substrate surface. PDMS substrates were affixed face down in a reservoir filled with 25-μM crystal violet, with the Ag-decorated and bare ZnO nanowires oriented away from incoming laser light. Raman spectra were acquired over a range of 100 – 1800 cm^{-1}, and enhancement factors were estimated from these spectra as described in our previous work.[127] Each Raman spectrum was the accumulation of two background-subtracted spectra, taken with a 20-s exposure time, a 200-μm aperture, and a 1800-grooves/mm grating. Laser power was 10.0 mW, measured at the turret. Raman spectra background was subtracted using a proprietary intelligent fitting algorithm developed by Renishaw.[166] The algorithm used an

11th order polynomial and a noise tolerance of 1.50. Spectra were smoothed using a Savitzky-Golay filter. Crystal violet was chosen for this purpose to facilitate detection due to its multiple strong Raman peaks where the PDMS Raman signal is weak. These spectra were intensity normalized using the 687 cm^{-1} PDMS peak.

There was also concern that the ALD-AMD cleaning method would change the Raman spectrum of the PDMS by introducing solvents into the PDMS. Curling of the substrates was observed after the cleaning process due to the presence of acetone and methanol. To address this concern, nine Raman spectra were acquired of a single PDMS substrate before cleaning and averaged, using the same system and conditions detailed for the spectra acquired through thick and thin PDMS. After cleaning, Raman spectra were acquired at the same locations as before and averaged. These spectra were intensity normalized using the 488 cm^{-1} PDMS peak.

Raman spectra of melamine through 0.15-mm thick PDMS were acquired with the same system described above. Raman spectra used to quantify SERS were acquired in a range of 200 – 1800 cm^{-1} for two Ag-decorated ZnO nanowire substrates deposited on 150 μm-thick PDMS, hereafter referred to as S1 and S2. Each Raman spectrum acquired through S1 was the accumulation of four background-subtracted spectra, each taken with a 10-s exposure time. Each Raman spectrum acquired through S2, was the accumulation of 8 background-subtracted spectra, each taken with a 1-s exposure time. All Raman spectra of melamine were acquired with a 200-μm aperture, and a 600-grooves/mm grating. Laser power was 5 mW, measured at the turret. Raman spectra background was subtracted using an asymmetric least squares method, and smoothed with a Savitzky-Golay filter.

Raman spectra of crystal violet injected into the SERS-integrated PDMS channel were acquired with Thermo Scientific DXR Raman microscope (Waltham, MA, USA). A 532 nm

diode-pumped, solid state (DPSS) laser was used with a 50× objective (Olympus, MPlan N Achromat, 0.75 NA) at a power of 10 mW as measured at the objective turret. These spectra were intensity normalized using the 488 cm^{-1} PDMS peak. Raman spectra were acquired through the PDMS channel "roof" bearing Ag/ZnO nanowires over a range of 100 – 1800 cm^{-1}. Each Raman spectrum was the accumulation of 4 background-subtracted spectra, each taken with a 60 second exposure time, a 50-μm slit aperture, and 900 grooves/mm grating. Laser power was 10 mW, as measured at the objective and Raman scattering was detected in-line with the laser normal to the surface of the sample. Raman spectra background were subtracted using a 5th order polynomial and smoothed with a Savitzky-Golay filter. These spectra were intensity normalized using the 488 cm^{-1} PDMS peak.

To characterize the plasmonic properties of Ag nanoparticles, ultraviolet-visible-near infrared (UV-vis-NIR) extinction spectra were acquired using a Hitachi U-4100 spectrophotometer with an integrating sphere. Extinction spectra were acquired at a rate of 300 nm/min over a range of 350 – 850 nm, with the nanowire substrate oriented facing oncoming light.

RESULTS & DISCUSSION

Effect of Cleaning on PDMS Raman Spectrum

Because SERS-active nanostructures were fabricated on a PDMS surface of the microchannel, SERS will be performed through that PDMS wall. Because PDMS is porous, it is known to absorb multiple solvents used during the ALD-AMD cleaning process.[167,168] Indeed, curling of substrates was observed after cleaning, although subsequent placement of the

substrates in a vacuum reduced this curling. It is essential that the Raman spectrum of PDMS be consistent in order to reliably extract signal from dilute analytes, so Raman spectra were acquired before and after the cleaning process to determine whether solvent absorption had an observable effect on the spectrum of PDMS. A comparison of these Raman spectra exhibited only Raman peaks associated with PDMS, as shown in **Figure B.4**. Thus, the cleaning process demonstrably did not affect the Raman spectrum of PDMS.

ZnO Nanowire Characterization

To be suitable as a platform for SERS enhancements, ZnO nanowires must possess two characteristics: 1) the nanowires must be high quality, which means they grow as single crystals with little to no defects, and 2) Ag/ZnO nanowires must possess uniform dimensional and structural properties, such as crystallinity. SEM images of nanowires (**Figure B.5**) show a dense bed of hexagonal nanowires, indicating single-crystallinity. A visual comparison of nanowires to remain bare and those to be decorated with Ag in **Figure B.6** revealed no visible difference in the dimensionality or structure of the nanowires, providing validation for the quantification of SERS enhancements. Furthermore, SEM images revealed nanowires that are long enough to provide large surface area for SERS, but not so long as to induce nesting. Nesting would introduce shadowing during nanoparticle deposition, reducing nanoparticle coverage.

PL spectroscopy was used to assess the crystallinity of the ZnO nanowires. ZnO is a direct bandgap semiconductor with a band-edge emission of ~3.4 eV at room temperature,[136] which means that PL spectra of crystalline ZnO nanowires will have a sharp band-edge emission peak around 380 nm. Any native point defects within the crystalline structure, such as vacancies (missing atoms at regular lattice locations), interstitials (extra atoms occupying lattice

interstices), or antisites (atoms occupying a lattice site where it doesn't belong) introduce transition levels within the bandgap which induce emissions at wavelengths in the visible region.[169] This defect emission is very broad compared to the band-edge emission, and the ratio of band-edge to defect emission in ZnO nanowires is an indicator of the nanowires' crystallinity.[170] PL spectra of the nanowires in **Figure B.7** exhibit very little defect emission and very strong band-edge emission, providing further evidence of high crystallinity with few defects. While the band-edge emission peak at 392 nm is shifted slightly for nanowires grown on PDMS versus the band-edge emission of 380 nm previously reported for nanowires similarly grown on fused silica,[170] the ratio of band-edge to defect emission remained similarly large. A comparison of the PL spectra for nanowires to remain bare (nonSERS) and those to be decorated with nanoparticles (SERS) revealed little variation. 5 PL spectra were acquired of each population and averaged. The band edge and defect emission for nonSERS exhibited a relative standard deviation (RSD) 2.4% and 3.4% respectively, while the SERS nanowires exhibited an RSD of 5.9% and 3.5% for band-edge and defect emission. The average band-edge peak intensity for nonSERS nanowires was within 10% of that for SERS nanowires, indicating that the nanowire populations had similar nanowire density and dimensions. The ratio between band-edge emission and defect emission in the visible region was ~56.9 for SERS nanowires and ~46.4 for nonSERS nanowires, indicating that both populations were highly crystalline with few defects. These features indicated that light would interact with both nanowire populations similarly, enabling high confidence in the comparison of non-SERS to SERS spectra.

To explore the possibility of patterning ZnO nanowire growth by patterning the ZnO seed layer deposition, a partially shielded PDMS substrate was deposited with a 100-nm seed layer, on which nanowires were hydrothermally grown. UV-Vis-NIR spectra of the seeded and non-

seeded portions of the substrate (**Figure B.8**) indicated nanowire growth on the seeded portion of the substrate and negligible nanostructure formation on the unseeded portion.

Ag Nanoparticle Deposition Characterization

ImageJ analysis of the SEM images of bare nanowires grown on PDMS substrates revealed an approximate nanowire height of 320 nm and approximate interwire spacing of 76 nm. Plugging these values into **Equation (III.1)** resulted in a Ag deposition angle of ~13°. SEM image of the nanowires after nanoparticle deposition revealed a dense population of resulted in an Ag deposition angle of ~13°. SEM image of the nanowires after nanoparticle deposition revealed a dense population of nanoparticles on the nanowire sides (**Figure B.6**). UV-Vis-NIR extinction spectra of Ag/ZnO nanowires before and after Ag deposition revealed a plasmon absorption peak centered at ~450 nm (**Figure B.9**).

Effect of PDMS Thickness on Surface Enhancement

To quantify SERS, Raman spectra were acquired of a 25-µM solution of crystal violet dye in DI water through both bare ZnO nanowires and Ag/ZnO nanowires for both PDMS thicknesses. Representative examples of these spectra are shown in **Figure III.2**. The SERS intensity was greater for thin PDMS than for thick. This difference was due to increased light scattering through thick PDMS, resulting in less Raman-scattered light reaching the detector. Crystal violet has several strong bands in the fingerprint region of its Raman spectra that can be decoupled from the strong Raman peaks of PDMS, shown in (see **Figure B.4**). Furthermore, plasmonic nanoparticles used for SERS are separated from PDMS by at least 100 nm, which was the thickness of the ZnO seed layer. This is more than enough to ensure that the PDMS Raman

contributions do not experience significant surface enhancements. Enhancement was quantified for 13 individual crystal violet Raman peaks distinguishable from the PDMS background in non-SERS spectra, tabulated with their raw enhancement through thick and thin PDMS in **Table III.1**. Raw enhancement, simply the difference in peak intensity between SERS and non-SERS spectra, ranged from an average of 2.2-fold for spectra taken through thick (~1 mm) PDMS to an average of 130-fold for spectra taken through ~0.17-mm thick PDMS, as shown in **Figure III.3**, demonstrating the impact that PDMS thickness has on the magnitude of enhancement observed. While more PDMS thicknesses would be required to establish a relationship between PDMS thickness and surface enhancement, this data demonstrates that enhancement is inversely related to PDMS thickness. Thus, it is vital to control the thickness of the PDMS cap through which analysis is performed. Multiple parameters must be considered in order to optimize PDMS thickness to maximize sensing reliability. First, PDMS thickness must be counterbalanced by the
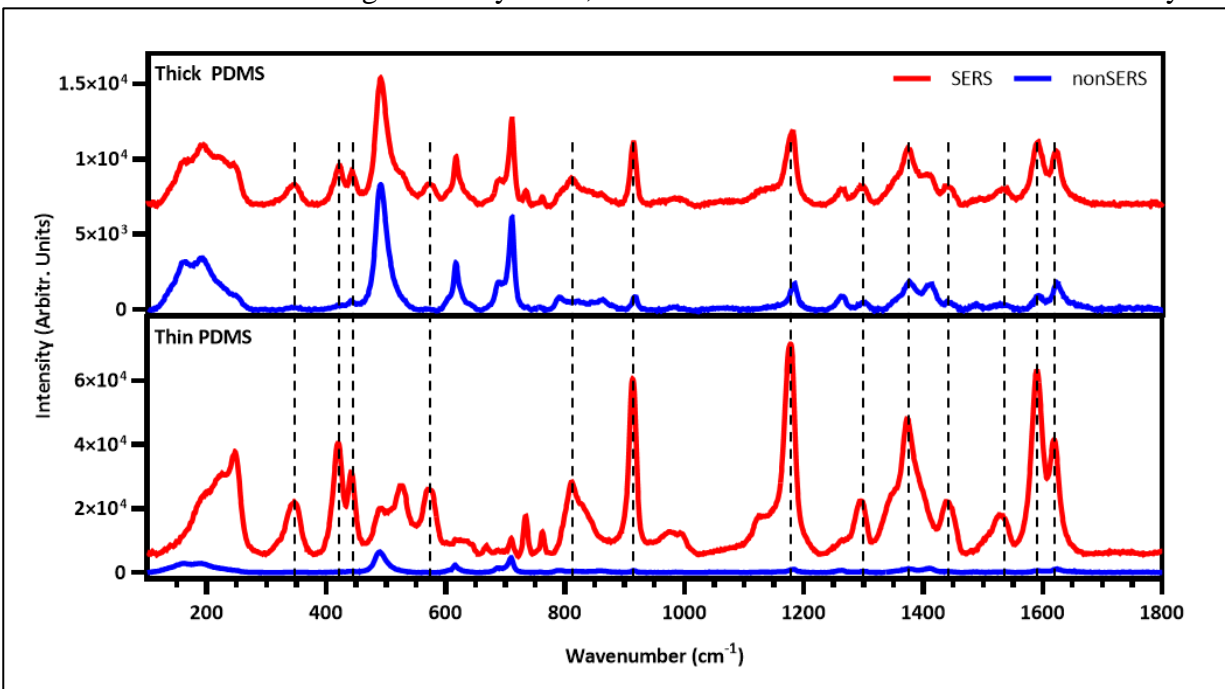
Figure III.2: SERS (blue) and non-SERS (grey) Raman spectra of crystal violet through (a) thick and (b) thin PDMS, demonstrating the ability to perform SERS spectroscopy through a PDMS wall, as well as the importance of PDMS thickness on the magnitude of enhancement.

Table III.1: Crystal violet Raman peaks used to compare surface enhancement through thick vs. thin PDMS.

Raman Band (cm⁻¹)	Thick (~1.0 mm)	Thin (~0.17 mm)
345	2.81	300.17
420	3.63	284.76
441	2.45	74.34
571	2.41	292.79
810	2.17	86.42
915	2.42	111.04
1175	2.47	58.87
1300	1.57	80.21
1374	1.91	43.04
1445	1.55	84.25
1529	1.26	129.17
1592	2.25	116.60
1621	1.95	35.34

channel's ability to withstand fluidic pressure without rupturing. The PDMS cap cannot be made so thin that it ruptures when samples are injected. Second, PDMS thickness must be uniform across the sensor area, as well as from sensor to sensor. Uniform thickness is essential to reliable sensing.

A more detailed understanding of the SERS enhancement to the Raman spectra of crystal violet considers the confocal sensing volume of the spectrometer relative to the volume of crystal violet being influenced by SERS. The volume of crystal violet solution being sensed by the laser was orders of magnitude greater than the volume of crystal violet solution sufficiently close to the sensing surfaces to be influenced by SERS, as discussed in previous work.[127] The volume of crystal violet solution being sensed by the spectrometer can be approximated as a cylinder with a
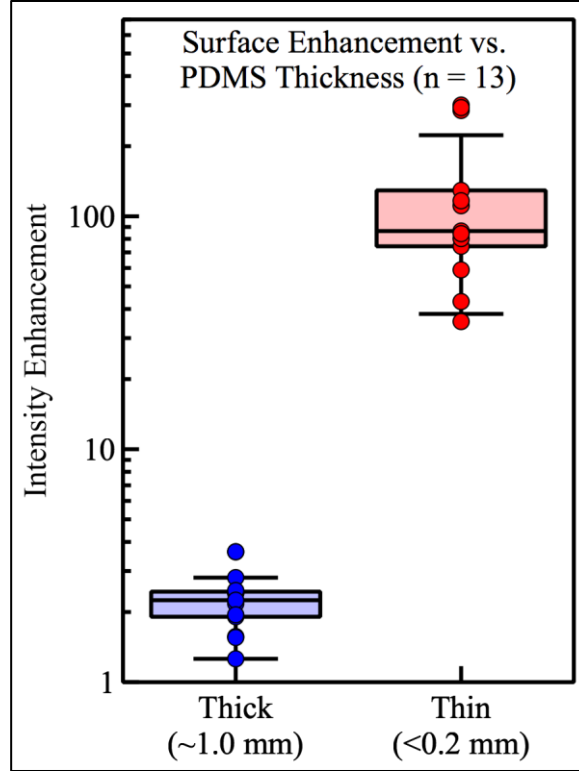
Figure III.3: Comparison of the enhancement to selected crystal violet
Raman peaks through thick and thin PDMS.

diameter equivalent to the laser waist and length equivalent to the confocal range. The beam

waist radius was determined to be approximately $d_w = 12$ μm via the knife-edge method.[127,171]

This was used to calculate the laser's confocal length L_c via **Equation (III.3)**.[127,172] This, in turn,

was used to calculate the ratio of confocal volume to SERS-influenced volume, defined here as

the enhancement factor (*EF*), via **Equation (III.4)**.

$$L_c = \frac{2\pi(d_w)^2}{\dfrac{\lambda}{10^3}} \tag{III.3}$$

$$EF = \frac{E_I}{2\dfrac{L_n}{L_c}\pi D(d_n d_m + d_m^2)} \tag{III.4}$$

In these equations, λ is the 532-nm laser wavelength, E_I is the raw enhancement for each

peak, d_n is the radius of effect for SERS (nm). D and d_n were determined via ImageJ analysis of

SEM images of the nanowires to be 1.96×10^{-4} nm^{-2} and 29 nm, respectively. Because SERS is extremely local to the sensing surface,[173] a radius of effect of $d_m = 3$ nm was used.[174] EF was estimated to be an average of 9.9×10^4 for crystal violet spectra acquired through thick PDMS and an average of 5.8×10^6 for spectra acquired through thin PDMS. The enhancement factors and vibrational modes for each chosen Raman band of crystal violet,[175–182] as well as the vibrational modes for the Raman bands of PDMS[183–187] can be found in

    Table B.1.

Surface-Enhanced Raman Spectroscopy of Melamine through PDMS Substrates

    After demonstrating the viability of SERS through thin PDMS with crystal violet, SERS spectra were acquired of melamine solutions in DI Water using SERS substrates fabricated on ~0.15-mm thick PDMS substrates. Two substrates, hereafter named P1 and P2, were fastened

Raman Band (cm-1)	Vibrational Modes	Reference
160	γas(C–Si–C)	186,187
188	δ(C–Si–C)/δ(C–Si–O)/γs(C–Si–C)/ρ(C–Si–C)/σ(C–Si–C)	183,186,187
488	νs(Si–O–Si)	183–187
615	ν(Si–O–Si)/ν(Si–C)	186
646	ρas(Si–C3)	184
687	ν(Si–C)/ρ(C–H3)	183,186,187
708	ν-s(Si–C)/δ(C–H3)	184–186
754	ρ(C–H3)/ρs(Si–C3)/ν(Si–C)	183,184,186
787	ρas(C–Si–C)/νas(C–Si–C)/ρ(C–H3)	184–187
845	ρas(C–Si–C)	184
859	ρ(C–Si–C)/ρ(C–H3)	184–187
882	ρas(Si–C3)/ρas(C–Si–C)	184
1088	νas(Si–O–Si)	184
1262	δs(C–H3)/δ(C–H2)	184–187
1411	δas(C–H3)/δ(C–H2)/σ(C–H2)	183–187

upside down to a reservoir so that Raman spectra were acquired through the PDMS substrate.

Raman spectra were acquired of μM concentrations of melamine in DI water (1, 2, 3, 4, and 6 μM for P1; 2, 4, 6, 8, 10, and 12 μM for P2). While the characteristic peak of melamine at 691
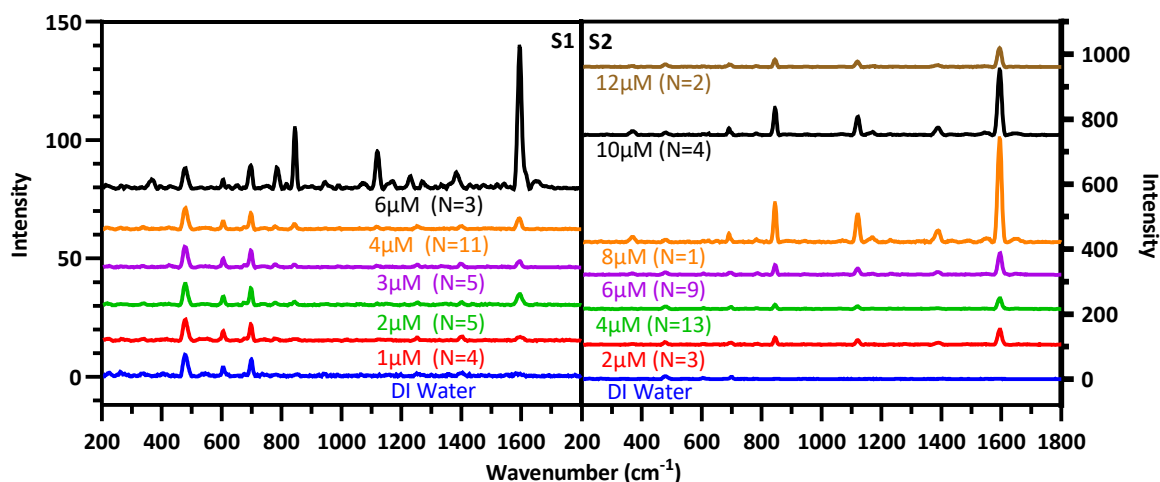
Figure III.4: SERS spectra of melamine in DI Water, acquired through P1 on the left and P2 on the right. Number of spectra acquired for each concentration through each substrate in parentheses.

cm^{-1} is coincident with the PDMS peak at 703 cm^{-1} associated with Si-C symmetric stretching and CH$_3$ bending, multiple melamine peaks are visible even at concentrations of 1 and 2 μM for both substrates. 6 melamine peaks other than the 691 cm^{-1} peak were identified in the spectra plotted in **Figure III.4** that could be assigned vibrational modes, as tabulated in **Table B.2**.[109,188] Importantly, the lowest concentrations detected are well below the 7.93 μM limit set by the Codex Alimentarius, demonstrating the efficacy of SERS sensing of melamine through PDMS.

SERS spectra exhibited substrate-to-substrate variation, with spectra from P2 generally having much greater melamine signal than P1, as illustrated by direct comparisons of the signals generated by 2, 4, and 6 μM concentrations of melamine shown in **Figure III.4**. Additionally, signal intensity exhibited point-to-point variability, with some spots on both substrates generating much more melamine signal than other spots. This effect is likely due to variation in nanowire density caused by the hydrophobicity of PDMS inhibiting precursor flow around the ZnO seed during hydrothermal nanowire growth. This variability in nanowire growth would cause variability in effective surface area. The ratios of melamine peak intensity to PDMS peak

intensity at 488 cm^{-1} shown in **Figure B.10** were averaged for each melamine peak across all concentrations measured for each substrate. For both substrates, these melamine to PDMS peak ratios followed the same trends with increasing concentration. Furthermore, the ratio of the 1596 to 845 cm^{-1} melamine peaks, shown in **Figure B.11**, remained consistent between substrates and across melamine concentrations, lending confidence that SERS can be used to reliably and consistently sense melamine through PDMS once device nanowire fabrication is standardized. In addition to variation across substrates, Raman spectra acquired at the same location on a single substrate exhibited varied intensity from measurement to measurement. It was observed that a Raman spectrum taken immediately after the introduction of a melamine solutions would exhibit little-to-no melamine signal. However, after the substrate was manually disturbed, strong melamine signal would appear in subsequent Raman spectra. This phenomenon is likely due to the hydrophobicity of nanowire beds preventing infiltration of the melamine solution. Disturbing the substrates allows melamine solution to infiltrate the bed of nanowires, enabling much stronger melamine signal. However, this infiltration was inconsistent.

Microchannel Mold Design and Fabrication

Based on the comparison between surface enhancement through thick and thin PDMS, it became apparent that a thin microchannel wall would be vital for successful SERS detection of trace analytes. Thus, it was necessary to design a microchannel mold that would enable the fabrication of channels able to facilitate such sensitive SERS. The mold was designed with a base and lid as shown in **Figure III.5**, which would be fitted onto the base after PDMS was poured into the mold. The mold was designed such that channels fabricated would be z-shaped channels with a 2-mm width in the center portion to facilitate subsequent nanostructure
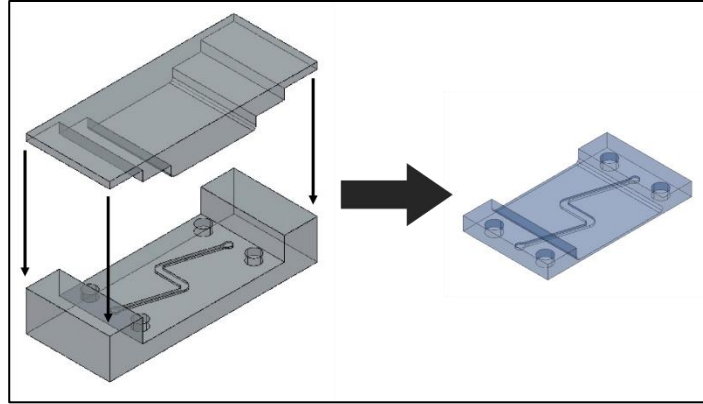
Figure III.5: AutoCAD drawing of the microchannel mold designed to enable sensitive SERS through the top channel wall, along with the resultant microchannel.

fabrication. The channel's top wall was designed to be thick enough at the inlet and outlet to support tubing, but thin enough at 0.10 mm to enable sensitive SERS sensing with minimal PDMS interference. The channel's top wall was also designed such that the thicker portions would be far enough apart to allow high-magnification objectives with short working distances close enough to focus on the SERS-active surface. The channel was designed with the z-shaped structure, ~7 mm long at the center, to enable Raman spectra to be acquired at multiple points along the center portion. The mold was milled from aluminum in the machine shop of the Physics Department at Vanderbilt University. As a function of the milling process, very small ridging occurred on the surface of the mold lid, which could interfere with SERS sensing through the top wall. To combat this, a glass slide was cut to fit the center portion of the lid and affixed with Kapton tape to the mold lid. Glass spacers were also cut and similarly affixed to the ends of the lid, which would rest on the base, in order to maintain the designed thickness of the PDMS cap.

Fabricating SERS Substrates Inside PDMS Channels

Several channels were sputtered with a ZnO seed layer and grown with nanowires. PL spectra of the nanowires inside the channels, shown in **Figure B.12**, exhibited a large band-edge emission and minimal visible emission, indicating high crystallinity with few defects. The intensity of the band-edge emission varied from channel to channel as shown in **Figure B.12**, which indicates variability in the amount of ZnO present in the channels. As exhibited by **Figure B.13**, nanowire density and dimensions varied greatly from channel to channels. Nanowire formation was, in general, sparser for sputtered seed layers versus e-beam deposited seed layers, as exemplified by a comparison of nanowire density between **Figure B.5** and **Figure B.13**. This variability demonstrates that sputtered ZnO does not result in uniform nanowire growth, indicating that another means of combating PDMS hydrophobicity should be explored. One possible way to do so would be to make channels with a copolymer consisting of PDMS and poly(ethylene oxide) (PEO), which has been shown to improve hydrophilicity.[189] Making the channels hydrophilic should improve precursor flow at an e-beam deposited ZnO seed layer, which would make nanowire growth and density more uniform. Channel 4 in **Figure B.13** exhibited the most consistent nanowire growth, and was selected for further development. SEM
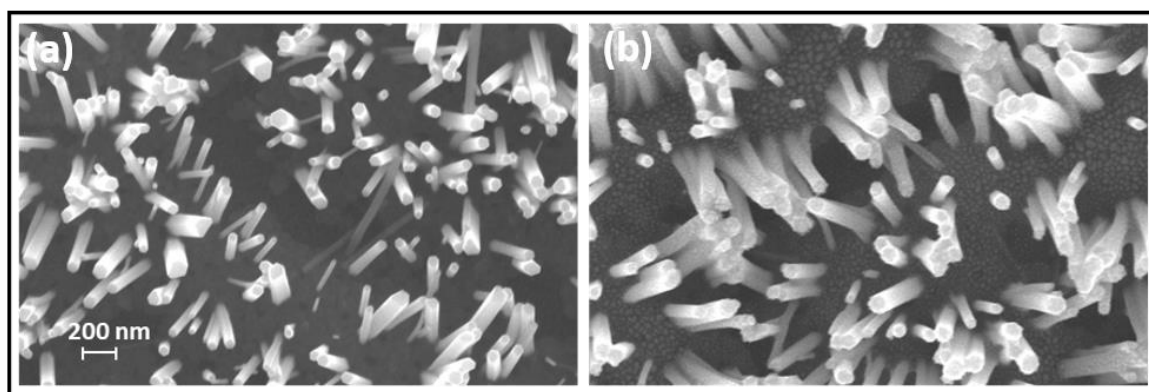
Figure III.6: SEM images of ZnO nanowires (a) before and (b) after deposition and anneal of Ag, demonstrating nanowire growth and Ag nanoparticle formation.

image of the channel taken before (**Figure III.6(a)**) and after Ag deposition (**Figure III.6(b)**)

confirmed the growth of highly crystalline nanowires inside the channel. The UV-Vis spectrum

of the Ag/ZnO nanowires in the channel (**Figure III.7**) exhibited a clear plasmon peak at ~515

nm and shoulder at ~600 nm. This is likely because of the dual size populations of Ag

nanoparticles deposited on the nanowire sides and the floor of the channel, as is exhibited by

SEM of the Ag/ZnO nanowires in **Figure III.6(b)**. The plasmon emission peaked at ~515 nm,

close to the 532 nm laser line, and extended well past the end of the fingerprint region at ~590

nm, making the channel suitable for SERS. Subsequently, the channel was completed by binding

the PDMS to a glass slide and tubing was inserted at the inlet and outlet.

Surface-Enhanced Raman Spectroscopy of Crystal Violet in Channel

   Crystal violet was used to characterize a SERS detection in the completed channels, since

crystal violet has multiple strong peaks between 900 and 1200 cm^{-1}, where the Raman of PDMS
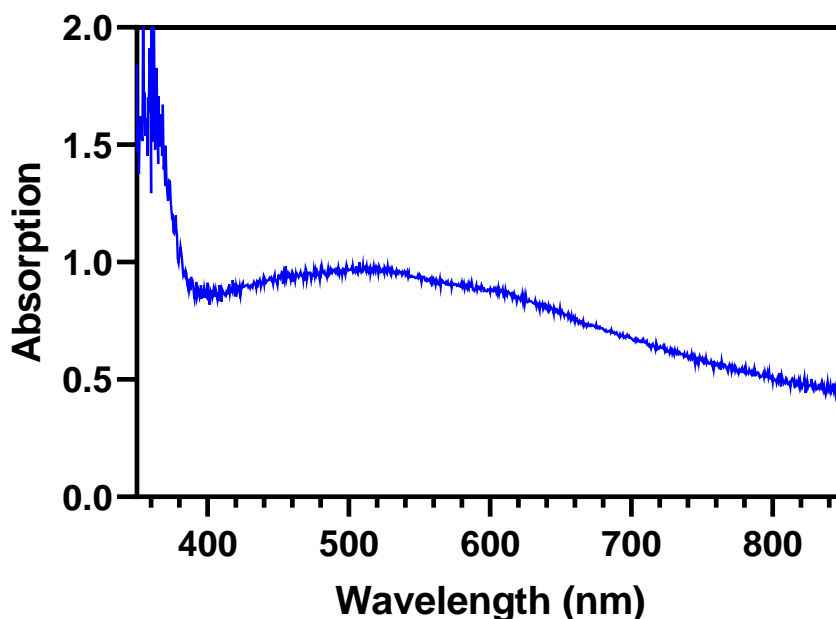
Figure III.7: UV-Vis spectrum of ZnO nanowires decorated with Ag
nanoparticels after anneal

is relatively weak. Raman spectra were acquired of 10 crystal violet solutions in DI water
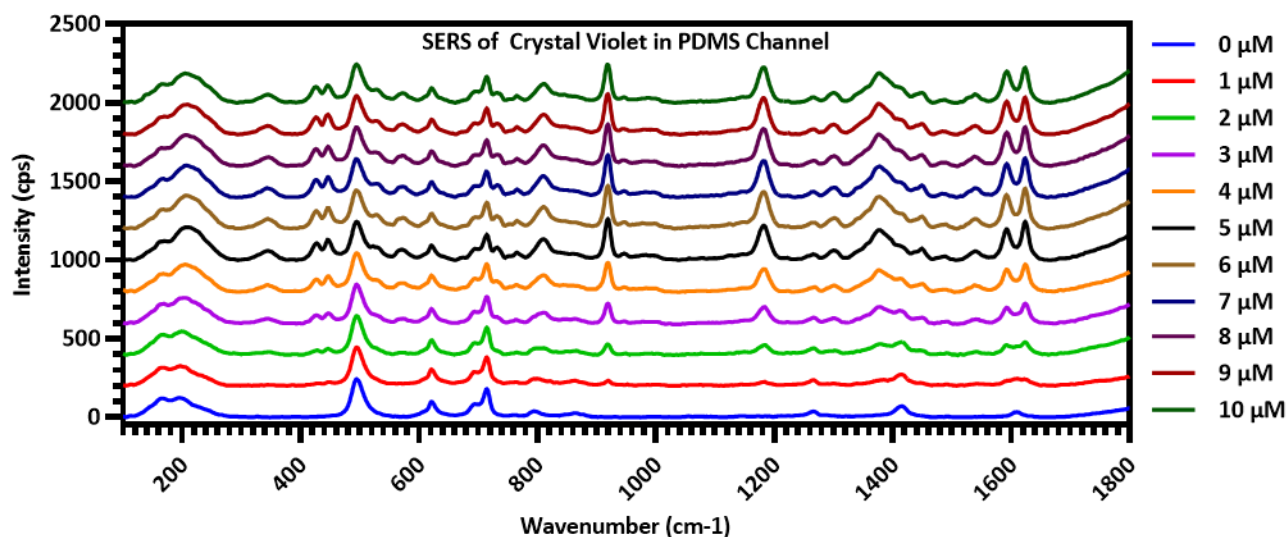
Figure III.8: Raman spectra of crystal violet solutions taken inside a fabricated channel, in concentrations ranging from 1 to 10 μM with a DI water control.

ranging from 1 μM to 10 μM concentrations in 1-μM increments, with a DI-water control

(**Figure III.8**). Before each solution was syringed through the channel, it was flushed with DI

water, and the Raman spectra were all acquired at the same location along the channel. There are

two strong crystal violet peaks in particular that are not near any PDMS peaks: the C-C_{center}-C

bending peak at 917 cm^{-1} and the C-C_{center}-C asymmetric stretching peak at 1175 cm^{-1}. These

peaks were not present in the control spectrum with no crystal violet, but clearly visible at a 1-

μM concentration. These crystal violet peaks exhibited a steady increase in intensity through the

5-μM concentration, as illustrated in **Figure III.9**. From 6 – 10 μM, however, the peak intensity

reached an asymptotic maximum. Raman spectra taken of the sensing surface after crystal violet

solutions were flushed from the channel with DI water exhibited crystal violet peaks, meaning

the levelling off of the Raman signal was likely due to accumulation of crystal violet adsorbed on

the sensing surface.

CONCLUSIONS
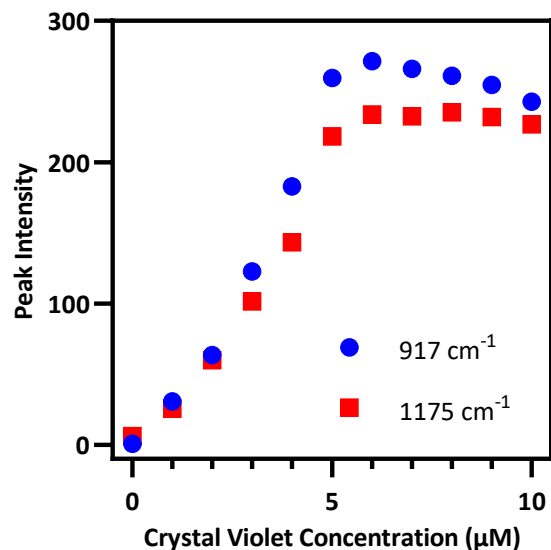
Figure III.9: Intensity of two crystal violet peaks as a function of increasing crystal violet concentration.

This work demonstrated a facile technique to fabricate physically deposited Ag nanoparticle decorated ZnO nanowires inside fluidic channels, allowing microfluidic SERS sensing to benefit from dense Ag nanoparticle formation from e-beam deposition. Through careful design and fabrication of fluidic channels to minimize spectral interference from PDMS, μM concentrations of crystal violet and melamine were detected, demonstrating the ability of the fluidic device to detect relevant concentrations of melamine. By further improvement on the SERS-active substrate fabrication process, it is expected that this process can provide a reliable and sensitive detection of melamine in a SERS-active microfluidic devices.

CHAPTER IV

TOXIC METALS CHELATION BY 18-CROWN-6 ETHERS IN MULTIPLE SOLUTIONS
AND QUANTIFICATION BY SPECTROSCOPIC TECHNIQUES

Reprinted with permission from:

ABSTRACT

Toxic metals exposure is a significant problem for military personnel, with increasingly
prevalent embedded fragments due to improvised explosive devices. Current biomonitoring for
military personnel with embedded fragments is centralized, limiting capacity and availability.
Importantly, monitoring using this approach begins long after peak exposure, indicating a need
for portable, multiplexed toxic metals detection that can be carried out closer to the time of
exposure with increased frequency. Small molecule chelators such as crown ethers are known to
selectively bind metal cations in solution. Crown ethers possess selective chelation of multiple
metal ions and is dependent on molecular structure, solution properties, and other parameters.
This selectivity extends to multiple ions and depends on not only molecular structure, but also
the solution properties. The goal of this study is to assess the potential for metal sensing in
solution as a function of crown ether structure and solution properties with future use for toxic
metal sensing from embedded fragments as a potential translational objective.

INTRODUCTION

As of 2017, improvised explosive devices (IEDs) have accounted for almost 75% of all traumatic injuries to U.S. soldiers in recent conflicts in Iraq and Afghanistan.[29] This means that of the more than 50,000 military personnel wounded in action so far in those conflicts,[191] almost 40,000 of them could have toxic embedded fragments[30] In response to this growing need, the United States Department of Veterans Affairs (VA) established the Toxic Embedded Fragment Surveillance Center (TEFSC, Baltimore, MD) in 2008 with the overall mission to 1) identify veterans who may have embedded metal fragments, and 2) conduct long-term medical surveillance of this population,[12] The evaluation process for inclusion into the Embedded Fragments Registry (EFR) is predicated on the individual's knowledge or suspicion of retained fragments,[31] Thus, biomonitoring of toxic embedded fragments begins long after peak exposure and depends on incomplete knowledge concerning exposure and retention toxic fragments from IEDs, making inclusion into the EFR noncomprehensive. As a result, there are currently only around 16,000 veterans enrolled in the EFR,[192] Biomonitoring of these veterans is carried out via centralized urinalysis using inductively-coupled plasma mass spectrometry (ICP-MS).[9,12,29] While ICP-MS is sensitive and precise, it is a large, research-grade instrument that requires significant power and highly trained technicians for operation,[35,36] making it unsuitable for use near locations where military blast injuries occur. Furthermore, there is a lack of information concerning the scope and extent of embedded fragments[17,37] as well as their long-term health effects.[6,30] To ensure more comprehensive and complete biomonitoring of embedded fragments, a portable, multiplexed toxic metals sensing strategy is required.

There are many techniques for toxic metals detection that can be implemented in a portable setting, including spectroscopic techniques such as fluorescence, colorimetry, and Raman spectroscopy. Many strategies utilizing these techniques make use of small-molecule

73

chelators known to bind various metal ions in solutions. One common family of chelators are known as crown ethers, small molecules with a characteristic ring made up of carbons and oxygens which are best known for chelating alkali metal cations.[90] While these chelators are moderately selective, they still bind multiple different ions in solution. Small changes in crown ether structure can significantly affect which metals it will bind.[91,93] Additionally, differences in solution affect crown ether morphology, changing chelation selectivity.[193] The purpose of this study is to explore how changes in the structure and solution of 18-crown-6 (18C6) ethers can change its selectivity profile for metal ions.

<div align="center">EXPERIMENTAL</div>

Two different solvents consisting of dimethyl sulfoxide (DMSO) and deionized (DI) water were used for all experiments in this study: 1:1 DMSO/water and 1:3 DMSO/water. 4'-aminobenzo-18-Crown-6 (AB18C6) and benzo-18-Crown-6 (B18C6) and the following 22 metals were examined as a part of this study: Al^{3+}, Ag^+, As^{3+}, Ba^{2+}, Ca^{2+}, Cd^{2+}, Co^{2+}, Cr^{3+}, Cu^{2+}, Fe^{3+}, Hg^{2+}, K^+, Li^+, Mg^{2+}, Mn^{2+}, Mo^{5+}, Na^+, Ni^{2+}, Pb^{2+}, UO_2^{2+}, W^{4+}, and Zn^{2+}. All metal salts used to obtain these ions were purchased from Sigma Aldrich. All 14 metals in the TEFSC biomonitoring panel[12,30] are included, as well as metals commonly found in urine, such as Ca^{2+}, K^+, Mg^{2+} and Na^+. Also included are a number of common metals that could make their way into human urine, such as Al^{3+}, Mn^{2+}, and Zn^{2+}. 100 μM equimolar solutions of each metal individually with AB18C6 were formed in both 1:1 DMSO/water and 1:3 DMSO/water.

In this study, the chelation of metal ions by two crown ethers was studied in a single solution to explore how a small change in the crown ether's structure might change the crown ether's metal selectivity. Furthermore, chelation by chelation of metal ions by one of those crown

<div align="center">74</div>

ethers was examined in two solutions. Chelation of metals by AB18C6 and B18C6 was examined primarily using ultraviolet-visible extinction spectrophotometry. Preliminary examination of the extinction spectrum of using a quartz cuvette in a Varian Cary 50 Bio spectrophotometer. These measurements were acquired at a resolution of 5 nm over a range of 250 – 800 nm to confirm the absorption profile of AB18C6 reported by Sarfo *et. al.*,[91] and to explore differences in chelation of metal ions between AB18C6 and B18C6. For these experiments, the extinctions from 100-µM concentrations of each crown ether in 1:3 DMSO:water were measured without metals. Subsequently, the extinctions of 100-µM equimolar concentrations of each crown ether and selected metal salts in 1:3 DMSO:water were acquired.

Full UV-vis spectrophotometry chelation sweeps of metal ions by AB18C6 were performed using Thermo Scientific™ Nunc™ UV-transparent plastic 96-well plates in a Tecan Infinite M1000 Pro plate reader. These measurements were acquired at a resolution of 1 nm over a range of 250 – 400 nm to determine which metals are chelated by AB18C6. For these measurements, 100-µM concentrations of AB18C6 in both solvents were used without metals, and 100-µM equimolar solutions of AB18C6 and each metal salt in each solvent were used for selectivity assessments. The same instrument was used to acquire fluorescence measurements of AB18C6 in the presence and absence of selected metals were acquired with an excitation wavelength of 295 nm over a range of 300 – 700 nm at a resolution of 2 nm. The same crown ether and metal solution strategy was used for fluorescent measurements, except only two metals known to be chelated from previous experiments were included. UV-vis spectrophotometry with the same spectral parameters described above was performed on 100-µM crown ether solutions with one of the metals known to be chelated in concentrations of 1 nM, 10 nM, 100 nM, 1 µM, 10 µM, and 100 µM. Fluorescence spectroscopy was performed on these same solutions with an
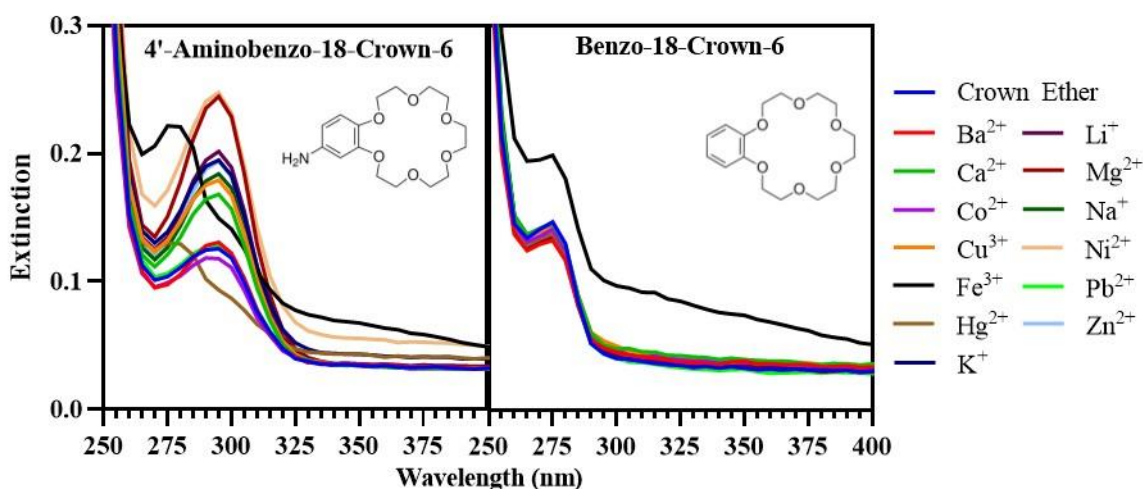
Figure IV.1: UV-Vis extinction spectra of 100-μM AB18C6 and B18C6 in 1:3 DMSO:water without and with equimolar concentrations of selected metals.

excitation wavelength of 295 nm over an emission range of 304 – 500 nm at a resolution of 1 nm.

RESULTS & DISCUSSION

The first experiment was a comparison via UV-vis spectrophotometry of which metals are chelated by AB18C6 and B18C6. It was reported by Sarfo *et. al.*[91] that AB18C6 crown ethers possess a strong extinction peak centered at 295 nm. When the crown ether chelates a metal, this peak is quenched and another emerges at ~280 nm. For this experiment, 100-μM solutions of AB18C6 and B18C6 by themselves and with equimolar concentrations of 13 selected metal salts prepared in 1:3 DMSO:water. As can be seen in **Figure IV.1**, while AB18C6 has an extinction peak at 295 nm as Sarfo et. al. reported, B18C6 has a peak at ~275 nm. No chelation occurred for most of the metals investigated, as evidenced by a lack of quenching of the 295-nm peak for AB18C6 or the 275-nm peak for B18C6, as well as a lack of an additional peak. However, both Fe^{3+} and Hg^{2+} ions were chelated strongly by AB18C6, evidenced by the quenching of the 295-
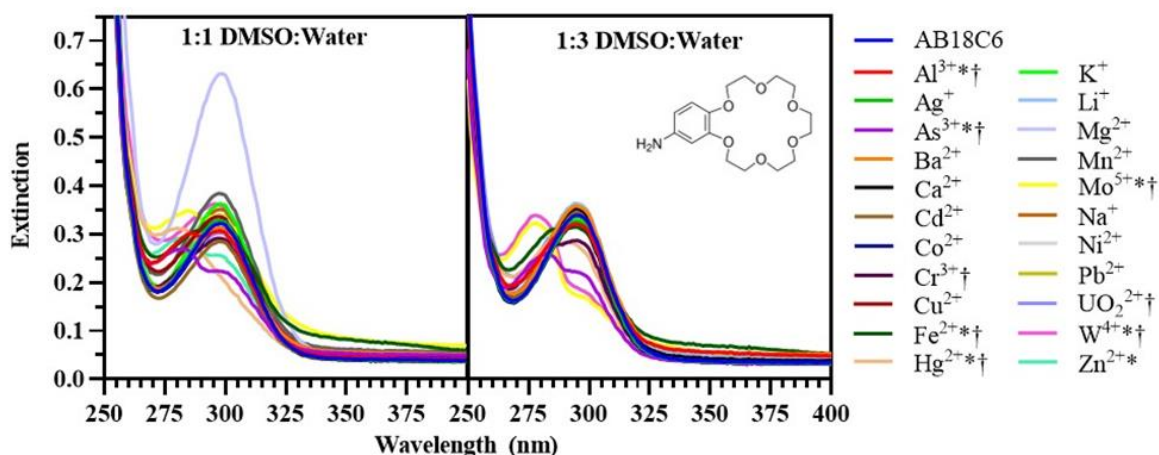
Figure IV.2: UV-Vis extinction spectra of 100-µM AB18C6 alone and with equimolar concentrations of 22 metal salts in two different solutions. Metals chelated by AB18C6 in 1:1 DMSO:water are denoted with "*", while metals chelated by AB18C6 in 1:3 DMSO:water are denoted with "†".

nm peak and appearance of a peak ~282 nm. Benzo-18-Crown-6 chelated none of the metals

examined, indicating that even small differences in crown ether structure can lead to big

differences in metal chelation.

The second experiment performed was an examination of how different solutions would

affect the chelation of metal ions by AB18C6. 100-µM solutions of AB18C6 were prepared in

1:1 DMSO:water and 1:3 DMSO:water, without and with equimolar concentrations of 22 metals.

UV-vis spectra were acquired of each solution and plotted in **Figure IV.2**. While the chelation

profile for AB18C6 was very similar in both solutions, there were some significant differences.

AB18C6 chelated Al, As, Fe, Hg, Mo, and W in both solutions, while it chelated U in only 1:1

DMSO:water and Zn in only 1:3 DMSO:water. Even among metals chelated in both solutions,

there were differences in the strength of chelation. Notably, Al is more strongly chelated in 1:1

DMSO:water while Hg is more strongly chelated in 1:3 DMSO:water. Interestingly, while Sarfo

et. al. reported that AB18C6 chelates Pb^{2+},[91] these experiments demonstrate a lack of Pb^{2+}
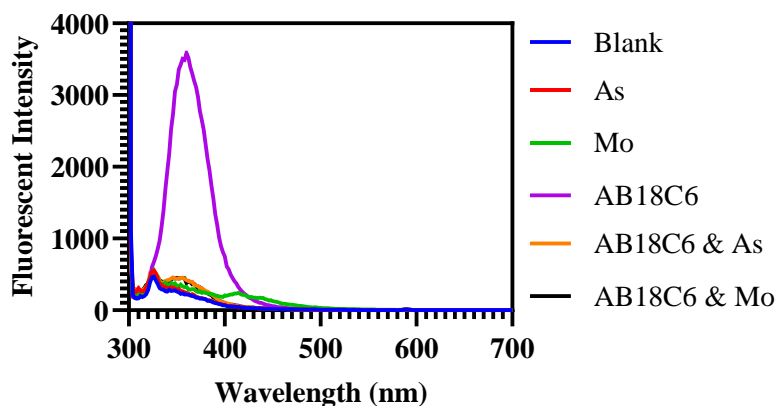
Figure IV.3: Fluorescent Spectra of AB18C6 by itself and with As and Mo separately in 1:3 DMSO:DI Water, demonstrating fluorescent quenching when of the crown ether when chelating both metals.

chelation in either solution. Because of the dependence chelation has on solution, it is likely that this discrepancy with reported results result from an unreported difference in solution.

While UV-vis is excellent for qualitatively determining whether a crown ether is chelating a metal ion, it is difficult to extract any meaningful quantitative information on the amount of chelation taking place in a given solution. However, Sarfo et al. reported that AB18C6 possesses a fluorescence peak at ~370 nm that gets quenched in the presence of chelated metals.[91] To confirm this, fluorescence measurements of 100-µM solutions of AB18C6 without and with equimolar concentrations of As^{3+} and Mo^{5+} (known to be strongly chelated from **Figure IV.2**) in 1:3 DMSO:water were acquired. As can be seen in **Figure IV.3**, AB18C6 with no metal ions present fluoresces as Sarfo et. al. reported. This fluorescence was strongly quenched when As and Mo were present. However, even at equimolar concentrations of metal ions, this fluorescence was not quenched completely, indicating that fluorescence can be used for quantification of toxic metals chelation by AB18C6.

An initial survey of the changes in optical absorbance and fluorescence resulting from AB18C6 chelation of a range of molybdenum concentrations between 1 nM and 100 µM, as

78
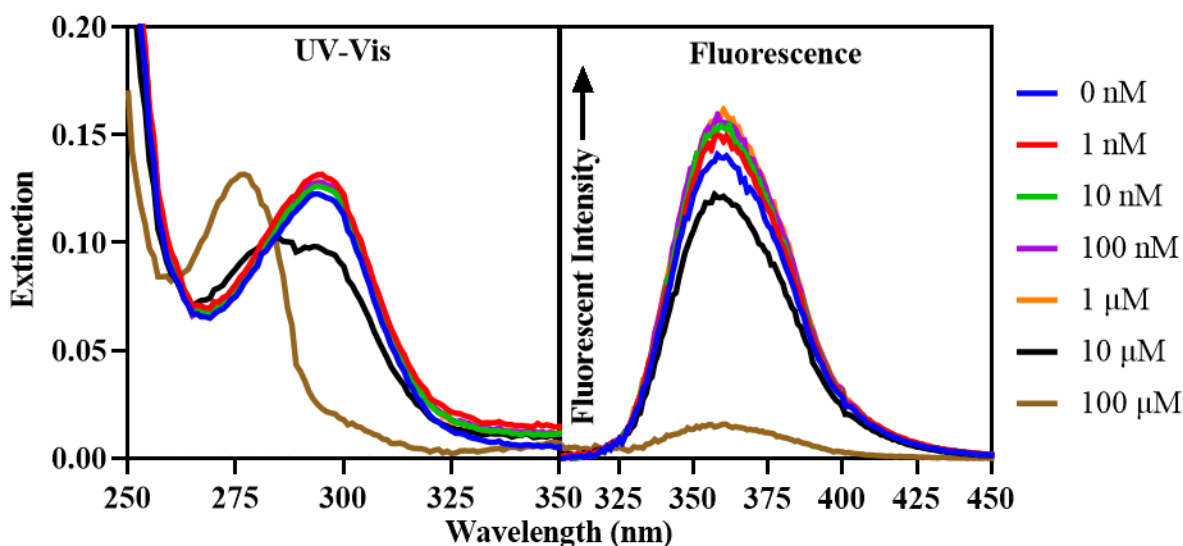
Figure IV.4: UV-Vis and fluorescence spectra of 100-µM AB18C6 with concentrations of Mo between 1 nM and 100 µM, with a control solution of 100-µM AB18C6 unmixed with Mo.

shown in **Figure IV.4**. Mo was selected for this assessment based on the quenching of extinction at 295 nm and the presence of another extinction peak at ~280nm (**Figure IV.2**). Mo concentrations of 1 nM, 10 nM, 100 nM, 1 µM, 10 µM and 100 µM were prepared with 100-µM solutions of AB18C6 in 1:3 DMSO:water. UV-vis spectrophotometry was performed at a resolution of 1 nm over a range of 250 – 400 nm (**Figure IV.4**), and spectra of each concentration of Mo were subtracted from their corresponding spectra of mixed AB18C6 and Mo. Fluorescence used an excitation wavelength of 295 nm over a range of 304 – 450 nm at a resolution of 1 nm. A clear peak shift from ~295 to ~275 nm at 100 µM Mo concentration was evident in addition to a small peak shift at 10 µM. Large fluorescence quenching occurred at 100 µM at ~360 nm with additional, slight quenching at 10 µM Mo concentration. Other concentrations of Mo did not produce evident changes in either UV-vis or fluorescence (**Figure IV.4**).
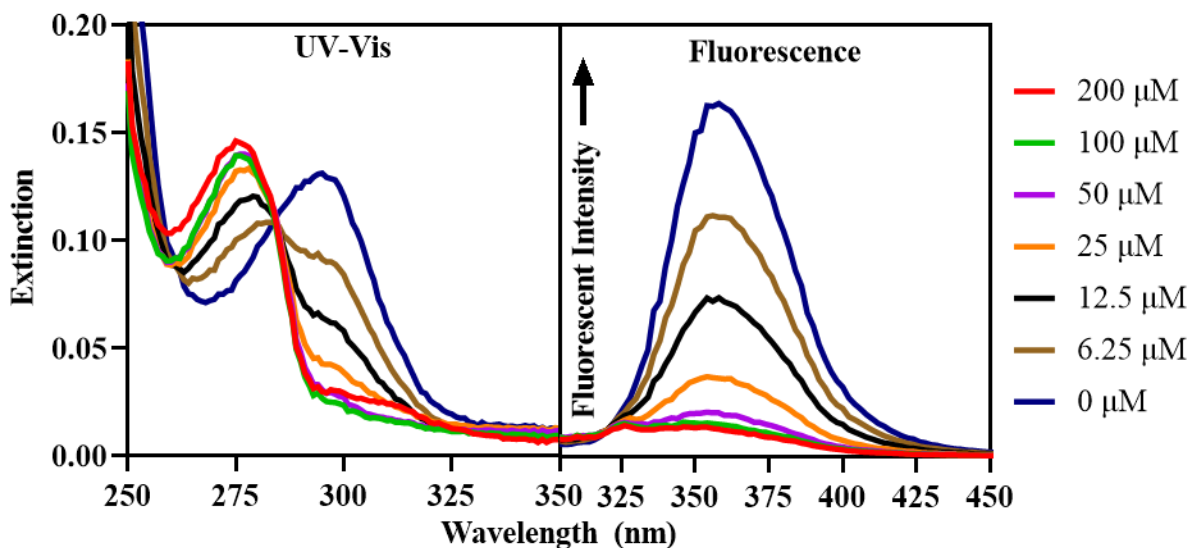
Figure IV.5: UV-Vis and fluorescence spectra of 100-µM AB18C6 with concentrations of Mo between 6.25 and 200 µM, with a control solution of 100-µM AB18C6 unmixed with Mo.

To expand the characterization of Mo chelation by AB18C6, the same experiment was performed using Mo concentrations (in µM) of 6.25, 12.5, 25, 50, 100, and 200. UV-vis spectrophotometry and fluorescence spectroscopy used the same resolution and range, as shown in **Figure IV.5**. The extinction peak at ~295 nm steadily decreased with increasing Mo concentration between 6.25 µM and 50 µM. This decrease reached a minimum at 50 µM and did not continue to decrease for 100 or 200 µM. The extinction peak at ~277 nm increased in conjunction with the decrease of the 295-nm peak, steadily intensifying between 6.25 µM and 50 µM and remaining steady for 100 and 200 µM. Gradual quenching of AB18C6's fluorescence peak at ~360 nm was observed under increasing Mo concentrations, as shown in **Figure IV.5**. Full quenching of this fluorescence peak occurred at the 100 µM concentration of Mo, indicating greater range of chelation quantification for fluorescence than for UV-vis. The absorption decrease at ~295 nm or increase at ~277 nm did not directly correlate with the increase in Mo concentration, suggesting that absorbance may be a complicated indicator of concentration for

this metal. However, these experiments indicate that a quantitative relationship between AB18C6's extinction profile and Mo concentration exists. Furthermore, fluorescence quenching is directly correlated with increasing Mo concentration, that demonstrates the quantitative potential for fluorescent detection of Mo through crown ether chelation.

CONCLUSIONS

This study demonstrated that minor structural changes in 18C6 ethers modulate metal ion chelation with crown ethers. Furthermore, solution characteristics influence crown ether morphology and the strength of metal ion chelations. Crown ether structure and the solvent environment determine metal chelation characteristics. Optimal quantitation of metal ion concentrations will require additional studies of crown ether chelation under various conditions. The quantitative spectroscopic response of single metal ion species with crown ethers, as demonstrated here, can also be expanded to include multi-composition solutions characterized by suitable mathematical analysis. This study demonstrated the potential for UV-vis and fluorescence spectroscopy to quantify chelation of toxic metal ions by crown ethers. These results inform the design of future portable detection and quantification techniques for toxic metal ions in solution.

CHAPTER V

CONCLUSIONS

CHAPTER SUMMARIES & IMPACT

The overall goal of this research was to develop a portable, disposable sensor to detect toxic metal ions in urine via surface-enhanced Raman spectroscopy. This approach required the development of a simple fabrication strategy for integrating physically deposited SERS-active surfaces within fluidic channels prepared via soft lithography. Direct physical deposition of a SERS active surface within a PDMS channel was not publicly disclosed prior to the start of this project. Successful proof of concept also required the optimization of e-beam deposited Ag nanoparticles on ZnO to maximize surface enhancement in Raman spectra acquired with a 532-nm laser. This work was the first to systematically explore multiple fabrication parameters within this paradigm and directly examine the relationships among parameters and surface enhancements to Raman signals.

In Chapter II, Ag nanoparticle fabrication on ZnO via electron beam deposition was optimized for maximally surface enhanced Raman spectroscopy with a 532-nm laser. Four fabrication parameters were explored in this analysis; deposition rate, deposition thickness, anneal temperature, and anneal time. Ag nanoparticles were e-beam deposited onto ZnO at rates of 0.1 and 0.3 Å/s and thicknesses of 1 through 9 nm in 1-nm increments. These depositions were annealed at temperatures ranging from 50 to 400 °C for times ranging from 15 to 150 min. Nanoparticles deposited at 0.1 Å/s generally produced better surface enhancement than those deposited at 0.3 Å/s. Increasing nanoparticle film thickness produced larger and more densely populated nanoparticles, red-shifting and intensifying their plasmon absorption peak.

Nanoparticle film thicknesses between 5 and 9 nm produced good surface enhancement, with 7 nm providing the best enhancement. Annealing at temperatures less than or equal to 200 °C produced the best increase to surface enhancement of the nanoparticles through Ostwald ripening, with annealing at 200 °C for 60 min or 50 °C for 120 min providing the greatest increase in enhancement factor. This work is the first report to systematically explore the impact of fabrication conditions on the performance of a specific SERS sensor, and laid the foundation for the analysis of similar phenomena in other SERS sensing approaches.

Chapter III demonstrated the simple fabrication of SERS-active fluidic channels leveraging the dense nanoparticle formation of e-beam deposited silver. The channel mold was milled from aluminum, and designed to minimize the thickness of the channel top wall. This design was carried out based on a preliminary examination of the effect of light scattering through PDMS on surface enhancement that suggested minimizing PDMS in the optical path would be beneficial to sensing performance. The top wall thickness is, therefore, a compromise between sensing performance and the feasible fabrication of the SERS-active sensor in the channel. The channels were masked and a seed layer of ZnO was sputtered into the channel, on which ZnO nanowires were grown hydrothermally. Ag nanoparticles were then e-beam deposited and annealed according to the parameters identified in Chapter II. Nanowire growth from channel to channel was very inconsistent, presumably due to the ZnO seed applied by sputtering rather than by e-beam deposition. E-beam deposition of ZnO seed is preferred over sputtering due to the apparent growth of more uniform nanowires as demonstrated by previous work[127] compared to the results in Chapter III, but the unidirectionality of e-beam deposition means that only the bottom of the channel would be coated in ZnO, leaving the walls of the channel bare. Because of this, the hydrophobicity of PDMS inhibited intra-channel nanowire

growth, necessitating sputtering of the ZnO seed. Sputter deposition is omnidirectional, coating

all channel walls in ZnO. This is another example of the design and fabrication constraints that

must be overcome (or optimized) for useful SERS sensing from this uncommon substrate.

Raman spectra of crystal violet in DI water were acquired through the PDMS wall on which the

SERS substrate was fabricated. Crystal violet Raman peaks were clearly visible in spectra

acquired at concentrations as low at 1 μM, and spectra acquired of increasing concentrations of

crystal violet exhibited a clear trend of increasing intensity, although saturation occurred at

approximately 5 μM, presumably due to molecular adsorption onto the sensing surface.

Nanowire forests are inherently hydrophobic, so wettability of the sensing surface potentially

compromises detection sensitivity and reliability. However, the reproducibility of spectral

acquisition within the channel suggests that any negative consequences resulting from sensor

hydrophobicity are inconsequential; perhaps the pressure created by injecting solutions into the

channel is sufficient to overcome this hydrophobicity. Following SERS acquisition of crystal

violet solutions in a channel, SERS-active substrates were fabricated on PDMS of the same

thickness as the channel wall and were placed face-down in a reservoir, which was filled to the

point of fluid contact with the sensing surface. Raman spectra were acquired through the PDMS

substrate of micromolar melamine solutions. Multiple substrates exhibited clear melamine signal

at concentrations as low as 1 to 2 μM, which is well below the limit of 7.93 μM melamine in

infant formula, as set by the Codex Alimentarius Commission.[194] Spectral intensity was not

clearly correlated with melamine concentration, and spectral intensity varied among and within

substrates. The variability and lack of correlation with concentration, not observed for crystal

violet sensing by SERS-active surfaces in the PDMS channel, may be associated with

inconsistent nanowire growth and difficulty in wetting inherently hydrophobic beds of

nanowires. The first problem is likely caused by the hydrophobicity of PDMS inhibiting precursor flow around the ZnO seed during hydrothermal nanowire growth. The hydrophobicity of PDMS may be mitigated by fabricating channels from a hydrophilic PDMS-PEO copolymer. This study was an important step in the development of a sensor for detecting toxic metals, demonstrating simple fabrication of channels with densely populated e-beam deposited Ag nanoparticles. Micromolar detection of crystal violet and melamine were successfully performed through PDMS of free molecules in solution. Functionalization of the sensing surface with chelating molecules will further increase detection sensitivity.

In Chapter IV, the chelation of toxic metals in solution by crown ethers was explored in multiple solutions. Equimolar solutions of AB18C6 and B18C6 and 13 different metals were mixed in 1:3 DMSO:DI water. These solutions were examined by UV-Vis spectrophotometry. Chelation of multiple toxic metals ions by AB18C6 was detected by a shift in light absorbance upon as compared to the spectrum of AB18C6 alone. A similar shift was not observed for B18C6 with any of the metals investigated. This result suggests that small changes in crown ether structure, such as the presence or absence of an amine in this case, can greatly affect metal chelation equilibria. Additional studies were carried out with AB18C6, expanding the library of toxic metals investigated to 22. Equimolar solutions of AB18C6 and these 22 metals were mixed in 1:1 DMSO:DI water and 1:3 DMSO:DI water, and were examined by UV-Vis spectrophotometry. Multiple metals were chelated by AB18C6 in both solutions, but there were a few metals chelated in one solution but not the other, and some metals were chelated more strongly in one solution but not the other. These results indicate that solvent can affect crown ether chelation of metal ions, illustrating the need to examine crown ether chelation in fluids indicated by the application, which would be urine in the case of SERS-based urinalysis.

Importantly, this multiplicity of metal ion chelation by a single crown ether is advantageous for multiplexed ion detection. Each ion will affect the crown ether's Raman spectrum differently, which can be elucidated with computational techniques such as principal component analysis (PCA). Multiple crown ethers that chelate different metal ions can be used in conjunction to determine the composition of metal ions in urine, including all 14 metals in the TEFSC biomonitoring panel. As and Mo were selected for further analysis based on strong chelation in 1:3 DMSO:DI water and fluorescence spectra of AB18C6 without and with equimolar solutions of each metal demonstrated fluorescent quenching of the crown ether's fluorescence peak. A 100 μM solution of AB18C6 was mixed with solutions of Mo ranging from 1 nM to 100 μM, and were examined with UV-Vis spectrophotometry and fluorescence spectroscopy. Concentration-correlated quenching of the crown ether's fluorescence peak and shifting of the crown ether's absorption peak was exhibited, with single-digit micromolar concentrations of Mo chelated by 100 μM AB18C6 being distinguishable from the unmixed 100 μM AB18C6 control. These experiments indicate the potential of fluorescence spectroscopy and UV-Vis spectrophotometry to corroborate SERS detection and quantification of toxic metals chelation, and to act as a dual sensing strategy for toxic metals in urine.

SHORTCOMINGS

Significant Aim 1

Only two deposition rates of Ag nanoparticles were explored, which provides an incomplete picture of how deposition rate affects nanoparticle formation, both before and after anneal. The scope of this optimization study was very large, and at the limit of what could

realistically be accomplished in a reasonable time frame. Adding two more deposition rates would have doubled the amount of work, resources, and time required to complete the study. In addition, nanoparticles were deposited on ZnO films rather than on nanowires. As the UV-vis spectrum in **Figure III.7** illustrates, the plasmon absorption peak for nanoparticles deposited on a bed of ZnO nanowires possesses a different profile than the spectra for nanoparticles deposited on a ZnO film, with two populations of nanoparticles exhibiting a plasmon peak at ~515 and shoulder at ~600 nm versus a single plasmon peak between 500 and 600 nm, as expected based on this study. As with increasing the number of deposition rates examined, performing this study on nanowires would have greatly increased the difficulty and time-consumption of the study, making it impossible to complete the study in a reasonable time frame. Thus, while the results from Chapter II are a good foundation for optimizing nanoparticle formation on ZnO nanowires, a more complete study would perform the exploration of nanoparticle fabrication parameters on nanowires rather than a film. Of course, doing so would add effective surface area as a variable that affects SERS enhancement. In addition, while a large population of substrates was available to analyze for deposition parameters, each data point in the annealing parameter space was represented by a single substrate. SERS sensitivity is notoriously difficult to control, being highly responsive to small changes in nanoparticle shape, structure, size, and density. It would have been preferable to have multiple substrates for each intersection of anneal time and temperature, to develop a statistically powerful understanding of how annealing parameters affect surface enhancement. To acquire even 3 substrates at each intersection would have tripled the amount of work and resources required to perform this study, making it infeasible for the scope of this study. While SEM images were acquired of representative substrates before annealing, it would have been advantageous to take SEM images of substrates after annealing to

examine the effects of Ostwald ripening at each intersection of anneal temperature and time. This was attempted, but high-quality images could not be acquired due to significant charging of the samples. Furthermore, atomic force microscopy would have been beneficial for acquiring information on how the height of the nanoparticles was affected by annealing and how height changes affect enhancement. Doing so would have required a significant amount of time and is better-suited for an investigation of a smaller parameter space.

Significant Aim 2

While the work performed in Chapter III represents a significant proof of concept that the strategy of physically fabricating SERS-active substrates within a PDMS channel produced devices capable of sensitively detecting contaminants such as melamine, it is presented with multiple shortcomings that must be acknowledged. To truly minimize interference of PDMS, it would be best to consider not just the thickness of the PDMS wall, but also the strength of the PDMS wall. In Chapter III, the thickness of the PDMS wall was chosen to allow lenses with short-working distances to acquire SERS spectra through the wall, but a better way to choose that thickness would be to optimize wall thickness with the channels' ability to withstand expected fluidic pressure. Doing so would require a clearer understanding of expected fluidic pressure, and would be best accomplished when channel design is more clearly understood. Another significant issue with this work was the inconsistency of nanowire growth in both channels and on PDMS substrates. In both cases, this inconsistency appeared to be caused by the hydrophobicity of PDMS interfering with flow of precursors during hydrothermal nanowire growth. Sputtering of the ZnO seed was used instead of e-beam deposition in channels in an attempt to coat more of PDMS surface inside the channel, but nanowire growth remained

88

inconsistent. A better solution might be to make channels out of a PDMS-PEO copolymer, which has been shown to be more hydrophilic than PDMS by itself. SERS of both crystal violet and melamine should have been performed in multiple channels at each concentration to avoid the problem of adsorption saturation of the sensor, and to enable calculation of a limit of detection. Doing so would have required a large number of channels, and fabrication of SERS active substrates within channels was too inconsistent to develop the required number of channels.

Significant Aim 3

While the work in Chapter IV developed a chelation profile for AB18C6 in multiple DMSO/DI water solutions, it is still unknown how binding the crown ether to the sensing surface would affect chelation equilibria. In order to complete the fabrication of toxic metals sensor, functionalization of the sensing surface within a channel with AB18C6 should have been accomplished and successful SERS of the crown ether with and without metals chelated should have been accomplished. While the results in Appendix C indicate that successful functionalization of SERS-active substrates with AB18C6 did occur, SERS spectra of the crown ether could not be acquired, meaning that surface coverage by the crown ether was likely insufficient to ensure a detectable crown ether SERS signal.

REPRODUCIBILITY & SENSITIVITY

Reproducibility of Surface Enhanced Raman Spectroscopy

Whenever SERS is explored as a detection and quantification technique, the question of reproducibility inevitably arises. As seen in Chapter II, small changes in nanoparticle shape, size,

crystal structure, and interparticle distance within an array of nanoparticles can have a large effect on the plasmon peak of that array, and thereby affecting the sensitivity and reproducibility of SERS measurements. Because SERS sensitivity is highly dependent on the sensing surface area, reproducibility is also dependent on the consistency of nanowire growth. While this work did not explore the reproducibility of detection, calculation of relative standard deviation (RSD) for SERS spectra from similar substrates has been reported. In general, substrates exhibiting RSDs lower than 15% are considered "well-performing."[195] Khan *et. al.* reported an intensity RSD of 3.5% over a mapped area of Au-decorated ZnO nanowires, and less than 10% variation of SERS intensity across batches of Au/ZnO nanowires.[196] Chen *et. al.* reported peak intensities for spectra acquired at 40 spots on a similar Au-decorated ZnO nanowire substrate,[197] from which Grégory Barbillon calculated an RSD of <15%.[138]

Sensitivity of Surface Enhanced Raman Spectroscopy

There are a wide variety of metals on the TEFSC biomonitoring panel, with a large range of relevant concentrations. These range from as low as ~170 pM for uranium to as high as ~16 μM for zinc.[29] This means that a multiplexed detection device designed to detect all 14 metals will require a range of detection of at least 6 orders of magnitude to properly identify concentrations of ions in excess of expected values for healthy individuals. The device presented in this work enabled detection of untargeted analytes in concentrations as low as 1 μM, so work remains to be done to improve sensitivity to required levels. However, Sarfo *et. al.* calculated a limit of detection of 6.90 pM for their Au-decorated ZnO nanowire substrate functionalized with AB18C6,[91] which is well below the nM sensitivity of portable electrochemical techniques[198] or the μM sensitivity of portable X-ray fluorescence techniques.[199] Achieving this level of

sensitivity through PDMS is complicated by the effect of PDMS hydrophobicity on sensor fabrication. Additionally, the spectral contributions from PDMS complicates sensing of low-intensity signals. For sufficiently large channels to enable facile alignment and assembly, it may be advantageous to form the SERS sensor on the glass portion of the device. In this way, the effects of PDMS on both nanowire growth and sensor sensitivity could be minimized. If channels are made small enough that an alignment step is problematic, other steps can be taken to both regulate nanowire growth and maximize sensitivity through PDMS. Channels can be fabricated out of a PDMS-PEO copolymer as discussed above to make the channels more hydrophilic, and the PDMS cap thickness can be minimized to reduce polymeric light scattering.

FEASIBILITY

Device Reliability

There is no reason to expect that the Ag-decorated ZnO nanowire surfaces reported in this work cannot achieve similar reproducibility to that reported by Khan *et. al.*,[196] especially if nanoparticle fabrication parameters are tightly controlled and nanowire growth is stabilized. Comparing these values to RSDs calculated for ICP-MS determination of toxic metals in urine, which range from <1% to 4%[200,201] demonstrates that SERS sacrifices precision for the sake of portability and ease of use. Batch-to-batch variability in intensity can be mitigated by the incorporation of a reporter molecule control by which signal intensity can be normalized across batches. Signal variation across a single surface can certainly be mitigated by averaging spectra acquired from multiple points on a SERS surface. A signal intensity RSD of <5% across a single

device is certainly acceptable error for a portable sensor, in line with RSDs reported for portable electrochemical[198] and X-ray fluorescence sensors.[202]

The reproducibility of crown ether chelation is a concern. As demonstrated in Chapter IV, crown ether chelation depends on sample composition, including the presence of nontarget ions. **Figure IV.2** demonstrates that the concentration DMSO in the solvent affected the strength of chelation between crown ethers and certain target ions, and other studies have demonstrated that fluid properties such as pH can affect the strength of crown ether chelation.[203,204] The relevant fluid properties should be identified, but once they are controlled for, they should not represent a significant hurdle with regard to device reproducibility. A second concern is the effect of competing ions on the identification and quantification of target ions. Because crown ethers are non-specific, the presence of non-target ions or multiple target ions can affect chelation efficiency. This interference will likely necessitate the development of a classification algorithm, such as the artificial neural network developed by Serrano *et. al.* for voltametric identification of metals chelated by crown ethers.[205] While there remain significant hurdles for improving the reliability of the device described in this work, it is reasonable to expect that by fine-tuning the fabrication process and developing a classification algorithm, reliability can be brought in-line with other portable techniques available, bringing to bear the advantages of SERS.

Detector Sensitivity

The limit of detection reported by Sarfo *et. al.* of 6.90 pM for crown ether-functionalized, Au-decorated ZnO nanowires is sufficient to detect even the low levels of uranium. This limit of detection was not determined for a SERS sensor integrated into a microfluidic, which represents

a potential loss of sensitivity. Mao *et. al.* reported a 4× reduction in sensitivity due to sensing

through a PDMS cap versus an open SERS sensor.[165] However, they did not attempt to design

their microfluidic channel to minimize PDMS interference. As discussed in Chapter III, reducing

the thickness of the PDMS cap from 1 mm to less than 0.2 mm resulted in an increase of 10^2 in

surface enhancement. Given that Ag results in more sensitive SERS than Au[206] and the

minimization of PDMS interference accomplished here, pM detection sensitivity is feasible for

Ag-decorated ZnO nanowires functionalized with crown ethers.

CONTRIBUTION & FUTURE WORK

Device Design

There are several potential techniques that can be and have been implemented for

portable toxic metals detection, yet SERS remains the most promising, blending enhanced

sensitivity with ease of use and the potential for multiplexation. Of course, reproducibility of

SERS detection remains a concern. However, as discussed above, controlling substrate

fabrication and the development of a classification algorithm can bring reliability in line with

other portable sensing techniques.[197,205] Other SERS-based designs for toxic metals sensing focus

on detecting single metals.[207–212] Any multiplexation reported is incidental rather than

intentional, being based on other metal ions reporter molecules happen to capture. This work is

the first to propose a SERS-based strategy to tailor multiplexation for the 14 metals listed in the

TEFSC biomonitoring panel.

While some toxic metal SERS detection strategies leverage changes in reporter molecule

spectral fingerprint in response to the presence of target ions,[71,91,93] the most common SERS-

based strategies for toxic metals detection rely the presence of target metal species increasing or decreasing[213] SERS intensity. Such techniques are difficult to multiplex and identification of metal species relies on high selectivity for target metal ions by reporter molecules, since intensity changes are the only indicator of target ion presence. In contrast, the strategy discussed here leverages the non-specificity of crown ethers, being able to identify metal species not by how that change spectral intensity, but rather how they change the crown ethers' spectral fingerprint. This work proposes the selection of crown ethers such that each metal on the biomonitoring panel is captured by at least one crown ether. Of course, this strategy comes with its own challenges. Sensing via spectral changes is more complex than simplified detection via spectral increase/decrease, requiring detailed understanding of crown ether SERS fingerprints before chelation and analysis of spectral changes after chelation. For single metal species in simple solutions, such analysis can be performed by examination of examination of spectral shifts and introduction of SERS peaks as a result of chelation. For multiple metal species in complex solutions, this s best pursued usingi machine learning techniques to develop an algorithm capable of identifying spectral changes resultant from the chelation of specific metal ions and accounting for factors such as competing chelation of multiple ions and changing chelation strength due to urine characteristics such as pH.

This sensing strategy requires spectra acquired from multiple points on each SERS array for sufficiently robust quantification of metal ions. Because multiplexed sensing of 14 metals will likely require multiple SERS sensing sites functionalized with a single crown ether each, the question of site-to-site variability is a potential concern. However, batch fabrication of all sensing sites within a device will mitigate this concern, as there is no reason to expect site-to-site structural variability will differ from variability within each site. Because this sensing strategy

will require multiple crown ethers, it is possible that crown ether density will vary from site to site. This can be controlled for by acquiring SERS spectra of each site before sample introduction. Fabricating the SERS substrate on PDMS simplifies device fabrication, but as discussed above, reduces detection sensitivity due to scattering. If this reduction in sensitivity proves to be problematic, the sensing surface can be fabricated on quartz, which interferes much less with SERS than PDMS. Another potential interferant is the ZnO nanowires used to increase SERS-active surface area. While ZnO nanowires have multiple benefits for SERS as discussed in my previous work[127] and in Chapter III, Zn^{2+} is one of the metals in the TEFSC biomonitoring panel. This is a significant concern if ZnO nanowires shed Zn^{2+}. If that is the case, it may become necessary to switch to silicon nanowires as a substrate, despite the fact that Si absorbs more light in the visible and NIR than ZnO. One of the difficulties inherent to working with microfluidics is that laminar flow inhibits capture of dilute analytes through a lack of mixing. The best way to mitigate this issue would be to increase the channel's cross-sectional aspect ratio, "flattening out" the channel. This would put more of the sample in contact with the SERS surface, increasing the opportunity for capture of metal species.

An important consideration in the development of a reliable portable detector is the detector's stability. One potential concern is the effect of suboptimal storage temperatures on device performance. In Chapter II, it was demonstrated that even temperatures as low 50 °C will change the Ag nanoparticles' plasmonic properties over time through Ostwald ripening, potentially degrading sensor performance. While the inclusion of a control molecule will enable SERS intensity normalization, studies of temperature-based sensor degradation will need to be performed to determine lifetime, after which sensor performance is too degraded to be viable. A second concern is sensor degradation through Ag oxidation. It is well-known that Ag oxidizes

over time when exposed to air, and that this oxidation reduces SERS intensity. Oxidation-based degradation can be easily mitigated, however, through storage under vacuum conditions[214] or an inert gas. While storage-based sensor degradation is a legitimate concern and must be studied for the sensor developed in this work, storage conditions can be modified to mitigate degradation and detection sensitivity can be normalized.

It is reasonable to expect that, initially, this sensing strategy will be more useful for detecting the presence of metal species in unusual quantities, rather than precise quantification of metal species in urine. Quantification will require more sophisticated machine learning than detection. Designing a microfluidic device with perhaps 5 crown ethers selected to bind in a parallel array seems feasible, with each crown ether and a control molecule functionalizing a different SERS sensor within the device. Parallel design is better than sequential design for this purpose to prevent sensors from influencing the outcomes of following sensors, since each crown ether will chelate multiple metal species. It is possible that such a device will eventually become wearable technology, but I don't see that happening for a long time. I expect that these devices will be used as disposable, single-use devices designed for application by medical personnel to carry out urinalysis in the field. Disposability eliminates the concern of cross-contamination, and reduces the need for long-term sensor stability beyond the time between production and use.

Next Steps

The design and implementation of a portable, reliable, multiplexed sensor to perform field urinalytic detection of toxic metals is an ambitious undertaking. While the work performed in this report represents a significant first step in that process, a great deal of additional study remains before a viable device is produced. The first step will be to optimize SERS surface

fabrication. This will include nanoparticle optimization and standardization of nanowire growth. Likely, standardizing nanowire growth will include mitigation of interference from PDMS hydrophobicity during hydrothermal nanowire growth. This could be accomplished through the fabrication of PDMS-PEO copolymer substrates, which have been shown to be more hydrophilic than PDMS.[189] Alternatively, it could involve dual sputter and e-beam deposition of ZnO seed. Next, it will be necessary to maximize SERS substrate functionalization with AB18C6 and determine sensitivity of metal ion detection through PDMS (or PDMS-PEO). This will determine whether the sensing strategy discussed here is feasible or if other options should be explored. Preliminary attempts to do so have been performed, the results of which are presented in APPENDIX C. Concurrently, longevity studies of the device should be performed, especially in suboptimal storage conditions. The information on loss of sensitivity gained from these studies is vital for determining how viable Ag-decorated ZnO nanowires are for urinalysis in the field. Once these studies have been performed, an examination of how the crown ether's SERS spectrum changes in response to chelation of different metals will need to be performed, and reliability studies will need to be performed in the presence of complex solutions such as urine, including relevant distractors such as non-target metal ions.

There are other aminated crown ethers that could be used to further multiplex toxic metal detection. Aminated crown ethers such as 2-aminomethyl-15-crown-5, 4'-aminodibenzo-18-crown-6, and 2-aminomethyl-18-crown-6 are commercially available, and others could be synthesized. Each crown ether will be individually bound to sensing surfaces and fluorescence-based assessment of chelation would be performed in urine. Crown will be chosen based on which metal ions they chelate, so that each of the 14 metals in the TEFSC biomonitoring panel (**Table I.1**) is chelated by at least one crown ether. The fluidic channel will be redesigned so that

each crown ether functionalizes a separate bed of Ag-decorated ZnO nanowires. A classification

algorithm will be developed to identify metals chelated by the device. On option is a hierarchical

method based on which crown ethers are exhibiting chelation-induced spectral changes. Another

option would be to perform principal component analysis on the spectra of crown ethers

chelating different metals to identify principal components for use in the development of a

classification algorithm. It is likely that device design will start simple, with a single crown ether

and a few target metal ions. An algorithm will need to be developed to reliably identify and

quantify those target ions in complex solutions before more crown ethers and more target metal

ions are added to the system.

CONCLUSION

This dissertation describes the development of a portable, disposable sensor to detect

analytes via surface enhanced Raman spectroscopy. The fabrication parameters of electron

beam-deposited silver nanoparticles on ZnO films including deposition rate, film thickness,

anneal temperature, and anneal time were evaluated for their effect on the nanoparticles'

plasmon resonance and surface enhancement. It was determined that nanoparticles deposited at a

rate of 0.1 Å/s provided better overall surface enhancement than those deposited at 0.3 Å/s, and

that 7-nm films annealed at either 50 °C for 120 min or 200 °C for 60 min provided the best

surface enhancement. These results were used to optimize silver nanoparticles deposited onto

ZnO nanowire beds fabricated inside a PDMS channel designed so that these nanowire beds

would be located on a thin PDMS wall, to minimize spectral interference from PDMS. To grow

these nanowires, ZnO seed was sputtered into the channel and nanowires grown hydrothermally.

Once the channel was completed, increasing concentrations of crystal violet in DI water from 1 –

10 μM were injected sequentially into the channel and SERS spectra were acquired. These spectra exhibited clear crystal violet peaks at the lowest concentrations evaluated, and peak intensities of crystal violet increased with increasing concentration, although saturation occurred due to crystal violet adsorption onto the sensing surface. The same sensing surface was deposited onto PDMS substrates and SERS spectra were acquired of melamine solutions ranging from 1 – 12 μM. Melamine Raman peaks were clearly visible in concentrations as low as 1 μM, well below the 7.93 μM maximum concentration allowed in infant formula. 4'-aminobenzo-18-crown-6 was shown to chelate multiple toxic metals, and both fluorescence spectroscopy and UV-vis spectrophotometry were demonstrated to be able to quantify toxic metals chelation by the crown ether. The work presented in this dissertation represents an important first step toward the development of a portable, multiplexed sensor to detect toxic metals in urine via SERS, and demonstrates the viability of the proposed mechanic of targeting toxic metal ions with crown ethers and detecting them by SERS. This work will ultimately be instrumental in comprehensively monitoring military personnel with embedded fragments and developing a clearer understanding of the short- and long-term health effects of embedded fragments.

APPENDIX A

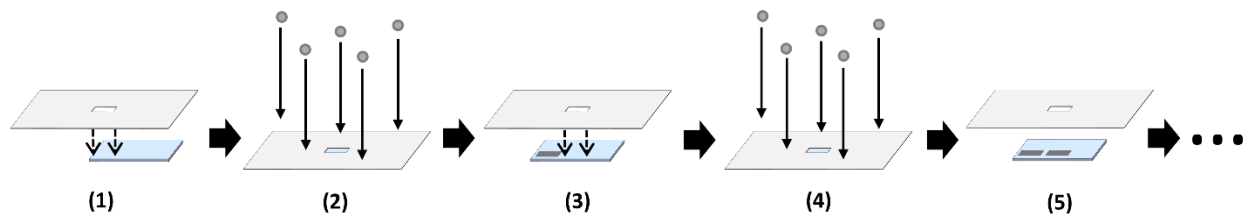SUPPLEMENTARY INFORMATION FOR CHAPTER II

Figure A.1: Illustration of the Ag deposition process. Masks cut from aluminum foil were placed on top of each substrate in step (1) such that only a small portion of the substrates was exposed. Ag was then e-beam deposited in step (2), after which the masks were moved to expose a new portion of each substrate in step (3). Ag was again deposited in step (4), and the process was repeated from step (5) onward until 9 Ag films of different thicknesses were deposited on each substrate.
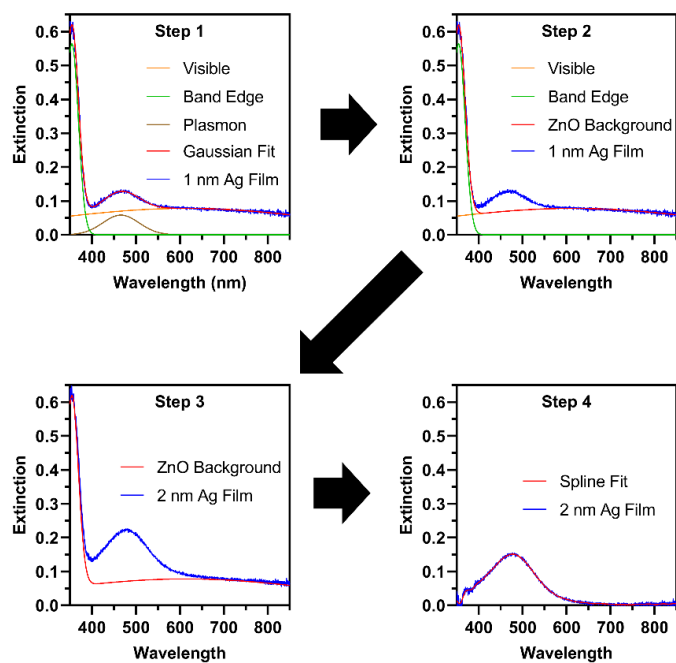
Figure A.2: Process for isolating Ag nanoparticle plasmon extinction, in which (Step 1) extinction spectra for 1-nm Ag films on each substrate were approximated with a tri-gaussian fit, (Step 2) the gaussian peaks associated with ZnO background were determined and summed, then (Step 3) subtracted from each film thickness on each substrate. The resultant plasmon peak was (Step 4) approximated with a spline fit to determine peak information.

Figure A.3: UV-Vis of two Ag-decorated ZnO samples, illustrating the variability in ZnO absorptive background induced by the fabrication and anneal process

Figure A.4: Average area of nanostructures for each Ag film thickness, demonstrating increasing nanostructure size with increasing film thickness.

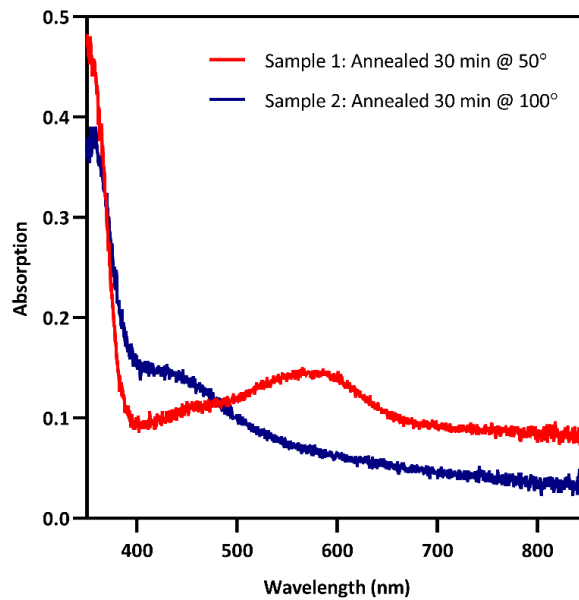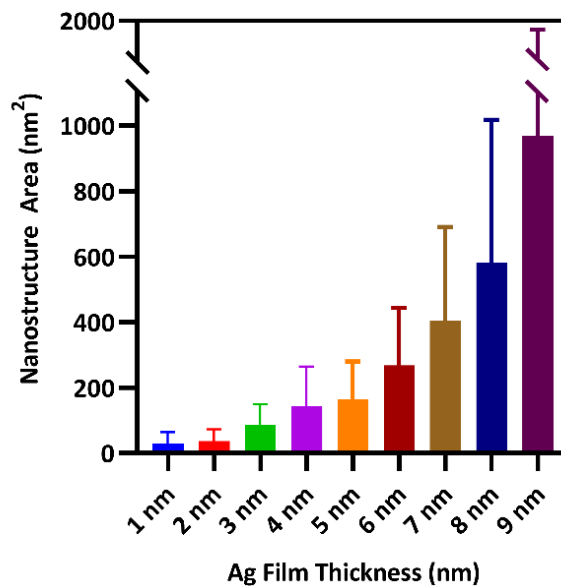**Table A.1:** Benzene and non-benzene vibrational modes associated with crystal violet Raman peaks. γ = torsion, δ = bending, ν = stretching, σ = scissoring, ρ = rocking; s = symmetric, as = asymmetric

Raman Band (cm^{-1})	Non-Benzene Vibrational Modes	Benzene	Reference
208	γ(C-H)/whole molecule breathing		[176]
225	ν_s(C-C$_{center}$-C)		[180]
345	γ(C-N-C)/δ(C-C$_{center}$-C)$_\parallel$		[176,178–181]
420	δ(C-C$_{center}$-C)/δ(C-N-C)$_\parallel$	16a	[176–180]
441	δ(C-C-C)$_{ring,\perp}$/δ(C-N-C)/δ_{as}(C-C$_{center}$-C)$_\perp$	16a	[176,177,179,181]
525	δ(C-N-C)	16b,6b	[176,178,179]
571	δ(C-C-C)$_\perp$/δ(C-N-C)/δ(C-C$_{center}$-C)	6a	[176,178,179]
605	δ(C-C-C)/δ(C-N-C)/ν_s(C-C$_{center}$-C)	6a	[176,179]
623		6b	[176]
730	ν_s(C-N-C)	4,17b	[176,179,180]
761	ν_s(C-C$_{center}$-C)/ν(C-N-C)	6a,17a	[176,179,180]
810		10a	[175–180]
825		10b,17b	[176,178,179]
915	δ(C-C$_{center}$-C)	12,17a	[176–179]
980		17a,18a	[176,179]
990	δ(C-C-C)	1	[176,179]
1130	δ(C-C$_{center}$-C)/ν(C-N)	15	[176,180]
1175	ν_{as}(C-C$_{center}$-C)	9a,9b	[175,176,178–181]
1300	ν(C-C-C)/δ(C-C-C)$_{ring}$/δ(C-H)		[175,176,180]
1345	δ(C-N)/δ(C-C-C)$_{ring}$/ν_{as}(C-C$_{center}$-C)/δ(C-H)		[176]
1374	ν(C-N)/ν_{as}(C-C$_{center}$-C)/δ(C-H)		[175,176,178–181]
1445	δ_{as}(C-H$_3$)	19b	[176,178–180]
1490	δ_{as}(C-H$_3$)	19a	[176,178,179]
1529	ν(C$_{ring}$-N)/δ_s(C-H$_3$)	8b	[175–177,180,181]
1592		8a	[175–177,179–181]
1621		8a	[175–177,179–181]

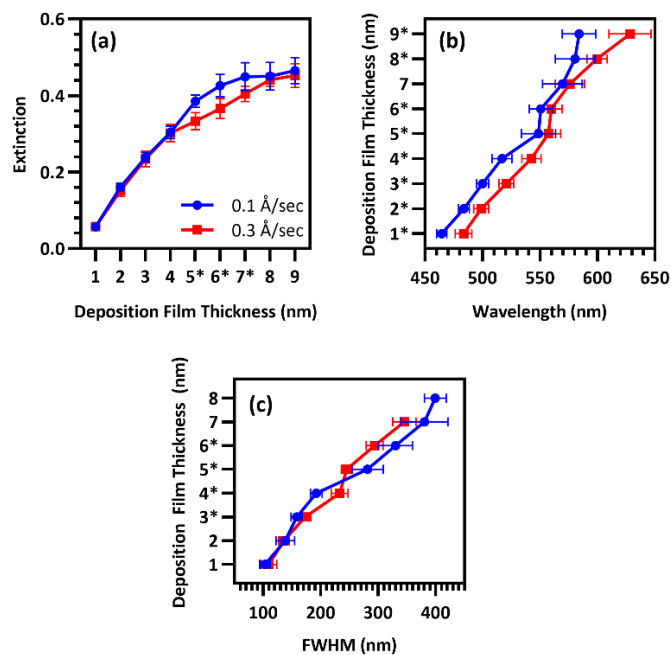**Figure A.5:** Means of (a)peak intensity (n = 40), (b)plasmon peak wavelength (n = 40), and (c)plasmon peak FWHM for each film thickness of Group A (blue) and Group B (red). Statistical testing performed with two-way ANOVA, *p = 0.05.
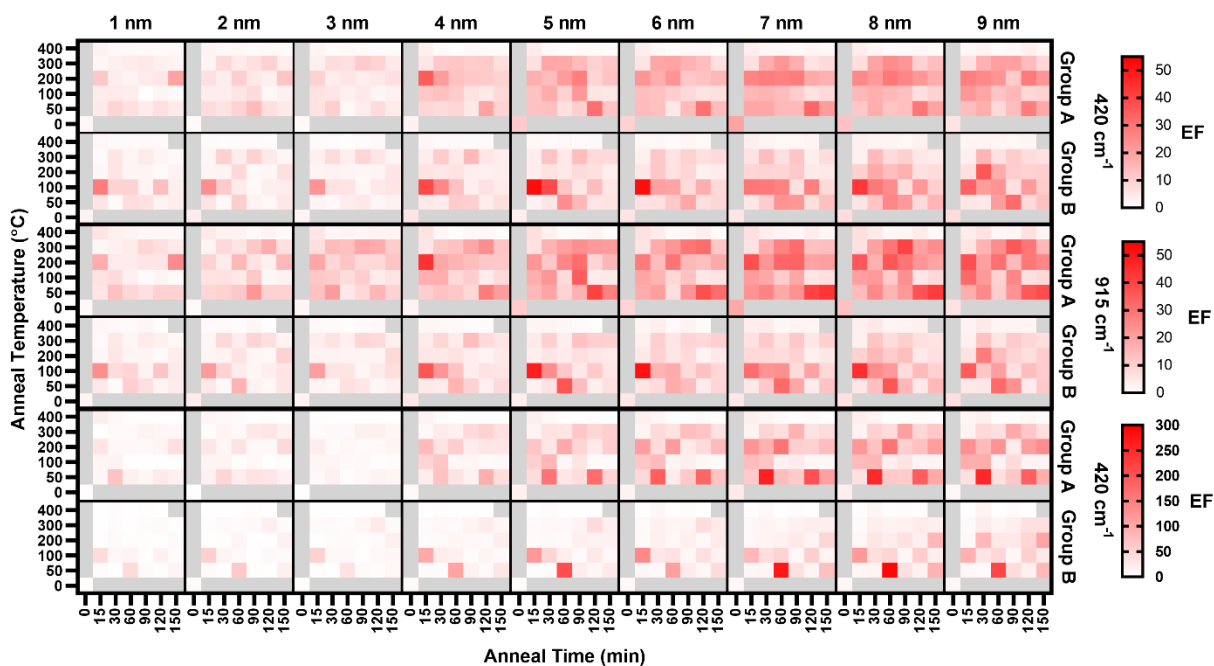
Figure A.6: Enhancement Factors for three analyzed peaks of the CV SERS spectra of each film thickness on each annealed substrate and the unannealed control for each rate group.

SUPPLEMENTARY INFORMATION FOR CHAPTER III
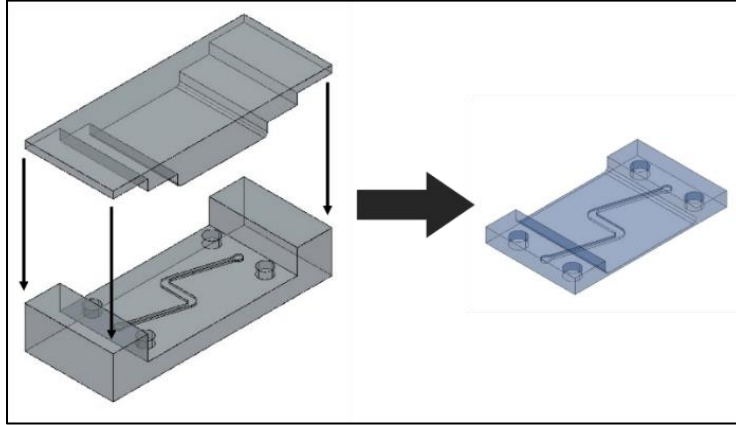
Figure B.1: Microchannel mold, designed in AutoCAD to minimize PDMS spectral interference.
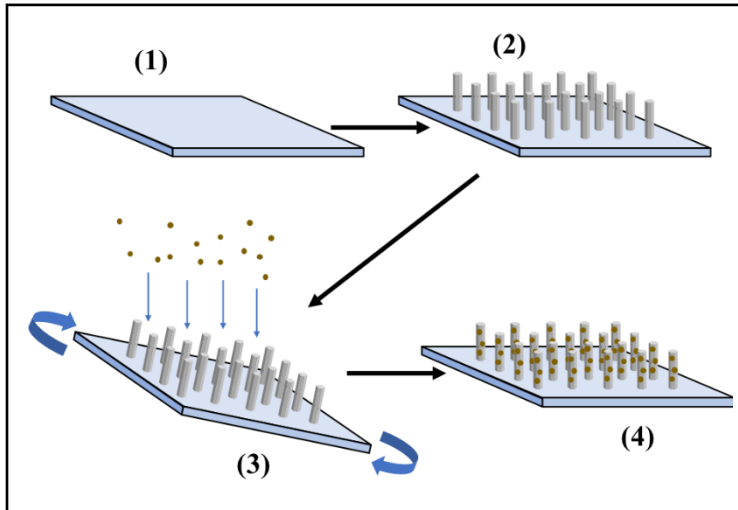
Figure B.2: Illustration of the Ag/ZnO nanoprobe fabrication process for PDMS substrates: (1) deposit 100-nm ZnO seed layer on PDMS, (2) hydrothermally grow ZnO nanowires, and (3) deposit Ag on the nanowires on an azimuthally rotated sample to get (4) a finished Ag/ZnO nanoprobe.
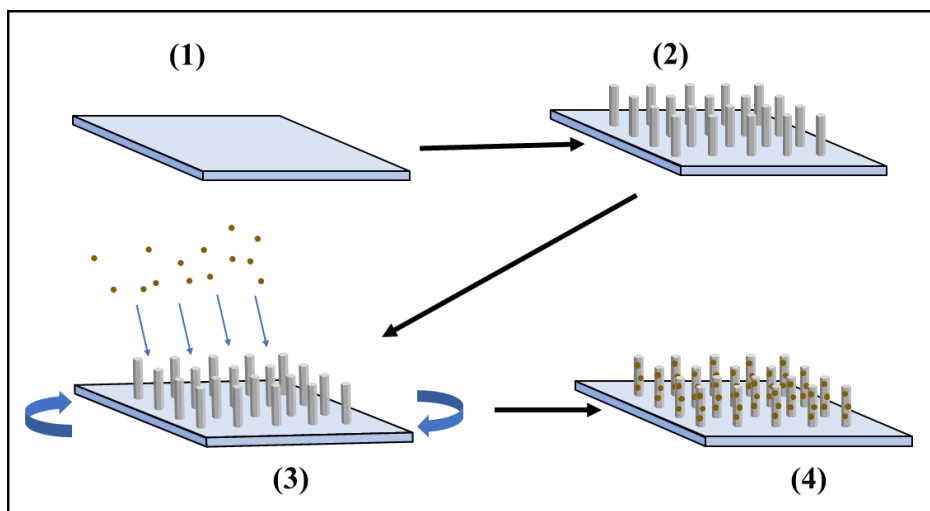
Figure B.3: Illustration of the Ag/ZnO nanoprobe fabrication process for PDMS channels: (1) deposit 100-nm ZnO seed layer on PDMS, (2) hydrothermally grow ZnO nanowires, and (3) deposit Ag from an angle on the nanowires inside a rotated channel to get (4) a finished Ag/ZnO nanoprobe.
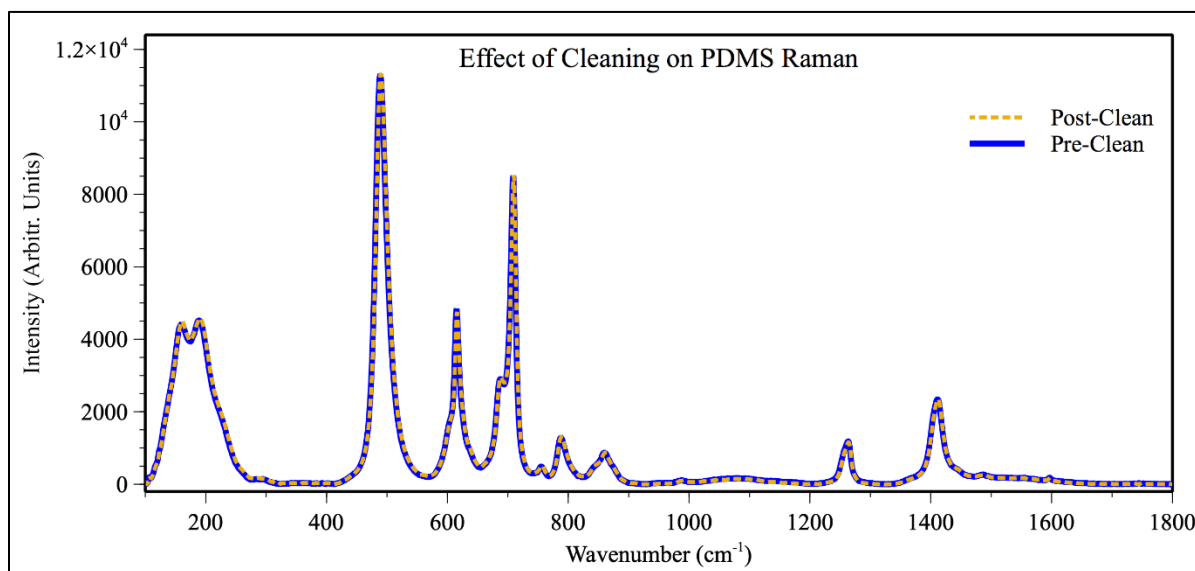
Figure B.4: Raman spectra of PDMS before and after the ALD-AMD cleaning process, demonstrating no spectral effects due to cleaning.
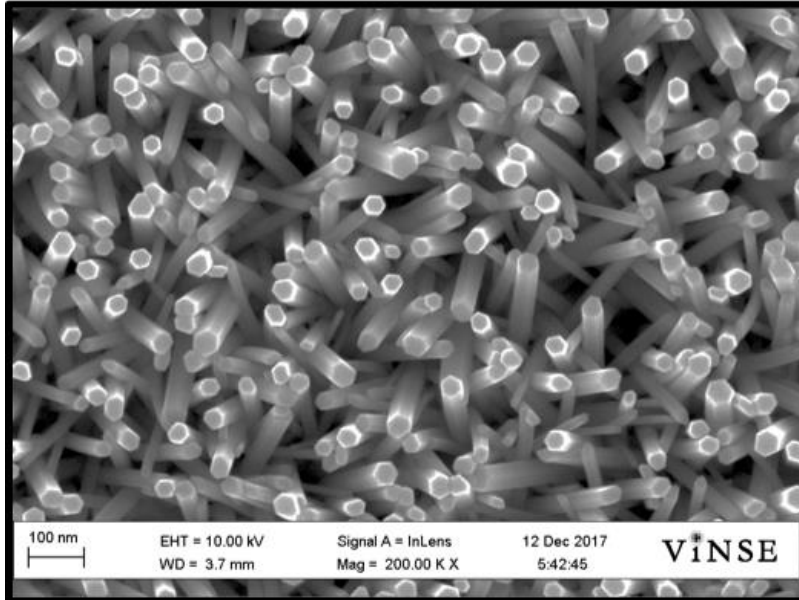
Figure B.5: SEM image of bare ZnO nanowires, exhibiting highly crystalline nanowires.
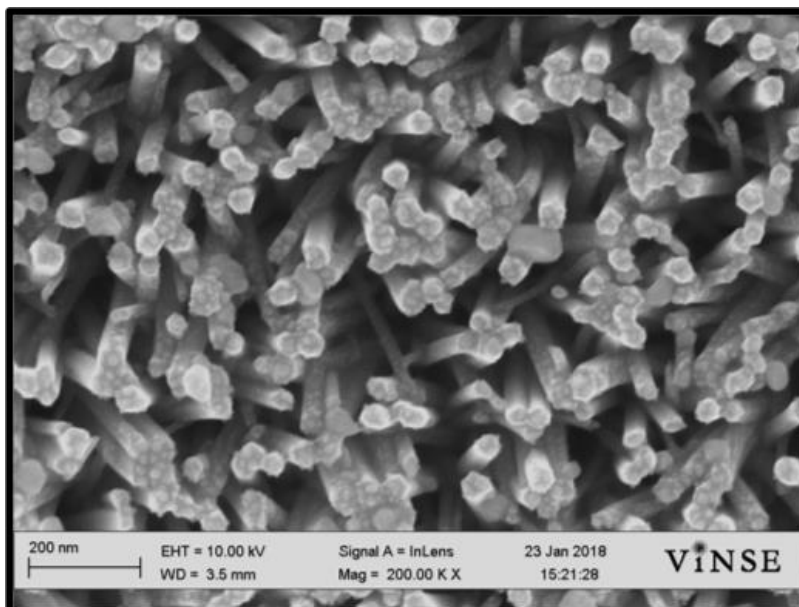
Figure B.6: SEM image of ZnO nanowires after Ag nanoparticle decoration, demonstrating dense nanoparticle formation on the sides of nanowires.
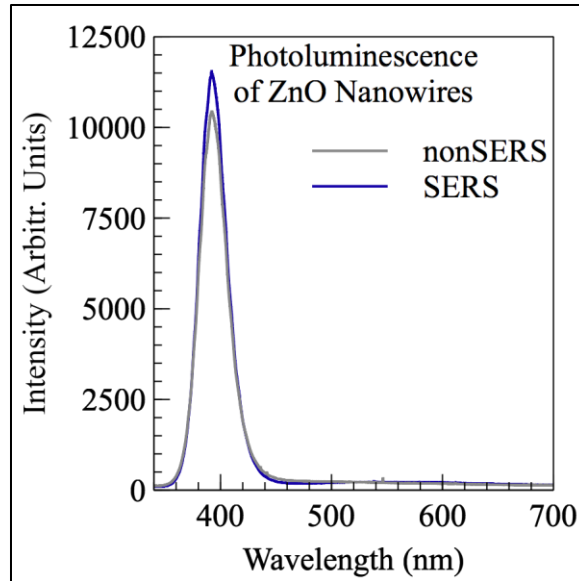
Figure B.7: PL of ZnO nanowires to be decorated with Ag nanoparticles and those to remain bare, demonstrating highly crystalline nature of the nanowires and the similarity between the two sets of nanowires.
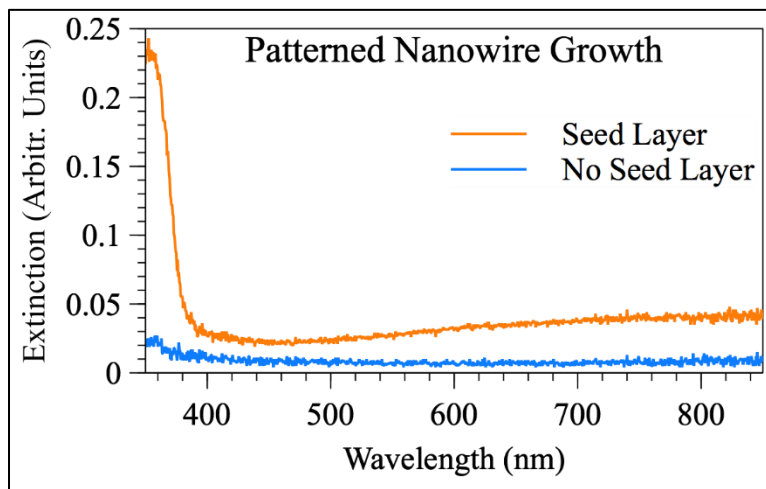
Figure B.8: UV-Vis extinction spectra after nanowire growth of the seeded and non-seeded portions of a patterned PDMS substrate, demonstrating the ability to pattern nanowire growth on PDMS by patterning the seed layer.
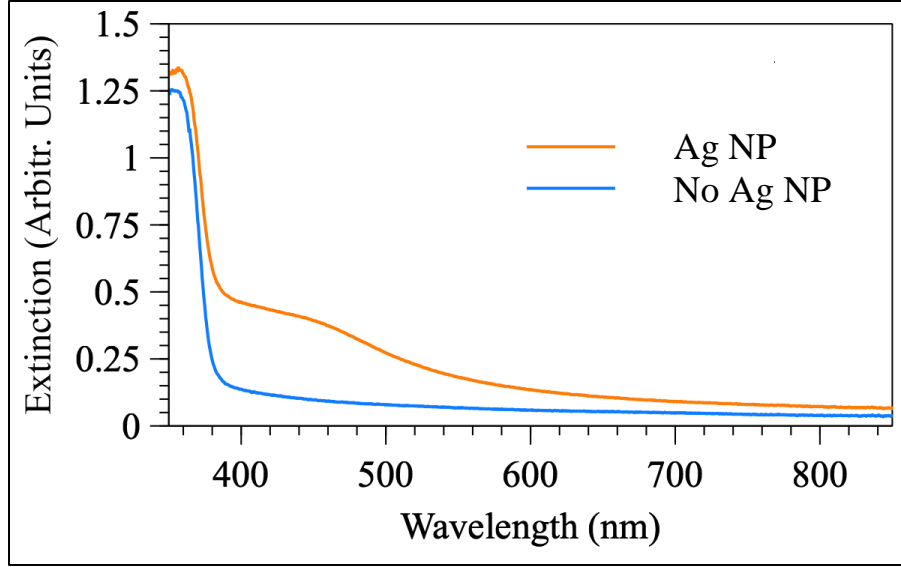
Figure B.9: UV-Vis extinction spectra of Ag/ZnO nanoprobe before and after Ag deposition, demonstrating the formation of plasmons, centered at ~450 nm.

Table B.1: Vibrational modes of PDMS in the fingerprint region: γ = torsion, δ = bending, ν = stretching, σ = scissoring, ρ = rocking; s = symmetric, as = asymmetric, $\perp$ = out-of-plane, ‖ = in-plane

Raman Band (cm^{-1})	Vibrational Modes	Reference
160	γ_{as}(C–Si–C)	[186,187]
188	δ(C–Si–C)/δ(C–Si–O)/γ_{s}(C–Si–C)/ρ(C–Si–C)/σ(C–Si–C)	[183,186,187]
488	ν_{s}(Si–O–Si)	[183–187]
615	ν(Si–O–Si)/ν(Si–C)	[186]
646	ρ_{as}(Si–C$_3$)	[184]
687	ν(Si–C)/ρ(C–H$_3$)	[183,186,187]
708	ν-s(Si–C)/δ(C–H$_3$)	[184–186]
754	ρ(C–H3)/ρ_{s}(Si–C3)/ν(Si–C)	[183,184,186]
787	ρ_{as}(C–Si–C)/ν_{as}(C–Si–C)/ρ(C–H$_3$)	[184–187]
845	ρ_{as}(C–Si–C)	[184]
859	ρ(C–Si–C)/ρ(C–H$_3$)	[184–187]
882	ρ_{as}(Si–C$_3$)/ρ_{as}(C–Si–C)	[184]
1088	ν_{as}(Si–O–Si)	[184]
1262	δ_{s}(C–H$_3$)/δ(C–H$_2$)	[184–187]
1411	δ_{as}(C–H$_3$)/δ(C–H$_2$)/σ(C–H$_2$)	[183–187]

Table B.2: Selected Vibrational modes of melamine in the fingerprint region: γ = torsion, δ = bending, ν = stretching, σ = scissoring; s = symmetric, $\perp$ = out-of-plane

Raman Band (cm^{-1})	Vibrational Modes	Reference
380	δ(C-N)	109,188
691	Ring Breathing	109,188
845	$\delta_\perp$(Ring)	109,188
1235	δ(N-H)	188
1390	σ(NH$_2$)/ν(C-N)/ δ_s(Ring)	188
1595	δ(NH$_2$)/ δ(N-C-N)	109
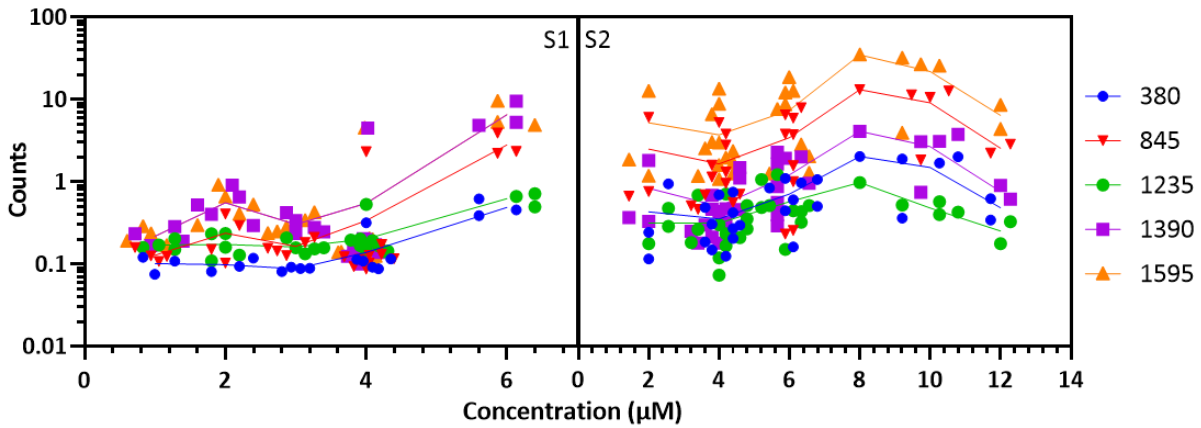
Figure B.10: Ratios of each melamine peak with the PDMS peak at 488 cm-1 for each substrate, illustrating the consistency of melamine peak intensities relative to the overall signal intensity for each measurement.
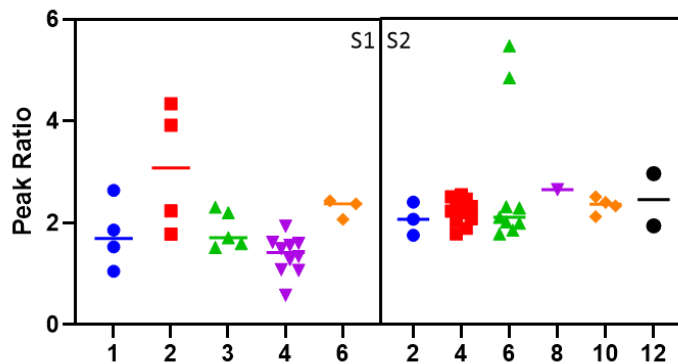
Figure B.11: Ratios of melamine peaks at 1595 cm^{-1} to 845 cm^{-1} for each melamine concentration measured for each substrate, illustrating internal signal consistency for all concentrations measured, and across substrates.
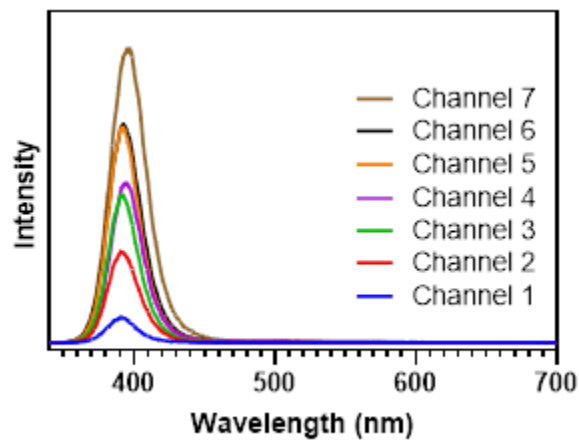
Figure B.12: Photoluminescence spectra of ZnO nanowires in 7 different PDMs channels, demonstrating variability in ZnO nanowire structure, though each still exhibits high crystallinity with few defects.
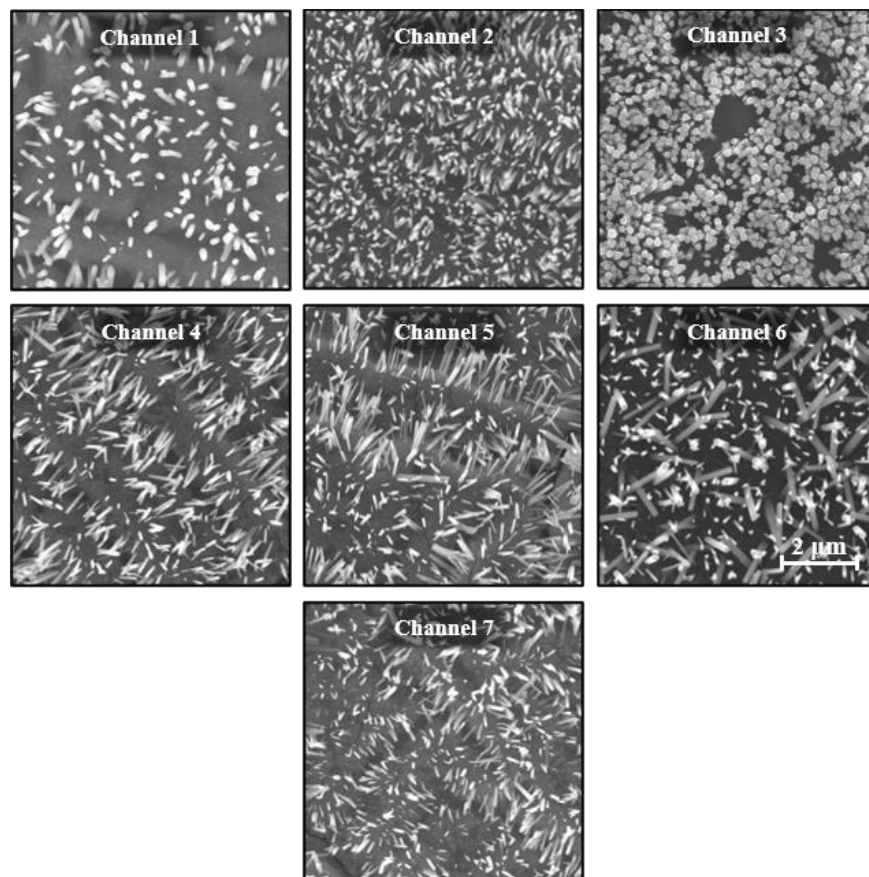
Figure B.13: SEM images of nanowires within PDMS channels on sputtered ZnO seed layers, illustrating the variability of nanowire growth on sputtered seed layers.

APPENDIX C

ADDITIONAL RESEARCH PERFORMED

Functionalizing Silver-Decorated Zinc Oxide Nanowires with 4'-Aminobenzo-18-Crown-6

Preliminary attempts were made to functionalize Ag-decorated ZnO nanowires with AB18C6. A 10-µM solution of AB18C6 was prepared in 1:3 DMSO:DI water and a portion of that solution was set aside for future analysis as a positive control. An Ag-decorated ZnO nanowire substrate grown on fused silica was placed in this solution and the solution was stirred for 60 min before being incubated overnight at room temperature to facilitate functionalization. The substrate was then pulled out of the solution and the residual fluid was washed off with DI water. Crown ether solution was taken after incubation with the SERS substrate. UV-vis (**Figure C.1**: UV-vis spectra of the 100 µM AB18C6 solution in 1:3 DMSO:DI water before and after incubation with an Ag-decorated ZnO nanowire substrate, with a spectrum of the solvent as a
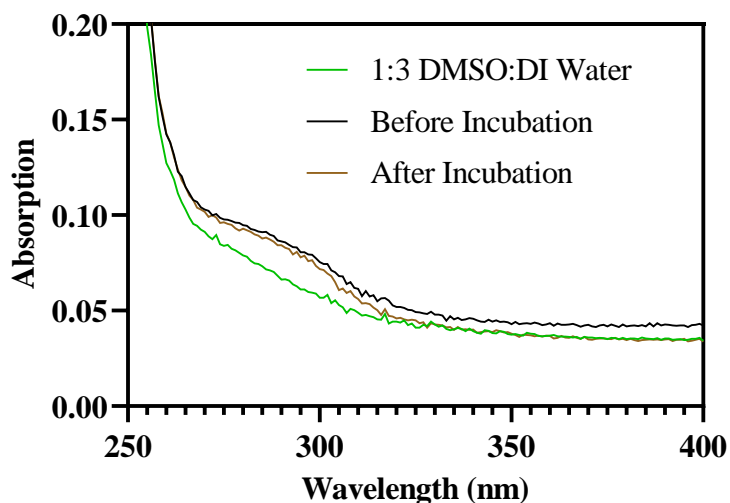
Figure C.1: UV-vis spectra of the 100 µM AB18C6 solution in 1:3 DMSO:DI water before and after incubation with an Ag-decorated ZnO nanowire substrate, with a spectrum of the solvent as a negative control
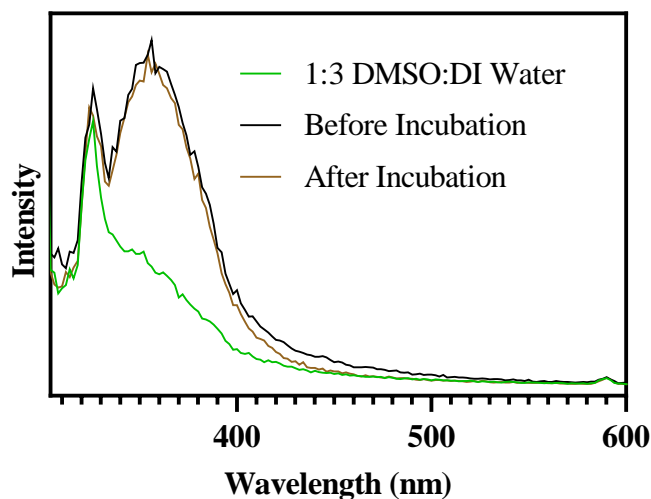
Figure C.2: UV-vis spectra of the 100 μM AB18C6 solution in 1:3 DMSO:DI water before and after incubation with an Ag-decorated ZnO nanowire substrate, with a spectrum of the solvent as a negative control

negative control) and fluorescence spectra (**Figure C.2**: UV-vis spectra of the 100 μM AB18C6 solution in 1:3 DMSO:DI water before and after incubation with an Ag-decorated ZnO nanowire substrate, with a spectrum of the solvent as a negative control) were acquired from solutions set aside before and after SERS surface functionalization, as well as 1:3 DMSO:DI water alone. The UV-vis spectrum for the post-incubation crown ether solution exhibits a decrease in intensity as compared to pre-incubation crown ether solution, which indicates that some of the crown ethers were attached to the sensing surface. The fluorescence spectrum for the post-incubation crown ether solution likewise exhibits a decrease in fluorescent intensity over the positive control, confirming that some crown ether was retained by the sensing surface.

REFERENCES

1 J. Aurell, B. K. Gullett and D. Yamamoto, *Environ. Sci. Technol.*, 2012, **46**, 11004–11012.

2 J. M. Gaitens, J. A. Centeno, K. S. Squibb, M. Condon and M. A. McDiarmid, *Mil. Med.*, 2016, **181**, e625–e629.

3 B. P. Shreve, in *Operational and Medical Management of Explosive and Blast Incidents*, eds. D. W. Callaway and J. L. Burstein, Springer International Publishing, Cham, 2020, pp. 99–107.

4 Institute of Medicine, Board on the Health of Select Populations and Committee on Gulf War and Health: Long-Term Effects of Blast Exposures, *Gulf War and Health, Volume 9: Long-Term Effects of Blast Exposures*, National Academies Press, Washington, D.C., 9th edn., 2014.

5 M. A. Kane, C. E. Kasper and J. F. Kalinich, *Mil. Med.*, 2009, **174**, 265–269.

6 D. P. Arfsten, K. R. Still, E. R. Wilfong, E. W. Johnson, S. M. McInturf, J. S. Eggers, D. J. Schaeffer and M. Y.-V. Bekkedal, *J.Toxicol. Environ. Health A*, 2009, **72**, 410–427.

7 J. Centeno, D. Rogers, G. van der Voet, E. Fornero, L. Zhang, F. Mullick, G. Chapman, A. Olabisi, D. Wagner, A. Stojadinovic and B. Potter, *Int. J. Environ. Res. Public Health*, 2014, **11**, 1261–1278.

8 S. Skaik, N. Abu-Shaban, N. Abu-Shaban, M. Barbieri, M. Barbieri, U. Giani and P. Manduca, *BMC Int. Health Hum. Rights*, 2010, **10**, 1–14.

9 J. F. Kalinich and C. E. Kasper, *Public Health Rep.*, 2016, **131**, 831–833.

10 C. A. Emond and J. F. Kalinich, *Health Phys.*, 2012, **102**, 124–136.

11 J. M. Gaitens and M. A. McDiarmid, in *Airborne Hazards Related to Deployment*, eds. C. P. Baird and D. K. Harkins, Government Printing Office, 2015, vol. 52, pp. 245–251.

12 J. F. Kalinich, V. B. Vergara and C. A. Emond, *Mil. Med.*, 2008, **173**, 754–758.

13 C. B. Weese, *U.S. Army Med. Dept. J.*, 2010, 22–28.

14 J. A. Vietas Lt. Col, G. Taylor, V. Rush and A. Deck, *Screening Health Risk Assessment Burn Pit Exposures, Balad Air Base, Iraq and Addendum Report*, U.S. Army Center for Health Promotion and Preventative Medicine.

15 A. M. Szema, *Occup. Med. Health Aff.*, 2013, **1**, 1–23.

16 C. Rose, J. Abraham, D. Harkins, R. Miller, M. Morris, L. Zacher, R. Meehan, A. Szema, J. Tolle, M. King, D. Jackson, J. Lewis, A. Stahl, M. B. Lyles, M. Hodgson, R. Teichman, W. Salihi, G. Matwiyoff, G. Meeker, S. Mormon, K. Bird and C. Baird, *J. Occup. Environ. Med.*, 2012, **54**, 746–751.

17 J. Liu, N. Lezama, J. Gasper, J. Kawata, S. Morley, D. Helmer and P. Ciminera, *J. Occup. Environ. Med.*, 2016, **58**, e249–e255.

18 A. M. S. Conlin, C. DeSciciolo, C. J. Sevick, A. T. Bukowinski, C. J. Phillips and T. C. Smith, *J. Occup. Environ. Med.*, 2012, **54**, 689–697.

19 M. J. Falvo, O. Y. Osinubi, A. M. Sotolongo and D. A. Helmer, *Epidemiologic Rev.*, 2015, **37**, 116–130.

20 C. B. Weese and J. H. Abraham, *Inhal. Toxicol.*, 2009, **21**, 291–296.

21 P. Kelleher, K. Pacheco and L. S. Newman, *Environ. Health Perspect.*, 2000, **108**, 12.

22 B. Smith, C. A. Wong, E. J. Boyko, C. J. Phillips, G. D. Gackstetter, M. A. K. Ryan and T. C. Smith, *J. Occup. Environ. Med.*, 2012, **54**, 708–716.

23 T. M. Powell, T. C. Smith, I. G. Jacobson, E. J. Boyko, T. I. Hooper, G. D. Gackstetter, C. J. Phillips and B. Smith, *J. Occup. Environ. Med.*, 2012, **54**, 682–688.

24 P. Rohrbeck, Z. Hu and T. M. Mallon, *J. Occup. Environ. Med.*, 2016, **58**, S104–S110.

25 G. A. Loh, D. G. Bell and M. J. Morris, *Curr. Pulmonol. Rep.*, 2016, **5**, 86–93.

26 J. McLean, D. Anderson, G. Capra and C. A. Riley, *Mil. Med.*, 2021, usab070.

27 M. J. Morris, L. L. Zacher and D. A. Jackson, *Mil. Med.*, 2011, **176**, 1157–1161.

28 J. M. Gaitens, M. Condon, K. S. Squibb, J. A. Centeno and M. A. McDiarmid, *J. Occup. Environ. Med.*, 2017, **59**, 1056–1062.

29 J. F. Kalinich, E. A. Vane, J. A. Centeno, J. M. Gaitens, K. S. Squibb, M. A. McDiarmid and C. E. Kasper, *Annu. Rev. Nurs. Res.*, 2014, **32**, 63–78.

30 J. M. Gaitens, C. D. Dorsey and M. A. McDiarmid, *Eur. J. Oncol.*, 2010, **15**, 77–89.

31 M. A. McDiarmid, J. M. Gaitens, S. Hines, M. Condon, T. Roth, M. Oliver, P. Gucer, L. Brown, J. A. Centeno, E. Streeten and K. S. Squibb, *Am. J. Ind. Med.*, 2015, **58**, 583–594.

32 J. M. Gaitens, B. K. Potter, J.-C. G. D'Alleyrand, A. L. Overmann, M. Gochfeld, D. R. Smith, R. Breyer and M. A. McDiarmid, *Am. J. Ind. Med.*, 2020, **63**, 381–393.

33 D. R. Glick, M. McDiarmid, J. Gaitens, C. H. Brown, K. H. Chin, M. A. Reback, P. S. Sriram, W. E. Lawson, K. L. Cavanaugh, L. Beck, J. M. Duch and S. E. Hines, in *B105 Health Effects Caused by Military Deployment*, American Thoracic Society, Philadelphia, PA, 2020, p. A4338.

34 A. V. Skalny, M. Aschner, I. P. Bobrovnitsky, P. Chen, A. Tsatsakis, M. M. B. Paoliello, A. B. Djordevic and A. A. Tinkov, *Environ. Res.*, 2021, **201**, 111568.

35 H. T. Temiz, I. H. Boyaci, I. Grabchev and U. Tamer, *Spectrochim. Acta A Mol. Biomol.Spectrosc.*, 2013, **116**, 339–347.

36 O. O. Soldatkin, I. S. Kucherenko, V. M. Pyeshkova, A. L. Kukla, N. Jaffrezic-Renault, A. V. El'skaya, S. V. Dzyadevych and A. P. Soldatkin, *Bioelectrochemistry*, 2012, **83**, 25–30.

37 C. P. Baird, *U.S. Army Med. Dept. J.*, 2013, 46–53.

38 Evans Analytical Group, 2007.

39 S. J. Hill, T. A. Arowolo, O. T. Butler, S. R. N. Chenery, J. M. Cook, M. S. Cresser and D. L. Miles, *J. Anal. At. Spectrom.*, 2002, **17**, 284–317.

40 K. L. Nuttall, W. H. Gordon and K. O. Ash, *Ann. Clin. Lab. Sci*, 1995, **25**, 264–271.

41 E. M. Nolan and S. J. Lippard, *Chem. Rev.*, 2008, **108**, 3443–3480.

42 J. Guo, Y. Chai, R. Yuan, Z. Song and Z. Zou, *Sens. Actuators B Chem.*, 2011, **155**, 639–645.

43 M. H. Mashhadizadeh and H. Khani, *Anal. Methods*, 2010, **2**, 24–31.

44 M. R. Ganjali, S. Aghabalazadeh, M. Khoobi, A. Ramazani, A. Foroumadi, A. Shafiee and P. Norouzi, *Int. J. Electrochem. Sci.*, 2011, **6**, 52–62.

45 V. K. Gupta, B. Sethi, N. Upadhyay, S. Kumar, R. Singh and L. P. Singh, *Int. J. Electrochem. Sci.*, 2011, **6**, 650–663.

46 M. H. Mashhadizadeh and R. P. Talemi, *Anal. Chim. Acta*, 2011, **692**, 109–115.

47 B. Bansod, T. Kumar, R. Thakur, S. Rana and I. Singh, *Biosens. Bioelectron.*, 2017, **94**, 443–455.

48 P. Kumar, K.-H. Kim, V. Bansal, T. Lazarides and N. Kumar, *J. Ind. Eng. Chem.*, 2017, **54**, 30–43.

49 A. Downes and A. Elfick, *Sensors*, 2010, **10**, 1871–1889.

50 L. Fabris, *ChemNanoMat*, 2016, **2**, 249–258.

51 C. V. Raman and K. S. Krishnan, *Nature*, 1928, **121**, 501–502.

52 Raman spectroscopy, https://en.wikipedia.org/w/index.php?title=Raman_spectroscopy&oldid=1037307328, (accessed August 18, 2021).

53 A. F. Chrimes, K. Khoshmanesh, P. R. Stoddart, A. Mitchell and K. Kalantar-zadeh, *Chem. Soc. Rev.*, 2013, **42**, 5880.

54 M. Fleischmann, P. J. Hendra and A. J. McQuillan, *Chem. Phys. Lett.*, 1974, **26**, 163–166.

55 I. J. Jahn, O. Žukovskaja, X.-S. Zheng, K. Weber, T. W. Bocklitz, D. Cialla-May and J. Popp, *Analyst*, 2017, **142**, 1022–1047.

56 A. Campion and P. Kambhampati, *Chem. Soc. Rev.*, 1998, **27**, 241–250.

57 K. Kneipp, H. Kneipp and J. Kneipp, *Acc. Chem. Res.*, 2006, **39**, 443–450.

58 J. R. Lombardi, R. L. Birke, T. Lu and J. Xu, *J. Chem. Phys.*, 1986, **84**, 4174–4180.

59 W. Xu, A. Zhao, F. Zuo, H. M. J. Hussain and R. Khan, *Anal. Chim. Acta X*, 2019, **2**, 100020.

60 D. Xu, W. Kang, S. Zhang, W. Yang, Y. Lei and J. Chen, *Microchemical Journal*, 2019, **148**, 190–196.

61 W. Xu, A. Zhao, F. Zuo, R. Khan, H. M. J. Hussain and J. Li, *Anal. Bioanal. Chem.*, 2020, **412**, 4565–4574.

62 Y. Li, Y. Li, J. Duan, J. Hou, Q. Hou, Y. Yang, H. Li and S. Ai, *Microchem. J.*, 2021, **161**, 105790.

63 Z. Guo, A. O. Barimah, C. Guo, A. A. Agyekum, V. Annavaram, H. R. El-Seedi, X. Zou and Q. Chen, *Spectrochim. Acta A Mol. Biomol.Spectrosc.*, 2020, **242**, 118747.

64 Y. Liu, Y. Wu, X. Guo, Y. Wen and H. Yang, *Sens. Actuators B Chem.*, 2019, **283**, 278–283.

65 X. He, X. Zhou, W. Liu, Y. Liu and X. Wang, *Langmuir*, 2020, **36**, 2930–2936.

66 J. Wang, J. Wu, Y. Zhang, X. Zhou, Z. Hu, X. Liao, B. Sheng, K. Yuan, X. Wu, H. Cai, H. Zhou and P. Sun, *Sens. Actuators B Chem.*, 2021, **330**, 129364.

67 A. Yuan, X. Wu, X. Li, C. Hao, C. Xu and H. Kuang, *Small*, 2019, **15**, 1901958.

68 H. Traboulsi and C. Awada, *ACS Omega*, 2020, **5**, 31352–31361.

69 C. E. McGhee, K. Y. Loh and Y. Lu, *Curr. Opin. Biotechnol.*, 2017, **45**, 191–201.

70 D.-W. Li, W.-L. Zhai, Y.-T. Li and Y.-T. Long, *Microchim. Acta*, 2014, **181**, 23–43.

71 S. Kamal and T. C.-K. Yang, *J. Colloid Interface Sci.*, 2022, **605**, 173–181.

72 Q. Zhao, H. Zhang, H. Fu, Y. Wei and W. Cai, *J. Hazard. Mater.*, 2020, **398**, 122890.

73 H. T. Phan, S. Geng and A. J. Haes, *Nanoscale*, 2020, **12**, 23700–23708.

74 O. Guselnikova, V. Svorcik, O. Lyutakov, M. M. Chehimi and P. S. Postnikov, *Sensors*, 2019, **19**, 2110.

75 Q. Zhou and T. Kim, *Sens. Actuators B Chem.*, 2016, **227**, 504–514.

76 D. Lee, S. Lee, G. H. Seong, J. Choo, E. K. Lee, D.-G. Gweon and S. Lee, *Appl. Spectrosc.*, 2006, **60**, 373–377.

77 B. L. Darby and E. C. Le Ru, *J. Am. Chem. Soc.*, 2014, **136**, 10965–10973.

78 J.-A. Huang, Y.-L. Zhang, H. Ding and H.-B. Sun, *Adv. Opt. Mater.*, 2015, **3**, 618–633.

79 H. Hwang, D. Han, Y.-J. Oh, Y.-K. Cho, K.-H. Jeong and J.-K. Park, *Lab Chip*, 2011, **11**, 2518–2525.

80 J. Zhou, K. Ren, Y. Zhao, W. Dai and H. Wu, *Anal. Bioanal. Chem.*, 2012, **402**, 1601–1609.

81 H.-Y. Shin, E.-L. Shim, Y.-J. Choi, J.-H. Park and S. Yoon, *Nanoscale*, 2014, **6**, 14622–14626.

82 Z. L. Wang, *J. Phys.: Condens. Matter*, 2004, **16**, R829–R858.

83 P.-H. Lei and C.-H. Cheng, *Mater. Sci. Semicond. Proc.*, 2017, **57**, 220–226.

84 Y. Wang, W. Ruan, J. Zhang, B. Yang, W. Xu, B. Zhao and J. R. Lombardi, *J. Raman Spectrosc.*, 2009, **40**, 1072–1077.

85 D. C. Mayo, C. E. Marvinney, E. S. Bililign, J. R. McBride, R. R. Mu and R. F. Haglund, *Thin Solid Films*, 2014, **553**, 132–137.

86 Y. S. Park and J. R. Schneider, *J. Appl. Phys.*, 1968, **39**, 3049–3052.

87 Z. Kang, Y. Gu, X. Yan, Z. Bai, Y. Liu, S. Liu, X. Zhang, Z. Zhang, X. Zhang and Y. Zhang, *Biosens. Bioelectron.*, 2015, **64**, 499–504.

88 W. Ji, L. Li, W. Song, X. Wang, B. Zhao and Y. Ozaki, *Angew. Chem.*, 2019, **131**, 14594–14598.

89 J. N. Anker, W. P. Hall, O. Lyandres, N. C. Shah, J. Zhao and R. P. Van Duyne, *Nat. Mater.*, 2008, **7**, 442–453.

90 J. W. Steed, *Coord. Chem. Rev*, 2001, **215**, 171–221.

91 D. K. Sarfo, E. L. Izake, A. P. O'Mullane and G. A. Ayoko, *Sens. Actuators B Chem.*, 2018, **255**, 1945–1952.

92 Y. Qian, Z. Zhang, W. Tian, L. Wen and L. Jiang, *Faraday Discuss.*, 2018, **210**, 101–111.

93 D. K. Sarfo, A. Sivanesan, E. L. Izake and G. A. Ayoko, *RSC Adv.*, 2017, **7**, 21567–21575.

94 M. Ansari Fard, G. H. Rounaghi, M. Chamsaz and K. Taheri, *J. Incl. Phenom. Macrocycl. Chem.*, 2009, **64**, 49–56.

95 H. J. Carmichael, *J. Opt. Soc. Am. B*, 1987, **4**, 1588–1603.

96 M. R. Chedekel, S. K. Smith, P. W. Post, A. Pokora and D. L. Vessell, *Proc. Natl. Acad. Sci. USA*, 1978, **75**, 5395–5399.

97 Abraham. Savitzky and M. J. E. Golay, *Anal. Chem.*, 1964, **36**, 1627–1639.

98 L. Zhang and M. J. Henson, *Appl. Spectrosc.*, 2007, **61**, 1015–1020.

99 L. A. Austin, S. Osseiran and C. L. Evans, *Analyst*, 2016, **141**, 476–503.

100 C. A. Lieber and A. Mahadevan-Jansen, *Appl. Spectrosc.*, 2003, **57**, 1363–1367.

101 M. N. Leger and A. G. Ryder, *Appl. Spectrosc.*, 2006, **60**, 182–193.

102 A. L. Cook, C. P. Haycook, A. K. Locke, R. R. Mu and T. D. Giorgio, *Nanoscale Adv.*, 2021, **3**, 407–417.

103 S. Jayabal, A. Pandikumar, H. N. Lim, R. Ramaraj, T. Sun and N. M. Huang, *Analyst*, 2015, **140**, 2540–2555.

104 M. S. Frost, Michael. J. Dempsey and D. E. Whitehead, *Sens. Actuators B Chem.*, 2015, **221**, 1003–1008.

105 Y. Zeng, J. Ren, A. Shen and J. Hu, *ACS Appl. Mater. Interfaces*, 2016, **8**, 27772–27778.

106 C. Rosman, J. Prasad, A. Neiser, A. Henkel, J. Edgar and C. Sönnichsen, *Nano Lett.*, 2013, **13**, 3243–3247.

107 R. A. Halvorson and P. J. Vikesland, *Environ. Sci. Technol.*, 2010, **44**, 7749–7755.

108 W. F. Pearman, S. M. Angel, J. L. Ferry and S. Hall, *Appl. Spectrosc.*, 2008, **62**, 727–732.

109 N. E. Mircescu, M. Oltean, V. Chiş and N. Leopold, *Vib. Spectrosc.*, 2012, **62**, 165–171.

110 X. Wang, X. Qian, J. J. Beitler, Z. (Georgia) Chen, F. R. Khuri, M. M. Lewis, H. J.-C. Shin, S. Nie and D. M. Shin, *Cancer Res.*, 2011, **71**, 1526–1532.

111 R. M. Jarvis and R. Goodacre, *Anal. Chem.*, 2004, **76**, 40–47.

112 A. A. Yanik, M. Huang, O. Kamohara, A. Artar, T. W. Geisbert, J. H. Connor and H. Altug, *Nano Lett.*, 2010, **10**, 4962–4969.

113 J. D. Driskell, K. M. Kwarta, R. J. Lipert, M. D. Porter, J. D. Neill and J. F. Ridpath, *Anal. Chem.*, 2005, **77**, 6147–6154.

114 H. Zhou, D. Yang, N. P. Ivleva, N. E. Mircescu, R. Niessner and C. Haisch, *Anal. Chem.*, 2014, **86**, 1525–1533.

115 T. T. X. Ong, E. W. Blanch and O. A. H. Jones, *Sci. Total Environ.*, 2020, **720**, 137601.

116   A. Sivanesan, E. Witkowska, W. Adamkiewicz, Ł. Dziewit, A. Kamińska and J. Waluk, *Analyst*, 2014, **139**, 1037–1043.

117   A. Kamińska, E. Witkowska, K. Winkler, I. Dzięcielewski, J. L. Weyher and J. Waluk, *Biosens. Bioelectron.*, 2015, **66**, 461–467.

118   A. M. Giovannozzi, F. Rolle, M. Sega, M. C. Abete, D. Marchis and A. M. Rossi, *Food Chem.*, 2014, **159**, 250–256.

119   D. S. Moore and R. J. Scharff, *Anal. Bioanal. Chem.*, 2009, **393**, 1571–1578.

120   K. Kneipp, H. Kneipp, I. Itzkan, R. R. Dasari and M. S. Feld, *J. Phys.: Condens. Matter*, 2002, **14**, R597–R624.

121   T. Vo-Dinh, *Trends Anal. Chem.*, 1998, **17**, 557–582.

122   J. D. Caldwell, O. J. Glembocki, F. J. Bezares, M. I. Kariniemi, J. T. Niinistö, T. T. Hatanpää, R. W. Rendell, M. Ukaegbu, M. K. Ritala, S. M. Prokes, C. M. Hosten, M. A. Leskelä and R. Kasica, *Opt. Express*, 2011, **19**, 26056–26064.

123   D. Graham, K. Faulds and W. E. Smith, *Chem. Commun.*, 2006, 4363–4371.

124   R. Pilot, R. Signorini, C. Durante, L. Orian, M. Bhamidipati and L. Fabris, *Biosensors*, 2019, **9**, 57–156.

125   Y. Zhang, B. Walkenfort, J. H. Yoon, S. Schlücker and W. Xie, *Phys. Chem. Chem. Phys.*, 2015, **17**, 21120–21126.

126   P. A. Mosier-Boss, *Nanomaterials*, 2017, **7**, 142–172.

127   A. L. Cook, C. S. Carson, C. E. Marvinney, T. D. Giorgio and R. R. Mu, *J. Raman Spectrosc.*, 2017, **48**, 1116–1121.

128   B. H. Nguyen, V. H. Nguyen and H. N. Tran, *Adv. Nat. Sci: Nanosci. Nanotechnol.*, 2016, **7**, 033001.

129   Y. Xie, S. Yang, Z. Mao, P. Li, C. Zhao, Z. Cohick, P.-H. Huang and T. J. Huang, *ACS Nano*, 2014, **8**, 12175–12184.

130   X. Wang, S. Xu, H. Li, J. Tao, B. Zhao and W. Xu, *J. Raman Spectrosc.*, 2012, **43**, 459–463.

131   A. Yu. Panarin, S. N. Terekhov, K. I. Kholostov and V. P. Bondarenko, *Appl. Surf. Sci.*, 2010, **256**, 6969–6976.

132   T. Szymborski, E. Witkowska, W. Adamkiewicz, J. Waluk and A. Kamińska, *Analyst*, 2014, **139**, 5061–5064.

133   Y. He, S. Su, T. Xu, Y. Zhong, J. A. Zapien, J. Li, C. Fan and S.-T. Lee, *Nano Today*, 2011, **6**, 122–130.

134   X. Liu, Q. Hu, Q. Wu, W. Zhang, Z. Fang and Q. Xie, *Colloids Surf. B*, 2009, **74**, 154–158.

135   P. Yang, H. Yan, S. Mao, R. Russo, J. Johnson, R. Saykally, N. Morris, J. Pham, R. He and H.-J. Choi, *Adv. Funct. Mater.*, 2002, **12**, 323–331.

136   A. Janotti and C. G. Van de Walle, *Rep. Prog. Phys.*, 2009, **72**, 126501–126530.

137   Z. Yi, X. Xu, X. Kang, Y. Zhao, S. Zhang, W. Yao, Y. Yi, J. Luo, C. Wang, Y. Yi and Y. Tang, *Surf. Coat. Tech.*, 2017, **324**, 257–263.

138   G. Barbillon, *Coatings*, 2019, **9**, 86.

139   E. Thouti, N. Chander, V. Dutta and V. K. Komarala, *J. Opt.*, 2013, **15**, 035005–035012.

140   S. Rezaee, *Results Phys.*, 2018, **9**, 1521–1524.

141   B. Amin-Ahmadi, H. Idrissi, M. Galceran, M. S. Colla, J. P. Raskin, T. Pardoen, S. Godet and D. Schryvers, *Thin Solid Films*, 2013, **539**, 145–150.

142 M. Bechelany, X. Maeder, J. Riesterer, J. Hankache, D. Lerose, S. Christiansen, J. Michler and L. Philippe, *Cryst. Growth Des.*, 2010, **10**, 587–596.

143 J. Schindelin, I. Arganda-Carreras, E. Frise, V. Kaynig, M. Longair, T. Pietzsch, S. Preibisch, C. Rueden, S. Saalfeld, B. Schmid, J.-Y. Tinevez, D. J. White, V. Hartenstein, K. Eliceiri, P. Tomancak and A. Cardona, *Nat. Methods*, 2012, **9**, 676–682.

144 C. A. Schneider, W. S. Rasband and K. W. Eliceiri, *Nat. Methods*, 2012, **9**, 671–675.

145 *MATLAB R2019a*, The Mathworks, Inc., Natick, Massachusetts, United States.

146 Y. Nishijima, Y. Hashimoto, L. Rosa, J. B. Khurgin and S. Juodkazis, *Adv. Opt. Mater.*, 2014, **2**, 382–388.

147 J. Dunkers and H. Ishida, *Spectrochim. Acta A*, 1995, **51**, 855–867.

148 A. Krylov, A. Vtyurin, P. Petkov, I. Senkovska, M. Maliuta, V. Bon, T. Heine, S. Kaskel and E. Slyusareva, *Phys. Chem. Chem. Phys.*, 2017, **19**, 32099–32104.

149 C. A. Patil, I. J. Pence, C. A. Lieber and A. Mahadevan-Jansen, *Opt. Lett.*, 2014, **39**, 303.

150 H. Sato, H. Chiba, H. Tashiro and Y. Ozaki, *J. Biomed. Opt.*, 2001, **6**, 366–370.

151 S. J. Cho, Y.-H. Ahn, K. K. Maiti, U. S. Dinish, C. Y. Fu, P. Thoniyot, M. Olivo and Y.-T. Chang, *Chem. Commun.*, 2010, **46**, 722–724.

152 D. He, B. Hu, Q.-F. Yao, K. Wang and S.-H. Yu, *ACS Nano*, 2009, **3**, 3993–4002.

153 C.-L. Zhang, K.-P. Lv, H.-P. Cong and S.-H. Yu, *Small*, 2012, **8**, 648–653.

154 A. J. Chung, Y. S. Huh and D. Erickson, *Nanoscale*, 2011, **3**, 2903–2908.

155 T. K. Sinha, S. K. Ghosh, R. Maiti, S. Jana, B. Adhikari, D. Mandal and S. K. Ray, *ACS Appl. Mater. Interfaces*, 2016, **8**, 14986–14993.

156 J. Guo, F. Zeng, J. Guo and X. Ma, *J. Mater. Sci. Technol.*, 2020, **37**, 96–103.

157 K. B. Kim, J.-H. Han, H. Choi, H. C. Kim and T. D. Chung, *Small*, 2012, **8**, 378–383.

158 Y.-J. Oh and K.-H. Jeong, *Lab Chip*, 2014, **14**, 865–868.

159 H.-Y. Wu and B. T. Cunningham, *Nanoscale*, 2014, **6**, 5162–5171.

160 C. Novara, A. Lamberti, A. Chiadò, A. Virga, P. Rivolo, F. Geobaldo and F. Giorgis, *RSC Adv.*, 2016, **6**, 21865–21870.

161 H. Pu, W. Xiao and D.-W. Sun, *Trends Food Sci. Technol.*, 2017, **70**, 114–126.

162 S. H. Lee, H. J. Lee, D. Oh, S. W. Lee, H. Goto, R. Buckmaster, T. Yasukawa, T. Matsue, S.-K. Hong, Ko, M.-W. Cho and T. Yao, *J. Phys. Chem. B*, 2006, **110**, 3856–3859.

163 M. Ladanov, P. Algarin-Amaris, G. Matthews, M. Ram, S. Thomas, A. Kumar and J. Wang, *Nanotechnology*, 2013, **24**, 375301.

164 S. Seiffert, J. Dubbert, W. Richtering and D. A. Weitz, *Lab Chip*, 2011, **11**, 966–968.

165 H. Mao, W. Wu, D. She, G. Sun, P. Lv and J. Xu, *Small*, 2014, **10**, 127–134.

166 Renishaw, http://www.renishaw.com/en/automatic-intelligent-background-removal--25934, (accessed August 9, 2021).

167 C. V. Rumens, M. A. Ziai, K. E. Belsey, J. C. Batchelor and S. J. Holder, *J. Mater. Chem. C*, 2015, **3**, 10091–10098.

168 T.-M. Durďáková, Z. Hrdlička, M. Dendisová, M. Švecová and O. Vopička, *Polymer*, 2020, **188**, 122140.

169 A. Galdámez-Martinez, G. Santana, F. Güell, P. R. Martínez-Alanis and A. Dutt, *Nanomaterials*, 2020, **10**, 857.

170 D. C. Mayo, J. R. Nolen, A. Cook, R. R. Mu and R. F. Haglund, in *Proceedings Volume 9737, Synthesis and Photonics of Nanoscale Materials XIII*, SPIE, San Francisco, California, United States, 2016, vol. 9737, p. 97370I.

171 Y. Suzaki and A. Tachibana, *Appl. Opt.*, 1975, **14**, 2809.

172   C. A. Bennett, *Principles of Physical Optics*, John Wiley & Sons, Inc., Hoboken, NJ, USA, 2008.

173   A. Sengupta, N. Brar and E. J. Davis, *J. Colloid Interface Sci.*, 2007, **309**, 36–43.

174   S. S. Masango, R. A. Hackler, N. Large, A.-I. Henry, M. O. McAnally, G. C. Schatz, P. C. Stair and R. P. Van Duyne, *Nano Lett.*, 2016, **16**, 4251–4259.

175   J. Wang, X. Gao, H. Sun, B. Su and C. Gao, *Mater. Lett.*, 2016, **162**, 142–145.

176   M. V. Cañamares, C. Chenal, R. L. Birke and J. R. Lombardi, *J. Phys. Chem. C*, 2008, **112**, 20295–20300.

177   W. Meng, F. Hu, L.-Y. Zhang, X.-H. Jiang, L.-D. Lu and X. Wang, *J. Mol. Struct.*, 2013, **1035**, 326–331.

178   T. Watanabe and B. Pettinger, *Chem. Phys. Lett.*, 1982, **89**, 501–507.

179   L. Angeloni, G. Smulevich and M. P. Marzocchi, *J. Raman Spectrosc.*, 1979, **8**, 305–310.

180   E. J. Liang, X. L. Ye and W. Kiefer, *J. Phys. Chem. A*, 1997, **101**, 7330–7335.

181   F. A. Harraz, A. A. Ismail, H. Bouzid, S. A. Al-Sayari, A. Al-Hajry and M. S. Al-Assiri, *Appl. Surf. Sci.*, 2015, **331**, 241–247.

182   M. Alcolea Palafox, *Int. J. Quantum Chem.*, 2000, **77**, 661–684.

183   L. A. Leites, S. S. Bukalov, T. S. Yadritzeva, M. K. Mokhov, B. A. Antipova, T. M. Frunze and V. V. Dement'ev, *Macromolecules*, 1992, **25**, 2991–2993.

184   M. J. Shenton, H. Herman and G. C. Stevens, *Polym. Int.*, 2000, **49**, 1007–1013.

185   R. P. S. de Campos, I. V. P. Yoshida, M. C. Breitkreitz, R. J. Poppi and J. A. F. da Silva, *Spectrochim. Acta A Mol. Biomol.Spectrosc.*, 2013, **100**, 67–71.

186   L. Bistričić, L. M. Borjanović and V. Dananić, *Vib. Spectrosc.*, 2013, **68**, 1–10.

187   L. Jayes, A. P. Hard, C. Séné, S. F. Parker and U. A. Jayasooriya, *Anal. Chem.*, 2003, **75**, 742–746.

188   X. Chen, Y. Hu, J. Gao, Y. Zhang and S. Li, *Appl. Spectrosc.*, 2013, **67**, 491–497.

189   K. S. Dogbevi, B. K. D. Ngo, C. W. Blake, M. A. Grunlan and G. L. Coté, *ACS Appl. Polym. Mater.*, 2020, **2**, 1731–1738.

190   A. L. Cook, F. Xue and T. D. Giorgio, in *Proceedings of The 6th World Congress on Recent Advances in Nanotechnology*, Avestia, Virtual Conference, 2021.

191   H. Fischer, *A Guide to U.S. Military Casualty Statistics: Operation Freedom's Sentinel, Operation Inherent Resolve, Operation New Dawn, Operation Iraqi Freedom, and Operation Enduring Freedom*, Congressional Research Services, 2015.

192   K. Cavanaugh, 2018.

193   Y. K. Agrawal, P. Shrivastav and S. K. Menon, *Sep. Purif. Technol.*, 2000, **200**, 177–183.

194   R. Li, G. Yang, J. Yang, J. Han, J. Liu and M. Huang, *Food Control*, 2016, **68**, 14–19.

195   D. Grys, R. Chikkaraddy, M. Kamp, O. A. Scherman, J. J. Baumberg and B. de Nijs, *J. Raman Spectrosc.*, 2021, **52**, 412–419.

196   M. A. Khan, T. P. Hogan and B. Shanker, *J. Raman Spectrosc.*, 2009, **40**, 1539–1545.

197   L. Chen, L. Luo, Z. Chen, M. Zhang, J. A. Zapien, C. S. Lee and S. T. Lee, *J. Phys. Chem. C*, 2010, **114**, 93–100.

198   W. Yantasee, Y. Lin, K. Hongsirikarn, G. E. Fryxell, R. Addleman and C. Timchalk, *Environ. Health Perspect.*, 2007, **115**, 1683–1690.

199   D. Guimarães, M. L. Praamsma and P. J. Parsons, *Spectrochim. Acta B At. Spectrosc.*, 2016, **122**, 192–202.

200   L. Yang, R. E. Sturgeon, D. Prince and S. Gabos, *J. Anal. At. Spectrom.*, 2002, **17**, 1300–1303.

201   K. Wrobel, K. Wrobel, B. Parker, S. Kannamkumarath and J. A. Caruso, *Talanta*, 2002, **58**, 899–907.

202   M. Rouillon and M. P. Taylor, *Environ. Pollut.*, 2016, **214**, 255–264.

203   Md. R. Awual, T. Yaita, T. Taguchi, H. Shiwaku, S. Suzuki and Y. Okamoto, *J. Hazard. Mater.*, 2014, **278**, 227–235.

204   E. Flores, J. Pizarro, F. Godoy, R. Segura, A. Gómez, N. Agurto and P. Sepúlveda, *Sens. Actuators B Chem.*, 2017, **251**, 433–439.

205   N. Serrano, A. González-Calabuig and M. del Valle, *Talanta*, 2015, **138**, 130–137.

206   Z.-Q. Cheng, Z.-W. Li, R. Yao, K.-W. Xiong, G.-L. Cheng, Y.-H. Zhou, X. Luo and Z.-M. Liu, *Nanoscale Res. Lett.*, 2020, **15**, 117.

207   Q. He, Y. Han, Y. Huang, J. Gao, Y. Gao, L. Han and Y. Zhang, *Sens. Actuators B Chem.*, 2021, **341**, 130031.

208   C. Tian, L. Zhao, J. Zhu and S. Zhang, *J. Hazard. Mater.*, 2021, **416**, 126251.

209   A.-H. Chiou, J.-L. Wei and S.-H. Chen, *Coatings*, 2021, **11**, 685.

210   X. He, S. Wang, Y. Liu and X. Wang, *Sci. China Chem.*, 2019, **62**, 1064–1071.

211   V. Dugandžić, S. Kupfer, M. Jahn, T. Henkel, K. Weber, D. Cialla-May and J. Popp, *Sens. Actuators B Chem.*, 2019, **279**, 230–237.

212   R. Chadha, A. Das, A. K. Debnath, S. Kapoor and N. Maiti, *Colloids Surf. A: Physicochem. Eng. Asp.*, 2021, **615**, 126279.

213   C. Song, J. Li, Y. Sun, X. Jiang, J. Zhang, C. Dong and L. Wang, *Sens. Actuators B Chem.*, 2020, **310**, 127849.

214   X. Luo, W. Liu, C. Chen, G. Jiang, X. Hu, H. Zhang and M. Zhong, *Opt. Laser Technol.*, 2021, **139**, 106969.